Theses and Dissertations

2016

Mechanical Properties of Von Willebrand Factor and Glycoprotein Ib-IX at the Single-Molecule Level

Wei Zhang
Lehigh University

Follow this and additional works at: http://preserve.lehigh.edu/etd

Part of the Mechanical Engineering Commons

Mechanical Properties of Von Willebrand Factor and Glycoprotein Ib-IX at the Single-Molecule Level

By

Wei Zhang

Presented to the Graduate and Research Committee

of Lehigh University

in Candidacy for the Degree of

Doctor of Philosophy

in

Mechanical Engineering

Lehigh University

May, 2016

ii

Approved and recommended for acceptance as a dissertation in partial fulfillment of the requirements for the degree of Doctor of Philosophy.

_____

Date

_____

Dissertation Advisor, Dr. Xiaohui (Frank) Zhang

_____

Accepted Date

Committee Members:

_____

Dr. Alparslan Oztekin

_____

Dr. Edmund Webb III

_____

Dr. Yaling Liu

_____

Dr. Xuanhong Cheng

Acknowledgments

I also want to thank the whole Lehigh University community as a whole for its welcoming environment. These great friends have filled my life with happiness and moments I will never forget.

Lastly, I would like to thank my parents for supporting my career decisions and for their unconditional love.

Table of Contents

List of Tables

List of Figures

List of Symbols and Abbreviations

AFM	atomic force microscopy
bp	base pair
BSS	Bernard–Soulier syndrome
CD	circular dichroism
cDNA	complementary DNA
Cys	cysteine
Dig	digoxigenin
dsDNA	double-stranded DNA
dsRNA	double-stranded RNA
DTT	dithiothreitol
E. Coli	Escherichia coli
Fab	the fragment antigen-binding fragment
FBS	fetal bovine serum
FLAG	a polypeptide having the sequence motif DYKDDDDK
FMC25	an anti-GPIX antibody
FVIII	the factor FVIII
GdmCl	guanidinium chloride
GP	glycoprotein
GST	glutathione S-transferase
h	hour
HA	hexahistidine-tagged
HEK	human embryonic kidney
His	hexahistidine
Ibα-S	recombinant GPIbα stalk region
IgG	Immunoglobulin G
kDa	kilodalton (= 1000 daltons)
M	molar
MBP	maltose-binding protein
min	minute
MSD	mechanosensory/mechanosensitive domain
MW	molecular weight
Myc	a regulator gene that codes for a transcription factor
N	newton (force unit)

N.R.	non-reducing
Ni	Nickel
nM	nanomolar
nm	nanometer
NTA	Nitrilotriacetic acid
PBS	phosphate buffer saline
pN	piconewtwon (force unit)
PS	polystyrene
PSD	position sensitive detector
PVDF	polyvinylidene difluoride
R.	reducing
s	second
S. pyogenes	*Streptococcus pyogenes*
SpyCatcher	*S. pyogenes* (Spy) protein partner
SpyTag	*S. pyogenes* peptide (Spy) tag
ssDNA	single-stranded DNA
VNTR	variable number tandem repeat
VWD	von Willebrand disease
VWF	von Willebrand factor
WLC	worm-like chain
WM23	an anti-(glycoprotein Ib complex) murine monoclonal antibody
$\alpha_4\beta_7$	a type of integrin
μM	micromolar
μm	micrometer

Parameters' Symbol:

β	$(k_BT)^{-1}$, a constant
ΔG	barrier height in two-state model
ΔL_c	contour length increment
$\Delta x^{\ddagger}$	barrier width in two-state model
F	force
F^*	most probable force
$\langle F \rangle$	mean force
$\dot{F}$	loading rate of force

F_r	refolding force
F_u	unfolding force
γ	friction
k_B	Boltzmann constant
K	spring constant
k	off rate under force
k_0	spontaneous off rate
L_c	contour length
L_p	persistence length
ν	a scaling factor in the Dudko model, indicating the free-energy surface profile
σ	standard deviation
SD	standard deviation
SEM	standard error of the mean
T	absolute temperature
τ	lifetime under force
τ_0	intrinsic lifetime
v	pulling velocity
x	extension or shortening

Abstract

Single-molecule experiments have been designed and carried out for investigating the mechanical and biological properties of proteins, and molecular interactions at a single molecular level [1, 2]. Since the first single-molecule technique, patch clamp, was developed in the 1970s [3], a variety of other techniques and instruments have been developed, including atomic force microscopy (AFM) [4–8], optical tweezers [9–19], magnetic tweezers [20–27], and biomembrane force probes (BFP) [28–30]. These optimized instruments are able to achieve high spatial resolution (nanometers), temporal resolution (microseconds), and force sensitivity (piconewtons). Furthermore, they allow us to carry out the single-molecule experiments in a force-clamp mode or force-ramp mode. In order to quantify the biological properties of the molecule, we can consider the molecule as an elastic chain and apply the worm-like chain (WLC) model [31, 32]. To characterize the mechanical properties of proteins or interactions, the Bell–Evans model [33] and Dudko model [34] are available, both of which are derived from Kramers theory [35].

This thesis focuses on three projects of single-molecule force experiments using optical tweezers and AFM. In the first project, we performed single-molecule force experiments on the platelet mechanosensor glycoprotein (GP) Ib-IX complex. We successfully identified a juxtamembrane mechanosensory domain (MSD) in GPIb-IX, and further proposed a model of GPIb-IX mechanosensing (i.e., the "trigger model"). In this model, the force-induced unfolding of MSD is the step by which GPIb-IX converts a mechanical signal into a change of the protein conformation, a type of signal that could be recognized and transduced further. This has significant implications for the pathogenesis and treatment of related blood diseases.

In the second project, we developed a novel SpyTag system for single-molecule experiments, inspired by the recent discovery of the SpyTag/SpyCatcher covalent bonds [36]. In a single-molecule experimental system, linking methods are usually used to capture, hold, and further apply an external force on the molecule. The traditional methods have many disadvantages, such as low mechanical stability and strength, or requiring the sample purification and reduction reaction. In our newly developed SpyTag system, we can perform the single-molecule pulling experiments efficiently since the SpyTag/SpyCatcher covalent bonds have high mechanical stability and mechanical strength. The minimal difference in the lifetimes of the C-terminal SpyTag/SpyCatcher and N-terminal SpyTag/SpyCatcher, indicates that we can fuse either terminal of the SpyTag to some other proteins without sacrificing the covalent bonds stability. This property makes the single-molecule experiments simpler. Furthermore, the new system simplifies the single-molecule experiments by eliminating the sample purification step, as well as providing a new approach to investigate complexed proteins, such as the integrin $\alpha_4\beta_7$. In addition, the novel system does not involve any protein reduction procedure. This property makes the system promising for measuring the domain-domain interactions within a protein, such as the von Willebrand factor (VWF), where traditional methods are not practical since the sample reduction step would also break the abundant inner disulfide bonds of VWF.

Finally, we aimed to investigate the domain-domain interactions within VWF, as well as the influence of the clotting factor VIII (FVIII) in VWF folding/unfolding, using the novel SpyTag system. Our experimental results showed that, there existed differences in the force spectrum of pulling VWF fragments, D'D3A1 or D'D3A1A2, in the absence and presence of 5 nM FVIII. We referred that FVIII binding to VWF altered the force-induced unfolding of D'D3A1A2 fragment, and possibly changed the

normal A2 unfolding pathway where no FVIII existed. However, more unfolding events are still needed to clearly reveal the function of FVIII as well as the interaction between FVIII and D'D3A1 or D'D3A1A2. Meanwhile, we intended to investigate the influence of FVIII on the A2 unfolding pathways, by performing single-molecule experiments on the A2 protein, with or without FVIII. Besides, we need to use D'D3 generated by mammalian cells instead of bacterial cells, to repeat the single-molecule experiments.

These projects have significant implications for the pathogenesis and treatment of related blood diseases.

Chapter 1:   Introduction

1.1   Hemostasis and Haemostasis

Hemostasis or haemostasis is a natural physiological process that causes bleeding to stop and prevent blood loss at the site of injury. The process includes two main components—the primary hemostasis and the secondary hemostasis.

The primary hemostasis includes two steps, vasoconstriction (vascular spasm) and platelet plug formation. Vasoconstriction is the first response of blood vessels to blood vessel damage, which is controlled by vascular smooth muscle cells. At the site of damage, the blood vessels constrict to reduce the volume of blood flow passing through and limit the loss of blood, which is effective in small blood vessels [37, 38]. In the platelet plug formation step, platelets first adhere to subendothelial matrix proteins (e.g. collagen) through the interactions of collagen with the platelet surface receptor glycoprotein (GP) VI and integrin $\alpha_2\beta_1$ (the platelet GPIa/IIa complex), and of collagen with the platelet GPIb-IX-V complex via von Willebrand factor (VWF) (Figure 1.1A) [39, 40]. Platelet activation is associated with a change in platelet shape, secretion of platelet agonists, such as thromboxane A_2 (TXA$_2$) and adenosine diphosphate (ADP), and intracellular signaling which leads to further integrin $\alpha_{IIb}\beta_3$ (GPIIb/IIIa) activation. A platelet plug is finally formed by aggregated platelets via fibrinogen bridges (Figure 1.1B). In healthy blood vessels, the endothelial cells produce and secrete coagulation and aggregation inhibitors, such as nitric oxide and prostacyclin, instead of VWF, to prevent blood clotting and platelet aggregation.

The secondary hemostasis consists of a cascade of blood coagulation or clotting, and converts the liquid blood into a semi-solid gel. In this process, the main role is played by an enzyme, called thrombin, which converts inactive soluble fibrinogen into insoluble fibrin fibers, thus forming an interlocking meshwork of fibers and a

framework to trap erythrocytes for the clot. The conversion of inactive prothrombin to thrombin is initiated by two pathways: (1) the intrinsic pathway or the contact activation; and (2) the extrinsic pathway or the tissue factor (TF) pathway. There are at least twelve factors, generally indicated by Roman numerals, involved in the series of reactions, and these coagulation factors circulate as inactive zymogens in blood. Most factors are serine proteases (enzymes) and act by cleaving downstream proteins. However, factor VIII (FVIII) and factor V (FV) are glycoproteins, and factor XIII (FXIII) is a transglutaminase [41].
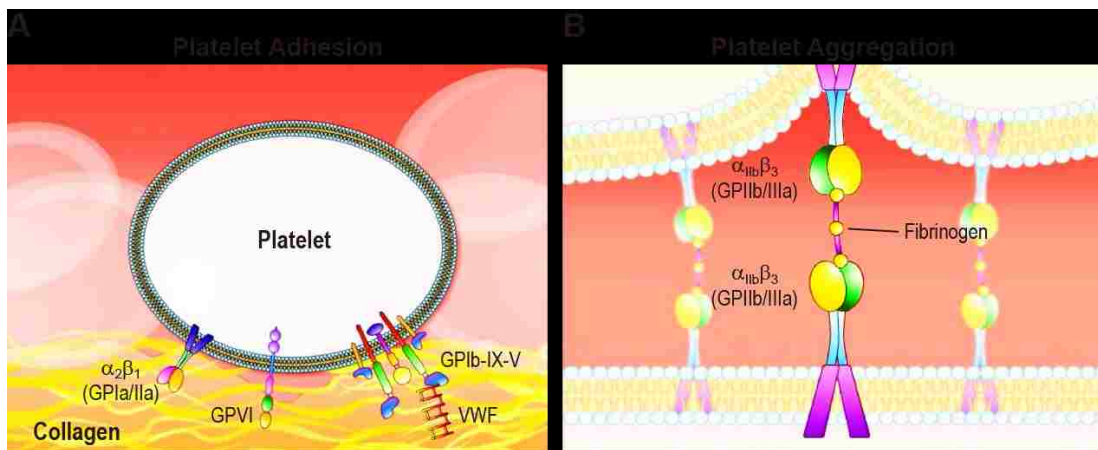
Figure 1.1 Platelet adhesion and aggregation. (A) Platelet adhesion. In the platelet plug formation step, platelets first adhere to subendothelial matrix proteins (e.g. collagen) through the interactions of collagen with the platelet surface receptor glycoprotein (GP) VI and integrin $\alpha_2\beta_1$ (the platelet GPIa/IIa complex), and of collagen with the platelet GPIb-IX-V complex via VWF. (B) Platelet aggregation through the binding of activated platelets. Platelet activation is associated with a change in platelet shape, secretion of platelet agonists, such as thromboxane A_2 (TXA$_2$) and adenosine diphosphate (ADP), and intracellular signaling which leads to further integrin $\alpha_{IIb}\beta_3$ (GPIIb/IIIa) activation. A platelet plug is finally formed by aggregated platelets via fibrinogen bridges. Figures are captured from https://youtu.be/0pnpoEy0eYE, produced by Mechanisms in Medicine Inc.

1.1.1 Bleeding Disorders

Bleeding disorders are a group of conditions where the blood cannot clot normally when needed. These diseases can be inherited or acquired, while most of them are genetically inherited, such as the most well-known hemophilia. As described before,

the process of hemostasis requires the platelets and as many as twenty different plasma proteins to function properly, including von Willebrand factor (VWF) and other blood clotting factors. There are many different classification methods for characterizing different types of bleeding disorders [42–45], among which hemophilia, von Willebrand disease (VWD), and factor XI (FXI) deficiency are the most common with general population prevalence rates of between 1 and 0.001% [46, 47].

Hemophilia or haemophilia contains three types, each of which is related to deficiency of one type of clotting factor. Hemophilia A and hemophilia B result from deficiencies in factor VIII (FVIII) and factor IX (FIX), respectively. The two types of hemophilia are recessive sex-linked, X chromosome disorders, so they are more likely to occur in males than females. According to the most recent survey [48], approximately 62% of bleeding disorders are hemophilia, and ~80% of those are of type A and ~16% are of type B. There are mild, moderate and severe forms of both types of hemophilia, which reflect the level of active FVIII or FIX in the plasma. Hemophilia C is an autosomal genetic disorder resulting from the deficiency of FXI, and not completely recessive.

Von Willebrand disease (VWD) is an inherited condition resulting from the deficiency or defect in von Willebrand factor (VWF), where the mode of inheritance is autosomal. VWD is the most common inherited bleeding disorder of humans. VWF functions in the primary hemostasis, and also carries another clotting protein FVIII. Deficiency in VWF causes defective platelet adhesion and a secondary deficiency in FVIII. The outcome is that VWF deficiency can cause bleeding that appears similar to that caused by platelet dysfunction or hemophilia, though it is usually milder than hemophilia. VWD is classified into three major types (i.e., Types 1, 2, and 3), based on the levels of VWF and FVIII's activity in the blood. Type 1 VWD, the mildest and most

common form, is inherited as an autosomal dominant trait. Type 2 VWD, similar to Type 1 VWD, is subdivided further depending on whether the dysfunctional protein has decreased or paradoxically increased function in the binding to platelets. Type 3 VWD, the most severe and least common form, which is characterized by recessive inheritance and virtual absence of VWF. For treatment of serious cases, patients may need to take the drugs that can help to increase the level of VWF in the blood or with infusions of blood factor concentrates.

1.1.2   Von Willebrand Factor (VWF)

As shown before, in human hemostasis or the coagulation process, there are complicated interactions between platelets and proteins in the plasma. In primary hemostasis, platelet adhesion to exposed collagen on subendothelial matrix is mediated by the von Willebrand factor (VWF) bridge. Its structure helps to give it specific biochemical and immunologic properties, and allows for unique and essential physiologic functions [49]. Defects in VWF or other related receptors will cause bleeding diseases, such as hemophilia and von Willebrand diseases.

The mechanical shear force generated by blood flow in the vasculature is a critical factor that mediates physiologic hemostasis and pathologic thrombosis. Platelet adhesion to collagen is mediated by VWF multimers (shown in Figure 1.2). The VWF multimers act as an intermediary bridge between collagen fibrils on damaged blood vessel walls and platelets in blood. Platelet adhesion and aggregation, which is induced by the enhanced shear stress, requires the existence of VWF and its platelet surface receptor glycoprotein (GP) Ib-IX and integrin $\alpha_{IIb}\beta_3$ (GPIIb/IIIa) [50, 51]. It has also been shown that both VWF and GPIb-IX complex are capable of sensing and reacting to tensile forces [52, 53].
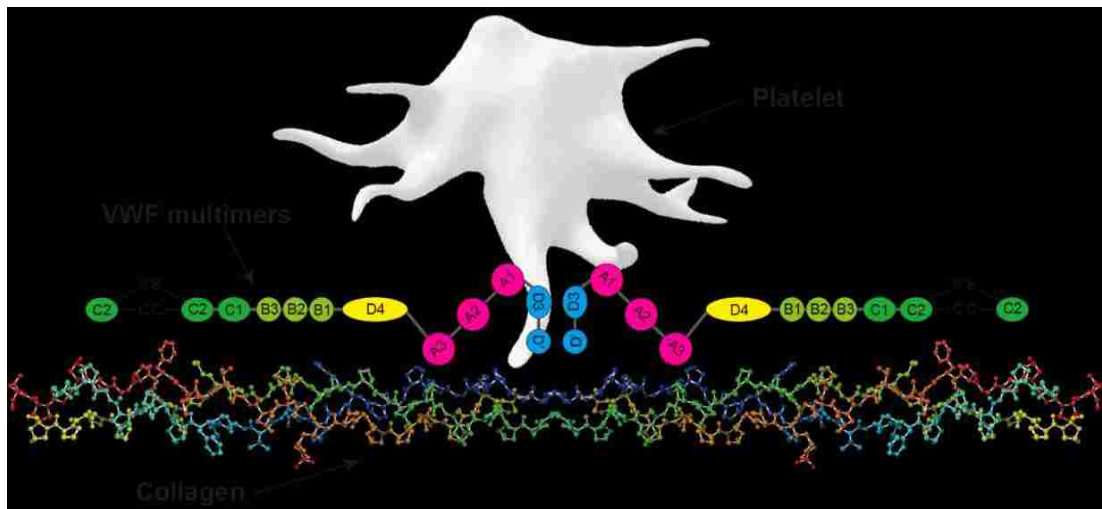
Figure 1.2 Schematic of multimeric VWF mediating platelet adhesion to collagen. Mature VWF monomer subunits (2050 amino acids) form VWF dimers and further multimers with variable lengths through disulfide bonds. During the blood clotting process, the VWF multimers are immobilized through the A3 domain on the collagen fibrils existing on the sub-endothelium of blood vessel wall, while its A1 domain binds to the platelet surface receptor GPIb-IX.

Von Willebrand factor (VWF) is an ultra-large, multimeric vascular protein, which plays an essential role in capturing platelets onto the damaged blood vessel wall, allowing the initiation of blood clotting. VWF is an adhesive glycoprotein existing in different types of cells, such as platelets, endothelial cells and megacariocites. It is synthesized as a large mature VWF monomer subunit (2050 amino acids), and these subunits are capable of forming dimers and further multimers with variable lengths through disulfide bonds, as illustrated in Figure 1.2 and Figure 1.3. VWF concatamers in plasma can contain up to 40 to 200 monomers, corresponding to molecular weights of up to 4000 to 10000 kDa, and can be extended to lengths of up to 3 to 15 μm [54, 55].

As shown in Figure 1.3, VWF monomer is a mosaic protein, consisting of several domains. Each domain contributes to some function(s). VWF is secreted to plasma though an initially narrow secretion pore, in the form of long tubules characteristic of Weibel-Palade bodies (WPB), i.e., a concatamer.
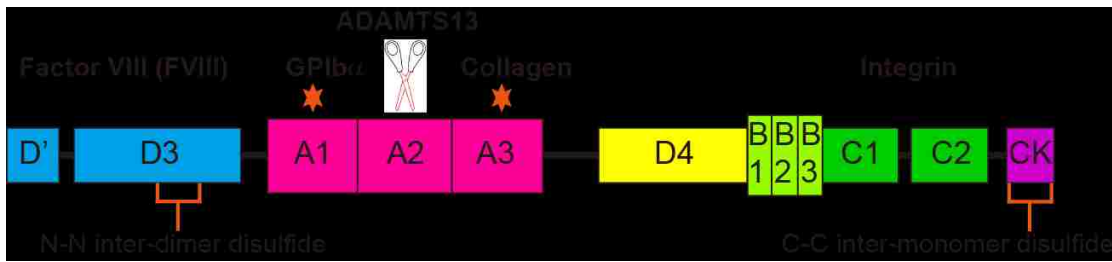
Figure 1.3 Primary structure and domain organization of VWF monomer. VWF domains are arranged as the figure shows. Cysteines are connected for chemically determined disulfide bonds [56, 57]. VWF acts as a carrier for factor VIII (FVIII) in blood circulation. FVIII interacts with D'D3 domain. Platelet binding to VWF is through the binding of VWF A1 domain to the Ibα chain of platelet surface receptor glycoprotein (GP) Ib-IX [58]. The metalloprotease ADAMTS13 is only able to cleave the unfolded A2 domain to produce smaller VWF multimers, to facilitate VWF release into bloodstream, and promote hemostasis [53, 55, 59]. The binding of VWF to collagen is through its A2 domain.

In stasis, the concatamer forms an irregularly coiled, compact shape, due to self-association between VWF monomers [60, 61]. When the blood shear flow increases, VWF extends, and is stretched to from a chain-like shape when the shear rate is above a critical threshold ~5000 s^{-1} [55, 62–65]. The elongated VWF exposes its A1-A2-A3 domains, which is correlated with activation of VWF-mediated platelet aggregation, platelet binding and rolling on VWF substrates, and binding of VWF to collagen and VWF substrates [66]. VWF is capable of sensing and responding to tensile forces, which induces the unfolding of the A2 domain. The metalloprotease ADAMTS13 is only able to cleave the unfolded A2 domain to produce smaller VWF multimers, help to facilitate VWF release into bloodstream, and promote hemostasis [53, 55, 59]. Platelet binding to VWF is through the binding of VWF A1 domain to the Ibα chain of platelet surface receptor glycoprotein (GP) Ib-IX [58]. VWF binding to collagen is achieved mainly by A3 binding to collagen III and A1 binding to collagen VI [55, 67–70].

The crystal structures of VWF A1 domain and A2 domain are shown in Figure 1.4. The A1 domain contains N- and C-terminal arms that wrap across the domain's lower surface (Figure 1.4A). VWF A1 does not contain a metal ion-dependent adhesion site

9

motif [71]. The Ibα chain of platelet surface receptor GPIb-IX possibly binds to the front and upper surfaces of A1. The VWF A2 domain contains a loop in place of the α4 helix, and a *cis*-proline (Figure 1.4B) [72]. The Tyr-Met cleavage site is buried in the poorly packed β4-strand in the central hydrophobic core. A2 has a C-terminal α6-helix, which is linked to the Tyr structurally. 2 Cysteine residues on the α6-helix are linked by an unusual vicinal disulfide bond.
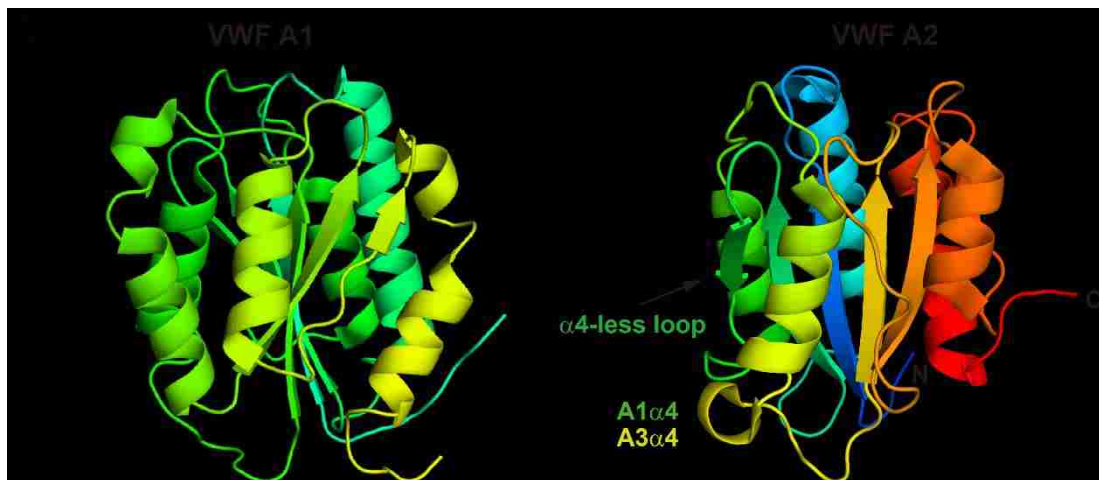
Figure 1.4 Structure of VWF A1 domain and A2 domain. (A) VWF A1 domain has a highly conserved set of hydrogen bonds external to the long-range disulfide (not drawn here) seen in all crystal structures. (B) VWF A2 domain has a C-terminal, vicinal disulfide bond and lacks of α4 loop [72–75].

1.1.3   Glycoprotein (GP) Ib-IX Complex

The glycoprotein (GP) Ib-IX-V complex, expressed exclusively on plasma platelets and megakaryocytes, is the platelet receptor for VWF and many other molecules involved in hemostasis and thrombosis [76, 77]. GPIb-IX-V complex contains GPIb-IX and GPV. However, the association between them is relatively weak [78]. The GPIb-IX complex consists of GPIbα, GPIbβ, and GPIX subunits in a 1:2:1 stoichiometry [79, 80]. GPIbα contains, starting from the N-terminus, a leucine-rich repeat (LRR) domain, a highly glycosylated macroglycopeptide region, a stalk region of about 60 residues, a pair of cysteine residues that connect to GPIbβ via disulfide bonds, a single-span

transmembrane helix, and a relatively short cytoplasmic domain that is connected to the cytoskeleton through filamin A [81]. The complex is capable of sensing the blood flow through its binding to VWF A1 domain and further transmitting a signal into the platelet [52]. However, the mechanism of this signaling was not clarified for a long period. The organization of GPIb-IX complex is shown in Figure 1.5A. The VWF-A1–GPIbα complex forms a super β-sheet at the interface between the A1 β3 and GPIbα β14 strands (Figure 1.5B).
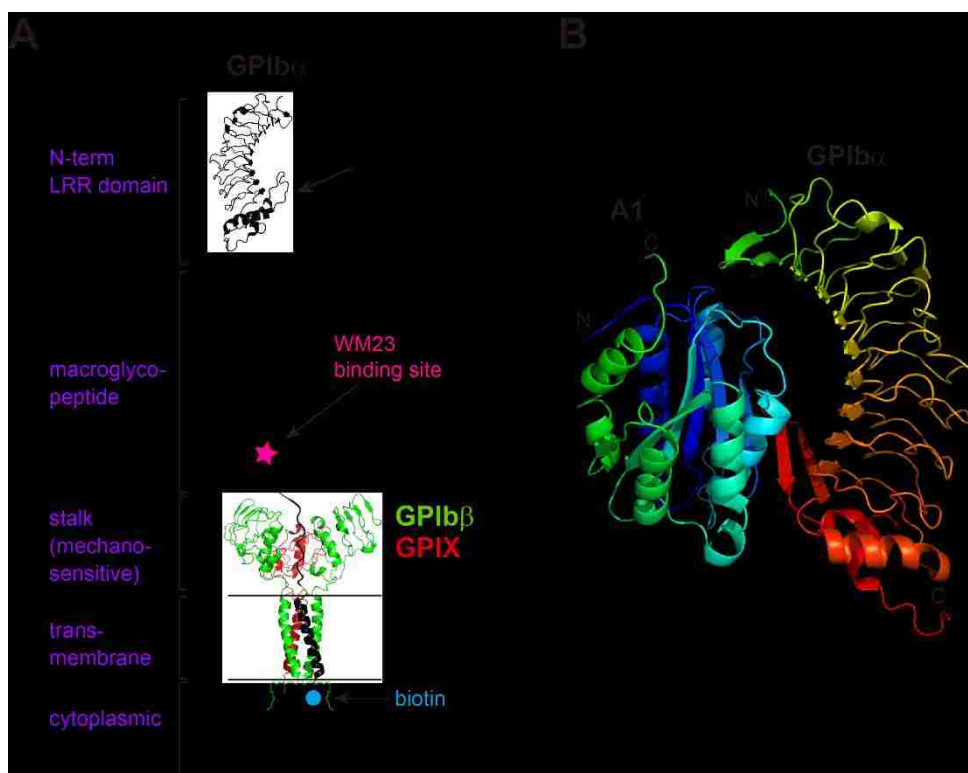
Figure 1.5 Organization of GPIb-IX complex. (A) The GPIb-IX complex consists of GPIbα, GPIbβ, and GPIX subunits in a 1:2:1 stoichiometry [79, 80]. GPIbα contains, starting from the N-terminus, a leucine-rich repeat (LRR) domain, a highly glycosylated macroglycopeptide region, a stalk region of about 60 residues, a pair of cysteine residues that connect to GPIbβ via disulfide bonds, a single-span transmembrane helix, and a relatively short cytoplasmic domain that is connected to the cytoskeleton through filamin A [81]. (B) The VWF-A1–GPIbα complex forms a super β-sheet at the interface between the A1 β3 and GPIbα β14 strands.

1.1.4 Human Factor VIII (FVIII) / Antihemophilic Factor

Human factor VIII (FVIII) or the antihemophilic factor is one of the most important serum proteins in hemostasis and coagulation. The mature FVIII is synthesized as a single polypeptide chain of 2332 amino acid residues (~280 kDa) by various tissues, including the liver, kidney, and spleen [82–84]. It has the domain structure A1-A2-B-A3-C1-C2 [82, 85], as shown in Figure 1.6. The A1-A2 domains are present in the heavy chain (HC) with a molecular weight varying between 90 kDa and 200 kDa [84], while the domains A3-C1-C2 form the light chain (LC) with a molecular weight of 76 kDa [86]. A region of the C2 domain contains a membrane binding site of FVIII and the site of interaction with VWF [87]. FVIII circulates as a series of noncovalent heterodimers with VWF, produced by proteolytic cleavage at the B-A3 junction or within the B domain [88]. At the site of a vascular injury, it nucleates the assembly of a membrane-bound protease complex on the surface of activated platelets. During the blood coagulation process, FVIII acts as a cofactor to the serine protease factor IXa (FIXa). FVIII is released after the peptide containing the VWF-binding site is removed by proteolysis near the N-terminus of LC by traces of thrombin. Further proteolysis between the A1 and A2 domains results in generation of FVIIIa, the active heterotrimeric cofactor. Upon proteolytic activation by either FXa or thrombin, FVIIIa dissociates from VWF, binds to the FIXa serine protease, and directs the localization of the resulting complex to the membrane surface of activated platelets via an interaction with its C-terminal C2 domain. The membrane-bound complex between FVIIIa and FIXa complex proteolytically activates factor X (FX), and then converts prothrombin to thrombin [82, 86, 87]. The proteolytic reaction rate hastens by nearly 5 orders of magnitude when it is localized onto the negatively charged membrane surface with fixed protein conformation in complex with FVIIIa and FVa [89].
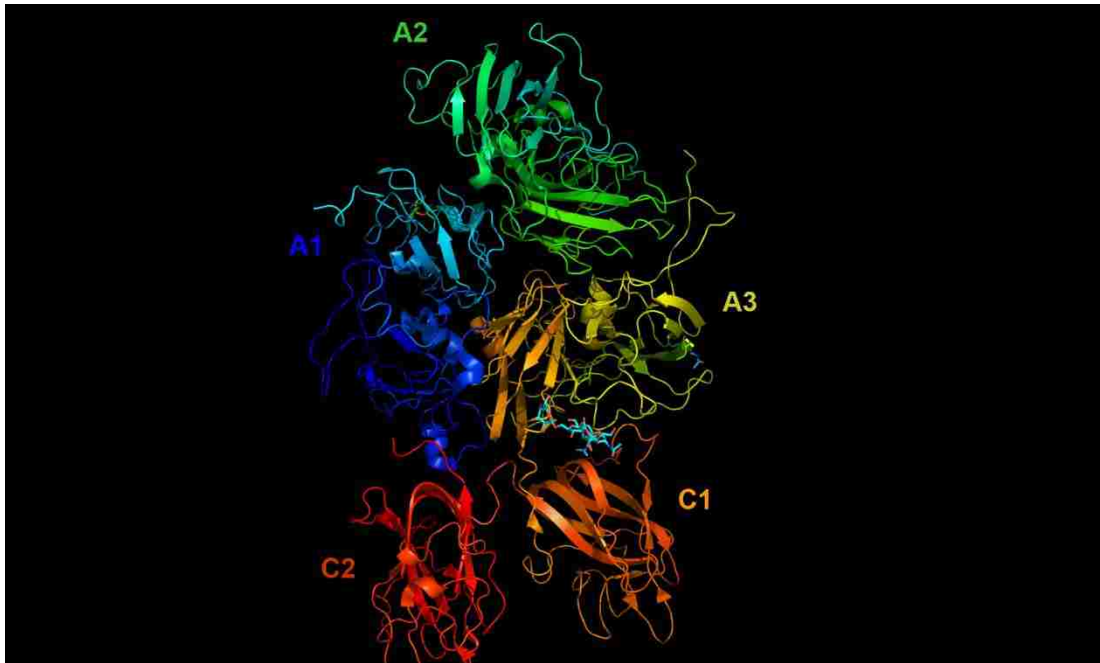
Figure 1.6 Crystal structure of factor VIII (FVIII). The mature VWF has the domain structure A1-A2-B-A3-C1-C2 [82, 85]. The A1-A2 domains are present in the heavy chain (HC) with a molecular weight varying between 90 kDa and 200 kDa [84], while the domains A3-C1-C2 form the light chain (LC) with a molecular weight of 76 kDa [86]. A region of the C2 domain contains a membrane binding site of FVIII and the site of interaction with VWF [87]. FVIII circulates as a series of noncovalent heterodimers with VWF, produced by proteolytic cleavage at the B-A3 junction or within the B domain [88].

1.2   Integrin $\alpha_4\beta_7$

Lymphocytes circulating in the blood must leave the bloodstream to enter lymphoid organs or areas of inflammation. This elaborative process, termed lymphocyte extravasation, involves the stages of tethering or rolling, cell activation, firm adhesion, and finally transendothelial migration [90]. When this adhesive process is not under proper control, it can cause severe immune disorders such as psoriasis, multiple sclerosis, and inflammatory bowel diseases (IBD). Among the lymphocyte surface molecules involved in this process, the α_4 integrins (including $\alpha_4\beta_1$ and $\alpha_4\beta_7$) can mediate both rolling and firm adhesion. In this thesis, the integrin $\alpha_4\beta_7$ is used as a kind of complexed protein to demonstrate the application of the newly developed SpyTag

method, as well as a model to further investigate the molecular and biophysical mechanisms underlying cell rolling and firm adhesion mediated by integrins [91].
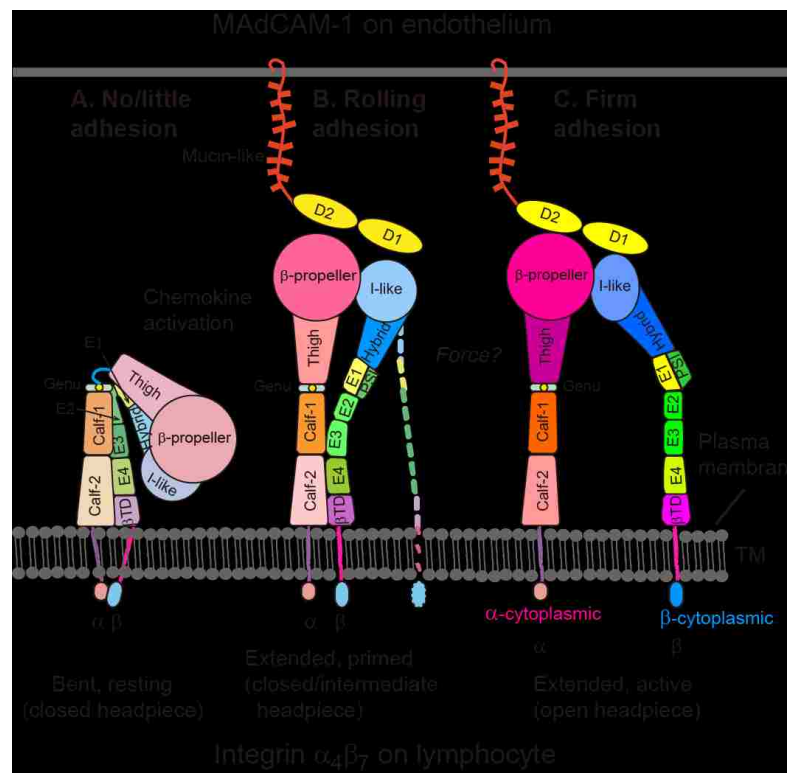
Figure 1.7 Structure of integrin $\alpha_4\beta_7$. Global conformational rearrangements in $\alpha_4\beta_7$ integrin extracellular domains upon activation. The three conformational states of $\alpha_4\beta_7$ and their contributions to lymphocyte-endothelial adhesion are shown. There may be an intermediate headpiece state shown by the broken line.

Integrin $\alpha_4\beta_7$ is a heterodimeric transmembrane molecule, held together by non-covalent association of the α_4 (MW 130–210 kDa) and β_7 (MW 95–130 kDa) subunits (Figure 1.7) [92]. The N-terminal region of the α_4 subunits is made up of seven repeats that form a "β-propeller" structure, which non-covalently associates with a Rossmann folded "I-like domain" in the N-terminus of the β subunit. The I-like domain consists of a metal ion-dependent adhesion site (MIDAS) that binds to negatively charged residues in ligands [93]. $\alpha_4\beta_7$ mediates the homing of lymphocytes to lymphoid tissues by binding MAdCAM-1, the natural ligand for $\alpha_4\beta_7$, expressed on the endothelium in mucosal lymphoid tissues such as lamina propria, Peyer's patches, and mesenteric lymph nodes [94]. MAdCAM-1 has two NH_2-terminal Ig domains (D1 and D2), which

are directly involved in integrin binding, and a more C-terminal, membrane-proximal, mucin-like region (Figure 1.7) [94]. The most crucial interaction in the stabilization of the $\alpha_4\beta_7$–MAdCAM-1 complex appears to be the electrostatic interaction between Asp-42 of domain 1 (D1) of MAdCAM-1 and the chelated Mg^{2+} ion of the β I-like domain [95].

Like most integrins, affinity regulation is an important functional feature of $\alpha_4\beta_7$. On resting lymphocytes, $\alpha_4\beta_7$ mediates transient adhesion or cell rolling, while upon activation by chemokines and intracellular signals, the strength of the $\alpha_4\beta_7$/ligand complex is drastically increased within sub-seconds, resulting in a prolonged lifetime of the $\alpha_4\beta_7$/ligand bond. This activation leads to firm adhesion [96, 97]. Induction of high affinity integrin is proposed to be initiated by the unclasping and separation of the integrin α and β cytoplasmic tails followed by changes in the global conformation of the whole integrin molecule including an axial movement of the C-terminal α_7 of the β I-like domain and a 60° outward swing of the β hybrid domain (Figure 1.7) [93, 98, 99]. Recent studies have shown that lymphocyte rolling is not mediated by the bent integrin conformer, but the extended conformer with a closed head piece. A recent structural study has suggested there might exist additional intermediate head piece states that are less active than the fully open head piece. These physiologically induced alterations in the distinct phases of adhesion can be mimicked by the manipulation of the divalent cation concentrations *in vitro* [100], or mutation of the metal ion binding sites in the β_7 I-like domain [101]. It is unclear if and how chemokine activation is different from cationic activation in terms of the affinity enhancement and structural change.

1.3 SpyTag–SpyCatcher

The methods of tagging the desired protein with peptides (such as His_6, Myc, HA, and FLAG) or biotin have been widely used by researchers for protein immobilization in single-molecule experiments [102–105]. However, the bonds formed in this traditional way are usually non-covalent, which means that the binding has low mechanical strength and is thermal dynamically unstable, and the reaction is reversible. Besides, due to the non-specificity of the bonds, these methods cannot eliminate the non-specific interaction between the protein and the polystyrene bead in a single-molecule system. In the experiments, two different kinds of binding methods at two ends of the protein are usually required to prevent its two ends binding to one site. Recently, Mark Howarth *et al.* [36] proposed a new tagging method where the formation of a rapid covalent bond occurs without using chemical modification, artificial amino acids, or cysteines. They obtained a peptide tag of 13 amino acids (termed SpyTag) by splitting the *Streptococcus pyogenes* CnaB2 domain. The SpyTag is a C-terminal peptide containing amino acid residue Asp117, while the SpyCatcher is an N-terminal protein fragment containing amino acid residue Lys31 [36, 106]. The SpyTag and its partner SpyCatcher associate specifically and spontaneously by forming an isopeptide bond between Lys31 and Asp117 [103, 104, 107]. The bond is a type of covalent bond. A rational modification of the remaining protein fragments from the splitting of CnaB2 is shown in Figure 1.8. This reaction proceeds spontaneously, rapidly, and efficiently. Moreover, the SpyTag/SpyCatcher bonds have a high mechanical stability with a lifetime of more than one day, and a high mechanical strength of 131 pN [36]. The specific binding between SpyTag and SpyCatcher allows potential simplification of single-molecule force spectrum experiments.

16
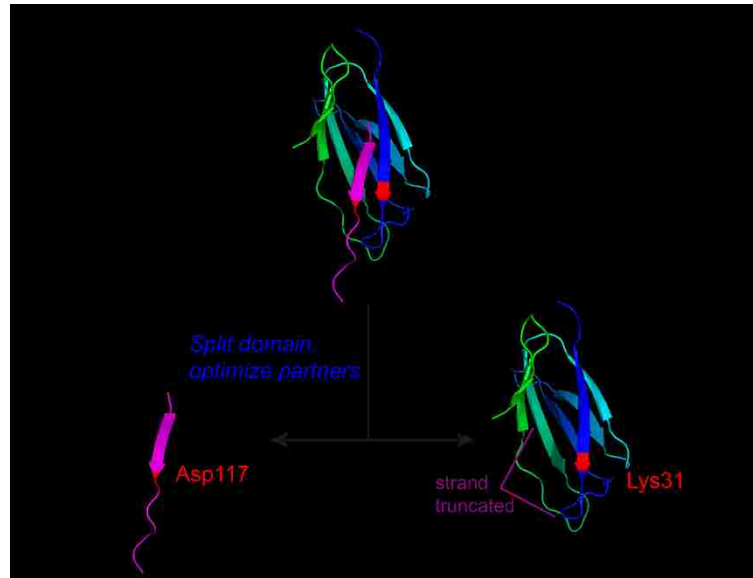
Figure 1.8 SpyTag–SpyCatcher interaction. *Streptococcus pyogenes* (Spy) CnaB2 is split into two fragments, a large N-terminal fragment (SpyCatcher, left) and a smaller C-terminal peptide fragment (SpyTag, right). The SpyTag is a C-terminal peptide containing amino acid residue Asp117, while the SpyCatcher is an N-terminal protein fragment containing amino acid residue Lys31 [36, 106]. The SpyTag and its partner SpyCatcher associate specifically and spontaneously by forming an isopeptide bond between Lys31 and Asp117 [103, 104, 107].

1.4   Single-Molecule Kinetic Mechanisms and Models

Many biological molecules, such as a single-stranded DNA (ssDNA), a double-stranded DNA (dsDNA), a double-stranded RNA (dsRNA) and polypeptides (proteins), display a significant flexibility over long distances, while every small segments remain rigid. To characterize the elastic and mechanical properties of the chain-like biomolecules, the worm-like chain (WLC) model (sometimes referred to as the Kratky–Porod model) is usually utilized. Fitting the force-extension data from the single-molecule pulling experiments to WLC model gives the contour length L_c, the persistence length L_p, and sometimes the elastic stretch modulus S, and the twist rigidity C.

To characterize the natural energy landscape of interactions or different states (usually two states) of molecules, single-molecule pulling experiments are performed

in a force-ramp mode (with constant pulling velocities) or force-clamp mode (with constant pulling forces). Two well-known models, i.e., the Bell–Evans model and the Dudko model, derived from the Kramers theory can be used to extract the following parameters: (1) the spontaneous off/unfolding/refolding/dissociation rate or the intrinsic rate coefficient k_0; (2) the distance between the native state and the transition state along the reaction coordinate, i.e., the location of the transition state or the barrier width $\Delta x^{\ddagger}$; (3) the barrier height or the free energy of activation ΔG.

1.4.1   Worm-Like Chain (WLC) Model

The worm-like chain (WLC) model (sometimes referred to as the Kratky–Porod model) is a continuous model used to characterize the behavior of semi-flexible polymers. Many biological molecules, such as a single-stranded DNA (ssDNA), a double-stranded DNA (dsDNA), a double-stranded RNA and proteins, display a significant flexibility over long distances, while every small segments remain rigid.

It assumes polymers to be an idealized, macroscopic, and circularly-symmetric beam elements with a flexural rigidity. With successive monomers constrained to point in nearly the same direction, the isotropic polymer chain is continuously flexible. It is different from the freely-jointed chain model, which assumes the flexibility only between discrete segments [108, 109]. The WLC model has been widely used in analyzing the elastic and mechanical properties of the chain-like biomolecules, and has developed some variations [11, 31, 110–115].

The basic *inextensible* WLC model describing the relation between the polymer's extension and the applied force is approximated by the following interpolation formula [31]

$$\frac{F(x) \cdot L_p}{k_B T} = \frac{1}{4}\left(1 - \frac{x}{L_c}\right)^{-2} - \frac{1}{4} + \frac{x}{L_c} \tag{1.1}$$

where $F(x)$ is the applied force on the polymer chain, x is the end-to-end distance, L_c is the contour length, L_p is the persistence length of the polymer, k_B is the Boltzmann constant, and T is the absolute temperature. In this formula, the polymer is treated as inextensible and the twisting effect is ignored. In molecular physics, the contour length L_c of a polymer chain is its maximum length when possibly extended, and the persistence length L_p is defined as the length over which correlations in the direction of the tangent are lost, which quantifies the rigidity of the chain. An example of fitting force-extension data to WLC model is shown in Figure 1.9. The figure shows a typical force-extension trace of pulling the glycoprotein Ib-IX complex. Blue line is the approaching trace, and the red line is the retracting trace, i.e., the pulling curve. Two dashed green lines are the WLC fits to two sections of the red pulling curve according to Eq. (1.1). Two different fitted contour lengths from the fittings would give a contour length increment ΔL_c indicating the extension of the unfolding.

In some polymers, the elastic response of the polymers cannot be neglected under stretching. Two *extensible* worm-like chain (eWLC) models were derived depending on the magnitude of the applied force.

For low forces $F < \sim 10$ pN, but has limitations near $F \approx 0.1$ pN), there is the following interpolations formula [111]

$$\frac{F \cdot L_p}{k_B T} = \frac{1}{4}\left(1 - \frac{x}{L_c} + \frac{F}{S}\right)^{-2} - \frac{1}{4} + \frac{x}{L_c} - \frac{F}{S} \tag{1.2}$$

where parameters F, x, L_c, L_p, k_B, and T are the same as these in Eq. (1.1), while the new parameter S is the elastic stretch modulus, which accounts for the enthalpy term.
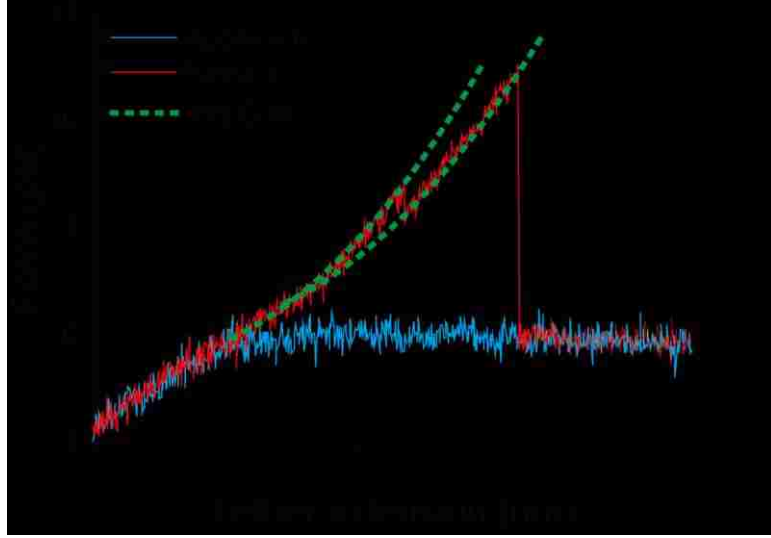
Figure 1.9 An example of fitting the force-extension data to the WLC model. It shows a typical force-extension trace of pulling the glycoprotein Ib-IX complex. Blue line is the approaching trace, and the red line is the retracting trace, i.e., the pulling curve. Two dashed green lines are the WLC fits to two sections of the red pulling curve according to Eq. (1.1). Two different fitted contour lengths from the fittings would give a contour length increment ΔL_c indicating the extension of the unfolding.

For high forces, the following approximation is available [110]

$$x = L_c \left[1 - \frac{1}{2}\left(\frac{k_B T}{F L_p} \right)^{1/2} + \frac{F}{S} \right] \qquad (1.3)$$

where all the parameters are same as these in Eq. (1.2).

To take into account the sequence composition and a force-dependent twist-stretch coupling, a *twistable* worm-like chain (tWLC) model was built by expanding the eWLC model to the following approximation [115]

$$x = L_c \left[1 - \frac{1}{2}\left(\frac{k_B T}{F L_p} \right)^{1/2} + \frac{C}{-g(F)^2 + S \cdot C} \cdot F \right] \qquad (1.4)$$

where F, x, L_c, L_p, k_B, and T are the same as these in Eq. (1.1), C represents the twist rigidity, and $g(F)$ is the twist-stretch coupling [116–118].

1.4.2 Kramers Theory

In 1940, Kramers derived the first theory to calculate the rate of chemical reactions using the Brownian motion model [35, 119]. In this theory, chemical reactions are treated as diffusion problems. Based on a derivation of the Fokker–Planck diffusion equation [120] for the Brownian motion in phase space, in the presence of a nonlinear potential field, Kramers predicted the probability of escape (or called "rate of escape") k depending on the temperature T and the friction γ. In the model of chemical reactions, a classical particle of mass M moves in a one-dimensional asymmetric double-well potential $U(x)$ (Figure 1.10). Along the reaction coordinate x, the particle has minima of potential at x_a and x_c, denoting the reactant and product states, respectively. The local maximum point at x_b separating these states corresponds to the transition state (or activated complex). In this simplified model, all the reacting and solvent molecules constitute a heat bath at temperature T.
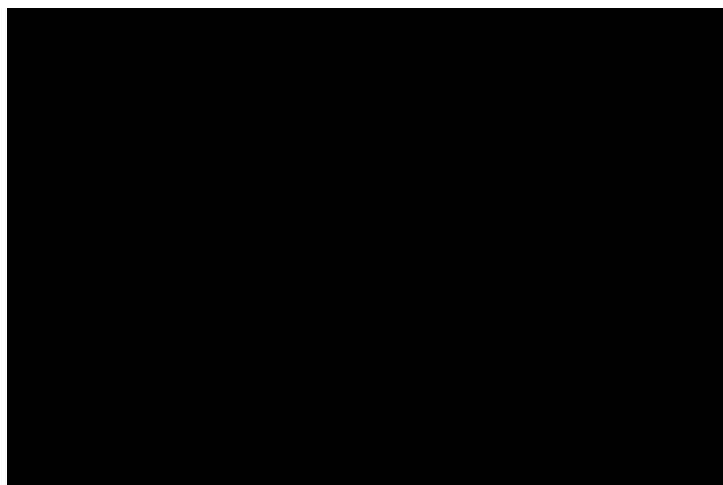
Figure 1.10 Asymmetric potential field with two metastable states. Asymmetric potential field $U(x)$ with two metastable states. There are two metastable wells at x_a and x_c, as well as a transition state at x_b along the reaction coordinate x. Escape occurs via the forward rate k^+, and the backward rate k^-, respectively. E_{b+} and E_{b-} correspond to activation energies. ω_a, ω_b, and ω_c denote the angular frequency at each point, with parameter $\omega_0 = \omega_a$.

For a solvent with strong friction γ (large viscosity), Kramers derived the celebrated result of the escape rate from A to C,

$$k_{A \to C} \equiv k^+ = \frac{(\gamma^2 / 4 + \omega_b^2)^{1/2} - \gamma / 2}{\omega_b} \cdot \frac{\omega_0}{2\pi} \exp(-\beta \cdot \Delta E) \qquad (1.5)$$

where $\omega_0 = \omega_a$, with ω_a and ω_b denoting the angular frequency at position x_a and x_b, respectively; the thermal factor $\beta = 1/(k_B T)$, and the activation energy $\Delta E \equiv E_{b^+} = U(x_b) - U(x_a)$.

In the limit as damping becomes very large (the Smoluchowski limit), i.e., for $\gamma/2 \gg \omega_b$, using Taylor expansion, Eq. (1.5) turns to

$$k_{A \to C} \equiv k^+ = \frac{\omega_0 \omega_b}{2\pi\gamma} \exp(-\beta \cdot \Delta E) \qquad (1.6)$$

which predicts that the rate of escape k decreases inversely proportional to the friction γ.

When friction γ is weak (small viscosity), Eq. (1.5) turns to

$$k_{A \to C} \equiv k^+ = \gamma\beta \cdot \Delta E \cdot \exp(-\beta \cdot \Delta E) \qquad (1.7)$$

1.4.3   Bell–Evans Model

The earliest theory concerning the reaction rate was developed by Arrhenius [121], which is represented by the Van't Hoff–Arrhenius law: rate of dissociation $k = \nu \exp(-E_0/k_B T)$, where ν is the natural frequency of molecular collisions in the collision theory in vacuum, E_0 is the free entropy term in the transition state theory, k_B is Boltzmann constant, and T is the absolute temperature. Later, Kramers derived the analytical formula for the rate of escape, but it was not applied until about thirty years later due to the unavailability of experimental techniques. Kramers presented the reaction kinetics in liquids [35]. In 1978, Bell first proposed the phenomenological model to describe the rate of bond dissociation under external force load [122] by extending the kinetic theory of the strength of solids [123] and the transition state theory

for reactions in gases introduced by Eyring and others [119]. Later Evans refined the theory by deriving the dependence of adhesion (the most probably or most likely rupture force) on the force loading rate [33].

A simple assumption is that the applied external force F acts directly along the reaction coordinate, i.e., the height of the transition-state energy barrier ΔE depends linearly on the applied force F and a constant distance $\Delta x^{\ddagger}$ between the native equilibrium state and the transition state,

$$\Delta E = E_0 - F\Delta x^{\ddagger} \tag{1.8}$$

Based on Eq. (1.8), Evans *et al.* [33] derived the well-known force-dependent dissociation rate:

$$k(F) = \frac{\omega_{min}\omega_{max}}{2\pi\gamma}\exp(-\frac{E_0 - F\Delta x^{\ddagger}}{k_B T}) = k_0 \cdot \exp(\frac{F\Delta x^{\ddagger}}{k_B T}) = k_0 \cdot \exp(\beta F\Delta x^{\ddagger}) \tag{1.9}$$

where ω_{min} represents the angular frequency of the metastable state, ω_{max} is the positive valued angular frequency of the transition state at the barrier, γ is the damping relaxation rate, k_0 is the zero-force natural off rate, k_B is Boltzmann constant, T is the absolute temperature, and $\beta = 1/(k_B T)$.

The force-dependent lifetime of the bonds is the reciprocal of the force-dependent dissociation rate $k(F)$, i.e.,

$$\tau(F) = \tau_0 \cdot \exp(-\beta F\Delta x^{\ddagger}) \tag{1.10}$$

where $\tau_0 = k_0^{-1}$ is the intrinsic lifetime, corresponding to zero external force.

Taking logarithm of Eq. (1.9) and Eq. (1.10) leads to

$$\begin{aligned} \ln k &= \beta\Delta x^{\ddagger} \cdot F + \ln k_0 \\ \ln \tau &= -\beta\Delta x^{\ddagger} \cdot F + \ln \tau_0 \end{aligned} \tag{1.11}$$

We can see that $\Delta x^{\ddagger}$ and τ_0 (or k_0) can be extracted by linear fitting the lifetime-force data from constant-force experiments.

The change of existing bonds N_B with time has the relation with the dissociation rate k:

$$\frac{\mathrm{d}N_B(t)}{\mathrm{d}t} = -k \cdot N_B(t) \tag{1.12}$$

The number of intact bonds $N_B(t)$ is giving by integrating Eq. (1.12)

$$N_B(t) = \exp\left(-\int_0^t k(t')\mathrm{d}t'\right) \tag{1.13}$$

Assuming that the applied force F is a reversible continuous function of time t, t can be replaced by F, yielding the following expression:

$$N_B(t) = \exp\left(-\int_0^F k(f) \cdot \frac{1}{\dot{f}}\mathrm{d}f\right) \tag{1.14}$$

Then the number of dissociated bonds N_D at time t, under applied force F, is given by

$$N_D(t,F) = 1 - N_B(t) = 1 - \exp\left(-\int_0^F k(f) \cdot \frac{1}{\dot{f}}\mathrm{d}f\right) \tag{1.15}$$

The probability $p(F)$ that the bonds break under external force F is given by $\mathrm{d}N_D/\mathrm{d}F$:

$$p(F) = \frac{\mathrm{d}N_D}{\mathrm{d}F}(F) = \frac{k(F)}{\dot{F}(F)} \cdot \exp\left(-\int_0^F \frac{k(f)}{\dot{F}(f)}\mathrm{d}f\right) \tag{1.16}$$

where $\dot{F}(F) = \mathrm{d}F/\mathrm{d}t$ is called the force loading rate [122]. It can be proved that $\int_0^\infty p(F)\mathrm{d}F = 1$. In the Bell–Evans model, substituting Eq. (1.9) into Eq. (1.16) leads to

$$p(F)_{B-E} = \frac{k_0}{\dot{F}}\exp\left(\beta F\Delta x^{\ddagger}\right) \cdot \exp\left(-k_0 \int_0^F \frac{1}{\dot{F}}\exp\left(\beta F\Delta x^{\ddagger}\right)\right) \tag{1.17}$$

Therefore, the most probable rupture force F^* can be obtained by the derivation:

$$\left.\frac{\mathrm{d}p(F)}{\mathrm{d}F}\right|_{F=F^*} = 0 \tag{1.18}$$

Assuming that the force loading rate $\dot{F}$ is independent of the applied force F, like the situation in constant pulling speed experiments, a linear dependence of F^* on the logarithm of the loading rate $\dot{F}$ is predicted:

$$F^*(\dot{F}) = \frac{1}{\beta\Delta x^{\ddagger}}\ln(\frac{\beta\Delta x^{\ddagger}}{k_0}\dot{F}) = \frac{1}{\beta\Delta x^{\ddagger}}\ln(\dot{F}) + \frac{1}{\beta\Delta x^{\ddagger}}\ln(\frac{\beta\Delta x^{\ddagger}}{k_0}) \qquad (1.19)$$

According to Eq. (1.19), we can extract the single-molecule kinetic information, i.e., the spontaneous dissociation rate k_0 and the location of the transition state $\Delta x^{\ddagger}$, when given the distribution of the rupture forces and the corresponding loading rates. That is

$$\Delta x^{\ddagger} = \frac{k_B T}{m}$$
$$k_0 = \frac{1}{m}\exp(-\frac{b}{m}) \qquad (1.20)$$

where m and b denote the slope and the y-intercept from the linear fitting of F^* to $\ln\dot{F}$ using least squares.

Sometimes flexible linkers are used in the pulling experiments, the force loading rate under investigation is continuously changing when stretching the molecule. In this situation, the assumption of independence between $\dot{F}$ and F is not fulfilled, then Eq. (1.19) is only an approximate description.

It is also reported that the mean force $\bar{F}$ and the median force F_m from the distribution can be used to extract the kinetic parameters $\Delta x^{\ddagger}$ and k_0 [124, 125], with

$$\bar{F} = \int_0^{\infty} F \cdot p(F)\mathrm{d}F$$
$$S(F)|_{F=F_m} = \frac{1}{2} \qquad (1.21)$$

Recently in 2013, Sergey Sekatskii *et al.* [126] proposed one way of first-order correction to the Bell–Evans model. In the Bell–Evans model, Eq. (1.8) was used with the assumption of linear independence of the barrier height ΔE on the applied force F and a barrier width $\Delta x^{\ddagger}$ between the native equilibrium state and the transition state,

25

which requires a special shape of the interaction landscape. They employed an approximation of any interaction potential shape by first two terms of the Taylor expansion, i.e., $U_{min} = a_{min}x^2 + b_{min}x^3 + O(x^4)$ and $U_{max} = a_{max}x^2 + b_{max}x^3 + O(x^4)$, and obtained the most probable bond rupture force

$$F^*(\dot{F}) = \frac{1}{\beta\Delta x^\ddagger}\left(1 - \frac{C}{\beta\Delta x^\ddagger}\right)\left(\ln(\frac{\beta\Delta x^\ddagger}{k_0}\dot{F}) + \frac{C}{\beta\Delta x^\ddagger}\right) \tag{1.22}$$

where $C = 3b_{min}/(4a_{min}^2) + 3b_{max}/(4a_{max}^2)$, substituting $\tilde{B} = \beta\Delta x^\ddagger/C$ into Eq. (1.22) gives

$$F^*(\dot{F}) = \frac{1}{\beta\Delta x^\ddagger}\left(1 - \frac{1}{\tilde{B}}\right)\ln\dot{F} + \frac{1}{\beta\Delta x^\ddagger}\left(1 - \frac{1}{\tilde{B}}\right)\left(\ln(\frac{\beta\Delta x^\ddagger}{k_0}) + \frac{1}{\tilde{B}}\right) \tag{1.23}$$

with the condition $C \cdot F^* \ll 1$, i.e., $F^* \ll |\tilde{B}|/\beta\Delta x^\ddagger$. With a rough estimation of $\Delta x^\ddagger$ ~0.1 nm [127-130], and $|\tilde{B}|$ ~10, the most probable force should be smaller than 400 pN [126]. When $C = 0$, Eq. (1.23) turns to be the Bell–Evans law (Eq. (1.8)).

They [126] also reported the mean rupture force $\langle F \rangle$ in the approximation: for positive C,

$$\langle F \rangle = \frac{1}{\beta\Delta x^\ddagger}\left(1 - \frac{1}{|\tilde{B}|}\right)\ln\dot{F} + \frac{1}{\beta\Delta x^\ddagger}\left(1 - \frac{1}{|\tilde{B}|}\right)\ln\frac{\beta\Delta x^\ddagger}{k_0} + \frac{1}{\beta\Delta x^\ddagger}\left(-\gamma + \frac{\ln|\tilde{B}|}{|\tilde{B}|}\right) \tag{1.24}$$

and for negative C,

$$\langle F \rangle = \frac{1}{\beta\Delta x^\ddagger}\left(1 + \frac{1}{|\tilde{B}|}\right)\ln\dot{F} + \frac{1}{\beta\Delta x^\ddagger}\left(1 + \frac{1}{|\tilde{B}|}\right)\ln\frac{\beta\Delta x^\ddagger}{k_0} + \frac{1}{\beta\Delta x^\ddagger}\left(-\gamma - \frac{\ln|\tilde{B}|}{|\tilde{B}|}\right) \tag{1.25}$$

where $\gamma = 0.5772 \ldots$ is the Euler–Mascheroni constant.

The variance of mean rupture force is

$$\sigma_F^2 = \langle F^2 \rangle - \langle F \rangle^2 = \frac{\pi^2}{6}\left(\beta\Delta x^?\right)^{-2} \tag{1.26}$$

There are also some new unified systematic theories considering the influence of fast force loading rates, such as one described in [131].

1.4.4 Dudko Model

Based on the Kramers theory and certain scaling laws obtained by Garg [132] for high forces, Dudko *et al.* [133] built a unified framework for extracting kinetic information from single-molecule force spectroscopy experiments, which is also a phenomenological theory.
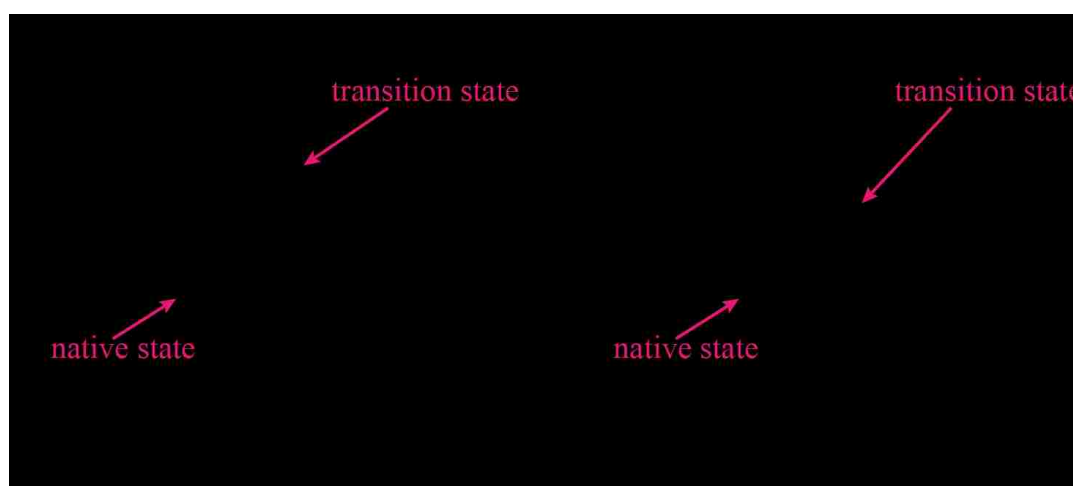
Figure 1.11 Effect of the applied external force on a single-well free-energy surface. (A) Intrinsic free-energy surface $U_0(x)$ with barrier width $\Delta x^{\ddagger}$ between the native state and the transition state along the reaction coordinate, activation free energy ΔG, and inflection point x^*; (B) The activation energy $\Delta U(F)$ of the combined free-energy surface decreases, $U(x) = U_0(x) - Fx$, due to the presence of an external force F, and the reaction rate $k(F)$ will increase (larger than spontaneous reaction rate k_0).

In the model, a molecule moves on a combined free-energy surface, with potential

$$U(x) = U_0(x) - Fx \qquad (1.27)$$

along the pulling direction x, where $U_0(x)$ is the free energy, and F is the exerted pulling force. In single-well model, $U_0(x)$ has a lowest single well at $x = 0$, and a barrier at $x = \Delta x^{\ddagger}$ of height ΔG. Under an external force F, the barrier height $\Delta U(F)$ decreases, shown in Figure 1.11.

From Kramers theory [35], the force-dependent off rate k for sufficiently high potential barriers is predicted as

$$k / k_0 = [\int_{\text{well}} e^{-U(x)} \mathrm{d}x \int_{\text{barrier}} e^{U(x)} \mathrm{d}x]^{-1} \cdot [\int_{\text{well}} e^{-U_0(x)} \mathrm{d}x \int_{\text{barrier}} e^{U_0(x)} \mathrm{d}x] \qquad (1.28)$$

For constant speed experiments (force-ramp mode), the external pulling force is $F(t) = K \cdot vt$, where K is the spring constant for the stiff molecular system. The combined free-energy surface is given by

$$U(x) = U_0(x) + K(x - vt)^2 / 2 \approx U_0(x) - Kvtx = U_0(x) - Fx \qquad (1.29)$$

using the first-order Taylor expansion for a soft effective spring $K \ll 2\Delta G / \Delta x^{\ddagger 2}$.

Substituting Eq. (1.29) to Eq. (1.28) gives

$$k / k_0 = [\int_{\text{well}} e^{-U_0(x)+Fx} \mathrm{d}x \int_{\text{barrier}} e^{U_0(x)-Fx} \mathrm{d}x]^{-1} \cdot [\int_{\text{well}} e^{-U_0(x)} \mathrm{d}x \int_{\text{barrier}} e^{U_0(x)} \mathrm{d}x] \qquad (1.30)$$

To get an analytical formulation for k, two single-well model free-energy surfaces $U_0(x)$ are considered, where the force grows linearly with time:

The cusp surface [134]:

$$U_0(x) = \begin{cases} \Delta G(x / \Delta x^{\ddagger})^2, & \text{for } x < \Delta x^{\ddagger} \\ -\infty & , \quad \text{for } x \geq \Delta x^{\ddagger} \end{cases} \qquad (1.31)$$

The linear-cubic surface:

$$U_0(x) = \frac{3}{2} \Delta G(x / \Delta x^{\ddagger}) - 2\Delta G(x / \Delta x^{\ddagger})^3 \qquad (1.32)$$

The force-dependent dissociation rate $k(F)$ can be derived in a unified form [133]:

$$k(F) = k_0 \left(1 - \frac{\nu F \Delta x^{\ddagger}}{\Delta G} \right)^{1/\nu - 1} \cdot \exp\{\beta \Delta G [1 - (1 - \frac{\nu F \Delta x^{\ddagger}}{\Delta G})^{1/\nu}]\} \qquad (1.33)$$

In this expression, k_0, $\Delta x^{\ddagger}$, and ΔG are the intrinsic off rate, the distance between the native state and the transition state along the reaction coordinate, and the apparent free energy of activation in the absence of an external force, respectively. ν is a scaling

factor, which specifies different kinds of free-energy surface profile. For $v = 1/2$, formula (1.33) corresponds to the cusp surface described by Eq. (1.31), either a harmonic well or barrier; for $v = 2/3$, formula (1.33) corresponds to the linear-cubic surface described by Eq. (1.32); for $v = 1$, formula (1.33) returns to the Bell–Evans' formula, exactly the same as Eq. (1.19), which means that the Bell–Evans model is a special case of Dudko model.

The lifetime $\tau(F) = k(F)^{-1}$ is given by

$$\tau(F) = \tau_0 \left(1 - \frac{v F \Delta x^{\ddagger}}{\Delta G} \right)^{1-1/v} \cdot \exp\{-\beta \Delta G[1-(1-\frac{v F \Delta x^{\ddagger}}{\Delta G})^{1/v}]\} \qquad (1.34)$$

If ΔG is calculated in unit of $k_B T$, expression (1.34) changes to

$$\tau(F) = \tau_0 \left(1 - \frac{v \beta F \Delta x^{\ddagger}}{\Delta G} \right)^{1-1/v} \cdot \exp\{-\Delta G[1-(1-\frac{v \beta F \Delta x^{\ddagger}}{\Delta G})^{1/v}]\} \qquad (1.35)$$

where τ_0 is the intrinsic lifetime of the bonds.

Taking the logarithm of each side of Eq. (1.33) or Eq. (1.34) gives the following new equation:

$$\ln(\tau) = \ln(\tau_0) + (1-1/v)\ln\left(1 - \frac{v F \Delta x^{\ddagger}}{\Delta G} \right) - \beta \Delta G \left[1 - \left(1 - \frac{v F \Delta x^{\ddagger}}{\Delta G} \right)^{1/v} \right] \qquad (1.36)$$

which is not a simple linear equation like Bell–Evans model (Eq. (1.19)). This equation is valid only when the rupture force F is below a critical force $F_c = \Delta G / (v \Delta x^{\ddagger})$, where the barrier vanishes, or Eq. (1.36) would involve complex values due to the logarithm function.

In the Dudko model, Eq. (1.34) or Eq. (1.36) is used to extract the kinetic properties, including k_0 (or τ_0), $\Delta x^{\ddagger}$, and ΔG. In a single-molecule experiment, either pulling with a constant speed (force-ramp mode) or a constant force (force-clamp mode), $k(F)$ (or $\tau(F)$) and F can be obtained directly or indirectly from the experimental results.

29

Under the quasi-adiabatic approximation, the transformation from constant speed experiments to constant-force experiments is given by [34, 133, 135]

$$\tau(F) = \frac{\int_F^\infty p(f \mid v)\mathrm{d}f}{\dot{F}(F \mid v) \cdot p(F \mid v)} \tag{1.37}$$

where $p(F|v)$ is the rupture-force probability density distribution measured at the constant pulling speed v, $\tau(F)$ is the lifetime at the constant force F, and $\dot{F}(F|v)$ is the loading rate at the speed v. This transformation is applicable to all kinds of underlying free-energy surface. For each pulling speed v (or loading rate $\dot{F}(F)$), a set of $(F, \tau(F))$ pairs are obtained according to Eq. (1.37), and it is predicted that different sets of $(F, \tau(F))$ from different speeds, should collapse onto one single master curve over a wide range of rupture forces.

Consider an experimental rupture-force histogram obtained at a constant speed v, the histogram has N bins of width $\Delta F = (F_{\max} - F_{\min})/N$. The number of counts in the ith bin is c_i, $1 \le i \le N$, then the total counts is $C = \sum_{i=1}^{N} c_i$, resulting in the probability $P(F_i) = c_i/C$, and the density $p(F_i) = c_i/(C \cdot \Delta F)$. Thus, substituting to Eq. (1.37) leads to (the Dudko–Hummer–Szabo equation)

$$\tau(F_i) = \frac{\left(p(F_i)/2 + \sum_{k=i+1}^{N} p(F_i) \right) \cdot \Delta F}{\dot{F}(F_i) \cdot p(F_i)} \tag{1.38}$$

where $F_i = F_{\min} + \left(i - \frac{1}{2} \right) \Delta F$, for $1 \le i \le N - 1$; $\tau(F_N) = \frac{p(F_N)/2 \cdot \Delta F}{\dot{F}(F_N) \cdot p(F_N)} = \frac{\Delta F}{2\dot{F}(F_N)}$, for $i = N$.

A quite general approximation of the relationship between the lifetime at the mean rupture force and the variance of the rupture-force distribution is given by [34]

$$\tau(\langle F \rangle) \approx \left[\frac{\pi}{2} (\langle F^2 \rangle - \langle F \rangle^2) \right]^{1/2} / \dot{F}(\langle F \rangle) \tag{1.39}$$

This expression is derived from Eq. (1.37) by approximating the rupture-force distribution $p(F)$ as a normalized Gaussian distribution, and setting the rupture force $F = \langle F \rangle$. Actually, the real rupture-force distribution is not well described by the Gaussian distribution over the entire range of rupture forces, but the approximation of the lifetime at the mean force turns to be quite good. It is said that $\tau(F)$ from this relation can be derived from the highly non-Gaussian rupture-force distribution, with a numerical coefficient differing by <10% [34, 133].

Another simple approach for data set with substantial outliers is given by [34]

$$\tau(\langle F \rangle) \approx \frac{3}{4} \delta F / \dot{F}(\langle F \rangle) \tag{1.40}$$

where $\langle F \rangle$ is the mean force, and $\delta F = F_3 - F_1$ is the interquartile range, i.e., 25% of the rupture forces are higher than F_3 and 25% are lower than F_1.

The disadvantage of using these two approximations is that experiments on different pulling speeds are required to get a good fit between rupture forces and lifetimes, since only one pair of $(\langle F \rangle, \tau \langle F \rangle)$ can be extracted from one constant-speed experiment.

After getting data set $(F, \tau(F))$, non-linear least-squares fitting to logarithm of $\tau(F)$ in Eq. (1.36) on force F with several values of v to estimate τ_0, $\Delta x^{\ddagger}$, and ΔG. If the fitting values of the tree parameters are insensitive to v over a v range which still lead to good fits, they are considered to be meaningful due to the independence of the exact profile of the free-energy surface.

It is further preferred to consider the wellness of fitting results, by comparing the predicted force distribution with the experimental one. They started from the same equation in the Bell–Evans model (Eq. (1.16))

$$p(F) = -\frac{dS(F)}{dF} = \frac{k(F)}{\dot{F}(F)} \cdot \exp\left(-\int_0^F \frac{k(f)}{\dot{F}(f)} \, df\right)$$

31

Here, $S(F)$ is the bond survival probability that the molecular system keeps intact at time t.

For constant pulling speed experiments, Eq. (1.16) can be converted to

$$p(F \mid v) = \frac{1}{\dot{F}(F)\tau(F)} \frac{\exp\left[\beta(\dot{F}(F)\tau_0 \Delta x^{\ddagger})^{-1}\right]}{\exp\left[\beta(\dot{F}(F)\tau(F)\Delta x^{\ddagger})^{-1}(1 - \frac{vF\Delta x^{\ddagger}}{\Delta G})^{1-1/v}\right]} \qquad (1.41)$$

For small loading rate $\dot{F}$, the mean rupture force $\langle F \rangle$ and the variance σ_F^2 are given asymptotically by [132, 133]

$$\langle F \rangle \cong \frac{\Delta G}{v \Delta x^{\ddagger}}\left[1 - \left(\frac{1}{\Delta G} \ln \frac{\exp(\Delta G + \gamma)}{\dot{F}\tau_0 \Delta x^{\ddagger}}\right)^{v}\right]$$

$$\sigma_F^2 \cong \frac{\pi^2}{6\Delta x^{\ddagger 2}}\left(\frac{1}{\Delta G} \ln \frac{\exp(\Delta G + \tilde{\gamma})}{\dot{F}\tau_0 \Delta x^{\ddagger}}\right)^{2v-2} \qquad (1.42)$$

where $\gamma = 0.5772\ldots$ is the Euler–Mascheroni constant, $\psi''(1) = -2.404\ldots$ is a particular value of the tetragamma function, and $\tilde{\gamma} = \gamma^2 - 3/\pi^2 \psi''(1) \approx 1.064$ [133, 136]. For $v = 1$ corresponding to the phenomenological theory, the variance σ_F^2 is independent of the pulling speed v. Therefore, the phenomenological approach is invalid if the experimental variance changes for different pulling speeds.

Figure 1.12 shows an example of using the Dudko model to analyze the experimental data. Experimental data is from the pulling of polyprotein (GB1)$_8$ in PBS buffer with 0M GdmCl and 30% glycerol, at a variety of velocities (~0.1 μm/s, ~0.2 μm/s, ~0.5 μm/s, ~1 μm/s, ~2 μm/s) using AFM [137]. The symbols of same color (red, yellow, blue, puple, and green) are from the same pulling speed. At each pulling speed, several $(F, \tau(F))$ pairs are obtained by transforming the unfolding force histogram (inset) according to Eq. (1.38). It can be seen that these $(F, \tau(F))$ pairs from different pulling speeds do collapse onto a same master curve. Least squares fitting (black line) to the data yields the estimations of τ_0, $\Delta x^{\ddagger}$, and ΔG, which are further used to predict

the force histograms. The inset is an unfolding force histogram measured at speed $v =$ 520 nm/s. Using the parameters from the fitting to the Dudko model, we obtain the predicted force distribution (inset, red line), which agrees well with the experimental one.
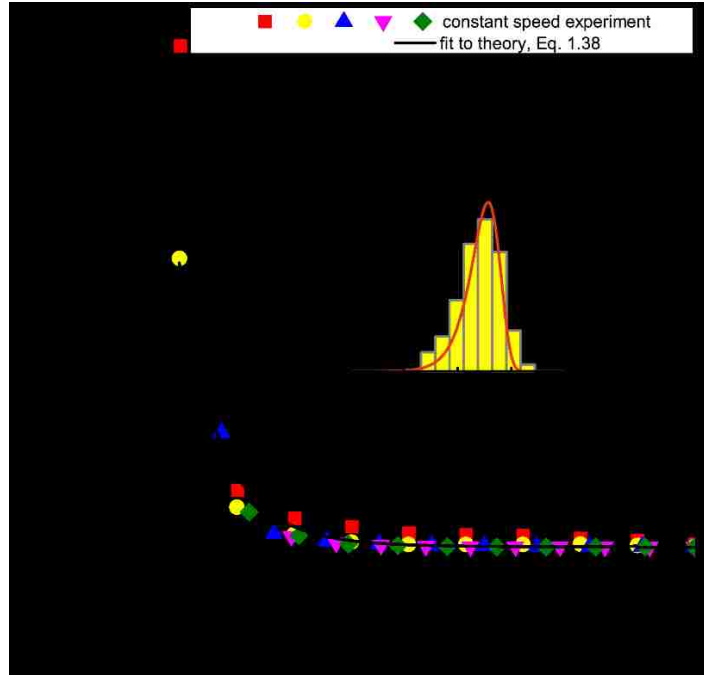
Figure 1.12 An example of the application of the Dudko model. Experimental data is from the pulling of polyprotein (GB1)$_8$ in PBS buffer with 0M GdmCl and 30% glycerol, at a variety of velocities (~0.1 μm/s, ~0.2 μm/s, ~0.5 μm/s, ~1 μm/s, ~2 μm/s) using AFM [137]. The symbols of same color (red, yellow, blue, puple, and green) are from the same pulling speed. At each speed, several $(F, \tau(F))$ pairs are obtained from the transformation of the unfolding force histogram (inset) according to Eq. (1.38). It can be seen that these $(F, \tau(F))$ pairs from different pulling speeds do collapse onto a same master curve. Least squares fitting (black line) to the data yields the estimations of τ_0, $\Delta x^{\ddagger}$, and ΔG, which are further used to predict the force histograms. The predicted force distribution (inset, red line) agrees well with the experimental one.

In AFM experiments, the force loading rate $\dot{F} = \mathrm{d}F/\mathrm{d}t = Kv$ is independent of F, when the linker effect is neglected. However, some experimental systems use intervening flexible linkers, like DNA handles, then the loading rate is a function of the applied force, i.e., $\dot{F} = \dot{F}(F)$. Considering the pulling process as a simple force-balance process, the force-dependent loading rate $\dot{F}(F)$ is given by [138]

$$\frac{1}{\dot{F}(F)} = \frac{1}{vK} + \frac{1}{v}\frac{\mathrm{d}l(F)}{\mathrm{d}F} \tag{1.43}$$

where v is the pulling velocity, K is the spring constant of cantilever in AFM experiments, $l(F)$ is the force-dependent extension of the linker.

For the WLC model, the extension $l(F)$ of the flexible linker is approximately the solution of Eq. (1.1)

$$\frac{F(x) \cdot L_p}{k_B T} = \frac{1}{4}\left(1 - \frac{l(F)}{L_c}\right)^{-2} - \frac{1}{4} + \frac{l(F)}{L_c}$$

where F is the applied force, L_c is the contour length, and L_p is the persistence length of the WLC linker. By taking into account the first two terms in the low-force expansion of dl/dF with the limit $F \to \infty$, an approximate analytical Padé-like expression for the force-dependent loading rate $\dot{F}$ is given by [34]

$$\dot{F}(F) = v\left[\frac{1}{K} + \frac{2\beta L_c L_p (1 + \beta F L_p)}{3 + 5\beta F L_p + 8(\beta F L_p)^{5/2}}\right]^{-1} \tag{1.44}$$

We can see that the second factor in the right hand side accounts for the link effect. If this part is ignored, the expression turns to the simple one $\dot{F} = Kv$. It is reported that this expression is accurate to within ~3.5% [34].

For the analogous expression for a freely jointed chain (FJC), the force-dependent loading rate $\dot{F}$ is given by Ray *et al.* [138]

$$\dot{F}(F) = Kv\left\{1 + \frac{KL_c}{F_K}\left[\left(\frac{F_K}{F}\right)^2 - \operatorname{csch}^2\left(\frac{F}{F_K}\right)\right]\right\}^{-1} \tag{1.45}$$

where L_c is the contour length of the linker, K is the cantilever spring constant in AFM experiments, and the parameter $F_K = k_B T / a$ where a is the Kuhn length of the linker. It is also noticeable that the loading rate approaches Kv under conditions of high force F, a short linker L_c, or a small spring constant K.

Both the Bell–Evans model and the Dudko model are derived from Kramers theory, and both are phenomenal approaches. A comparison between the two models is shown in Table 1.1.

Table 1.1 Comparison between the Bell–Evans model and the Dudko model.

	Bell–Evan model	Dudko model
Expression	force-ramp: $F^* = \dfrac{1}{\beta\Delta x^{\ddagger}}\ln\dot{F} + \dfrac{1}{\beta\Delta x^{\ddagger}}\ln\left(\dfrac{\beta\Delta x^{\ddagger}}{k_0}\right)$ force-clamp: $\ln\tau = -\beta\Delta x^{\ddagger}\cdot F + \ln\tau_0$	$\tau = \tau_0\left(1 - \dfrac{\nu F\Delta x^{\ddagger}}{\Delta G}\right)^{1-1/\nu}\cdot\exp\left\{-\beta\Delta G\left[1 - \left(1 - \dfrac{\nu F\Delta x^{\ddagger}}{\Delta G}\right)^{1/\nu}\right]\right\}$
Parameters (*known*)	force-ramp: β, $\dot{F}$, F^* force-clamp: β, F, τ	β, F, τ ν is preset to 1/2, 2/3 or 1
Parameters (*unknown*)	$\Delta x^{\ddagger}$, k_0 (or τ_0)	$\Delta x^{\ddagger}$, τ_0, ΔG
Law	force-ramp: $F^* \propto \ln\dot{F}$ force-clamp: $\ln\tau \propto F$	τ or $\ln\tau$ is nonlinearly related to F and $\ln F$
Fitting methods	least-squares linear fitting (simple)	least-squares nonlinear fitting or Bayesian inference (complicated)
Force-ramp experiments	various pulling speeds for $(\dot{F}, F^*)$ pairs from the force histograms	one pulling speed for (F, τ) pairs from the transformation of the force histogram (Eq. (1.38))
Force-clamp experiments	various constant forces for (F, τ) pairs	same as these in the Bell–Evans model

In this Table, F, $\dot{F}$ and F^* denote the force, the force loading rate, and the most probable force, respectively; k, k_0, τ, and τ_0 denote the off rate under force, the spontaneous off rate, the lifetime under force, and the intrinsic lifetime, respectively; $\Delta x^{\ddagger}$ and ΔG denote the barrier width and height, respectively; ν is a scaling factor indicating different kinds of free-energy surface profile, and $\beta = (k_B T)^{-1}$ is a constant.

1.5 Single-Molecule Force Measurements

Single-molecule experiments are designed and carried out to measure the mechanical and biological properties of proteins, and molecular interactions [1, 2, 133]. A wide variety of single-molecule manipulation techniques have been developed since about fifty years ago, including atomic force microscopy (AFM) [4–8], optical tweezers [9–19], magnetic tweezers [20–27], and biomembrane force probes (BFP) [28–30].

There are some good reviews about these different techniques [22, 139–141]. Fluorescence resonance energy transfer (FRET) is also a widely used technique in biological and biophysical fields. Though FRET does not measure the force, its function of imaging can be used to measure the conformational changes of proteins [142], to detect the molecular interactions [143], and to obtain the information about metabolic or signaling pathways [144]. A summary of the technical features of the three force spectroscopy techniques, including AFM, optical tweezers, and magnetic tweezers, and the imaging technique FRET is shown in Table 1.2.

Table 1.2 Comparison of different single-molecule techniques

	AFM	Optical Tweezers	Magnetic Tweezers	FRET
Spatial resolution (nm)	0.5–1	0.1–2	5–10	0.01–0.1
Temporal resolution (s)	10^{-3}	10^{-3}–10^{-4}	10^{-1}–10^{-2}	10^{-10}–10^{-9}
Stiffness ($pN·nm^{-1}$)	10–10^5	0.005–1	10^{-3}–10^{-6}	—
Force range (pN)	10–10^4	0.1–10^2	10^{-3}–10^2	—
Displacement range (nm)	0.5–10^4	0.1–10^5	5–10^4	1–10
Time scale (s)	10^{-3}–10^2	10^{-4}–10^3	10^{-3}–10^5	—
Probe size (μm)	100–250	0.25–5	0.5–5	—
Typical applications	High-force pulling and interaction assays	3D manipulation Tethered assay Interaction assay	Tethered assay DNA topology	Imaging
Features	High-resolution imaging High force range Active force clamp	Low noise and drift Dumbbell geometry Active/passive force clamp	Force clamp Bead rotation Specific interactions	Fast and high-resolution imaging
Limitations	Large high-stiffness probe Large minimal force Random attachment geometries	Photodamage Sample heating Bulky handles	Difficult to manipulate molecule Large particles Bulky handles	The optical spatial resolution by the Rayleigh criterion

In this table, the properties of AFM, optical tweezers, and magnetic tweezers are summarized from ref. [22, 141]. The properties of FRET are summarized from ref. [145–147].

1.5.1 Mini-Optical Tweezers

Our lab owns a mini-optical tweezers apparatus, which can measure forces as high as 150 pN, with sub-piconewton force resolution, sub-nanometer distance resolution, and 1 millisecond time resolution. The scheme of mini-optical tweezers is shown in Figure 1.13. The fundamental principle is that, a light beam carries momentum flux, and generates a force $F = d\mathbf{P}/dt = W/v$ when it is absorbed, where W is the power of the light beam and $v = c/n$ is the speed of light in the medium. When a light beam is refracted by an object, its momentum changes with the change in beam direction, thus exerting a force with an equal magnitude and an opposite direction to that of the momentum change on the object. The object, usually a transparent particle of high refractive index like a polystyrene micro-bead, is trapped at a laser focus by virtue of the way it refracts the photons and changes their momenta. When the trapped sphere deviates its equilibrium trap position (at the light focus) under an external force F, the flux of light exiting the back side of the trap will undergo a change equal to the force, and the sphere will leave the light focus center to sustain the force balance. After performing the force and distance calibration of the mini-tweezers system, we are able to obtain the relationship between the external force and the distance deviation from the light focus center.

In the mini-optical tweezers system, there are two main parts. The first one is the optical laser system, where a counter-propagating beam geometry is used to form a symmetric trap with 2 lasers focused to the same point. The other one is the well-

designed reaction chamber with three channels. The top and bottom channels are used for injecting micro-spheres (usually $d = 2$ μm), where experimental constructs are coated. The middle channel provides the zone and buffer solution for reactions. During an experiment, one micro-spherical bead is sucked on the tip of the micropipette, and is immobilized, while the other bead is captured by the optical trap and controlled to move back and forward to make contact with the first bead. The two kinds of beads are coated with proteins or other constructs, depending on different experimental systems.

The optical tweezers have a high advantage in the resolutions of force, distance, and time. They allow to perform single-molecule force measurements in both the force-ramp mode and the force-clamp mode, through different settings of the software.
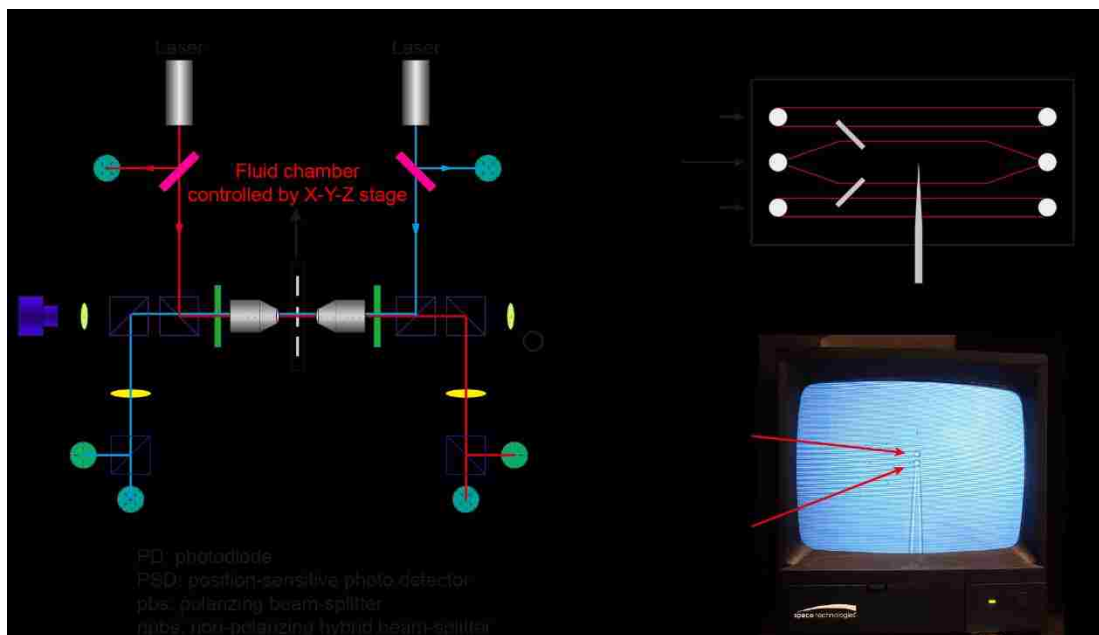
Figure 1.13 Mini-optical tweezers system. (A) Schematic diagram of the mini-optical tweezers system. A counter-propagating beam geometry is used to form a symmetric trap with two lasers focused to the same point. The position and force information is measured by the position-sensitive photo detector (PSD). (B) The chamber for single-molecule experiments. The chamber have three channels. One kind of bead is injected into the top channel, passes to the middle channel through the pipeline, and is captured by the optical trap. Then it is brought to the position of the micropipette, and sucked by the micropipette. Another kind of bead is injected into the bottom channel, and is captured by the trap in a similar way. The bead is further controlled by the trap to move in retract-approach cycles. (C) A photo of the CCD screen from the experiment. It shows that one bead is captured by the optical trap, and another bead is sucked by the micropipette.

1.5.2   Atomic Force Microscopy (AFM)

We also use on a home-built atomic force microscopy (AFM) for single-molecule force measurements, shown in Figure 1.14. In this AFM system, a beam of laser is reflected by the backside of the sensitive cantilever and detected by a position sensitive detector (PSD) with two closely spaced photodiodes. A deformation of the cantilever happens when it presses on a hard surface of the substrate or a tether is picked up by the cantilever tip. The difference in the signal measured by the photodiodes is proportional to the angular displacement of the cantilever, and then converted to force after the calibration of the cantilever. The displacement and pulling speed are controlled by the piezo. The time information can also be controlled and recorded. For the AFM experiments, we use a fast-speed camera (The Imaging Source DMK 21AF04.AS) to help locate the cantilever and align the laser.
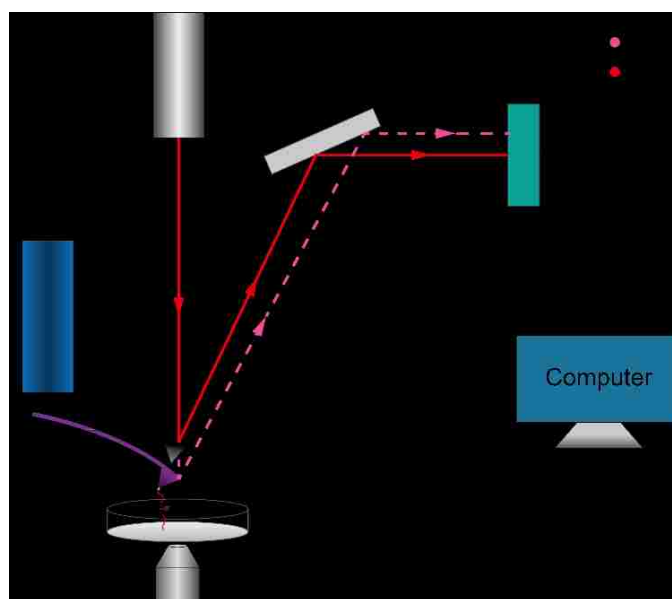
Figure 1.14 Schematic diagram of the home-built AFM. A beam of laser (red line) is reflected by the backside of the sensitive cantilever and detected by a position sensitive detector (PSD) with two closely spaced photodiodes. A deformation of the cantilever happens when it presses on a hard surface of the substrate or a tether is picked up by the cantilever tip. The difference in the signal measured by the photodiodes is proportional to the angular displacement of the cantilever, and then converted to force after the calibration of the cantilever. The displacement and pulling speed are controlled by the piezoelectric actuator.

To avoid the shifting of the gold-coated coverslip, vacuum grease is placed on its bottom. The holder where the cantilever is fixed is controlled by the piezoelectric actuator. The piezoelectric actuator brings the holder down to approach and press the coverslip's surface. By setting a trigger signal, the piezo state will stop to avoid damaging the cantilever. At this point, we can set a contact time, also called dwell time, to obtain a higher probability for the cantilever tip binding to the sample (usually 1 s to 5 s). The part of the protein that is picked up by the tip is random. The setting of dwell time depends on each experiment, and too long of a dwell time will require significantly more time to finish, especially when the pulling speed is very low (~0.1 μm/s). Then the cantilever moves upward to retract within a distance of Z range. We are able to observe the conformational changes (such as unfolding and refolding) of the protein samples, or the unbinding of bonds.

Though the optimized mini-optical tweezers have many advantages over traditional AFM, they cannot reach high external forces. That is to say, when we want to measure high unbinding or rupture forces of bonds/interactions, we have to use AFM to obtain the information.

Chapter 2: Identification of a Juxtamembrane Mechano-sensitive Domain in the Platelet Mechanosensor Glycoprotein Ib-IX Complex

How glycoprotein (GP) Ib-IX complex on the platelet surface senses the blood flow through its binding to the plasma protein von Willebrand factor (VWF) and transmits a signal into the platelet remains unclear. In this chapter, I will show that optical tweezers-controlled pulling of the A1 domain of VWF (VWF-A1) on GPIb-IX captured by its cytoplasmic domain induces unfolding of a hitherto unidentified structural domain prior to the dissociation of VWF-A1 from GPIb-IX. Additional studies using recombinant proteins and mutant complexes confirmed the existence of this quasi-stable mechanosensitive domain (MSD) of ~60 residues in GPIb-IX and enabled localization of the MSD between the macroglycopeptide region and the transmembrane helix of GPIbα subunit. These results suggest that VWF-mediated pulling under fluid shear induces unfolding of the mechanosensitive domain in GPIb-IX, which may possibly contribute to platelet mechanosensing and/or shear resistance of VWF-platelet interaction. The identification of the mechanosensitive domain in GPIb-IX has significant implications for the pathogenesis and treatment of related blood diseases.

2.1   Introduction

The mechanical shear force generated by blood flow in the vasculature is an important factor that mediates physiological hemostasis and pathological thrombosis. The induction of platelet aggregation by the elevated shear stress requires the VWF and its association with glycoprotein (GP) Ib-IX and GPIIb/IIIa, both of which are platelet-specific receptor complexes [50, 51]. VWF in flowing blood or immobilized at the

damaged vessel wall responds to shear stress and exposes its A1-A2-A3 domains [53, 148, 149]. Concurrently, ligation of VWF under flow with the N-terminal domain of GPIbα, the major subunit in GPIb-IX, transmits a signal into platelet that eventually leads to activation of GPIIb/IIIa and aggregation of platelets [64, 150–152]. Although GPIb-IX has been recognized as the platelet mechanosensor for the past 20 years [52], how this receptor complex senses shear stress and converts this mechanical information into a protein-mediated signal that can be recognized and propagated has remained elusive.

The GPIb-IX complex consists of GPIbα, GPIbβ and GPIX subunits in a 1:2:1 stoichiometry [79, 80]. GPIbα contains, starting from the N-terminus, a leucine-rich repeat (LRR) domain that interacts with the A1 domain of VWF, a highly glycosylated macroglycopeptide region, a stalk region of about 60 residues, a pair of cysteine residues that connect to GPIbβ via disulfide bonds, a single-span transmembrane helix, and a relatively short cytoplasmic domain that is connected to the cytoskeleton through filamin A (Figure 2.4) [81]. GPIbβ and GPIX each contain an extracellular leucine-rich repeat domain that is much smaller than that of GPIbα, a transmembrane helix and a cytoplasmic tail [153]. GPIb-IX is a highly integrated complex, with each subunit interacting with one another through its transmembrane helices and membrane-proximal extracellular domains (Figure 2.4) [77]. Crystal structures of the GPIbα N-terminal domain in complex with VWF-A1 have been determined [75, 154]. Its association with VWF-A1 is classified as a catch-bond [155, 156] or flex-bond [114], which better facilitates the tethering of platelets to VWF under flow. However, numerous studies on the GPIbα N-terminal domain have not provided any evidence on how it transmits the VWF-binding signal into the platelet. This is largely because the GPIbα N-terminal domain makes no contact with the membrane-proximal parts of

GPIb-IX except through the long and relatively flexible macroglycopeptide region (Figure 2.4) [157]. There have been no reports of a highly glycosylated mucin-like region mediating a long-distance allosteric conformational change.

Related to the elusive platelet mechanosensing mechanism is another puzzling, and again unanswered, question about the function of GPIbβ and GPIX. Previous studies have demonstrated that expression of GPIb-IX in CHO cells requires all three subunits; the surface expression level of GPIbα in the absence of GPIbβ and GPIX is drastically lower than that of GPIbα in GPIb-IX [158]. In principle, this explains why mutations causing Bernard–Soulier syndrome (BSS), a rare congenital bleeding disorder characterized by an abnormally low level of expression of functional GPIb-IX, are present in all three subunits [159–161]. The phenomenon of interacting subunits necessary for co-expression has been documented in other receptor complexes such as TCR-CD3 and integrins [162–165]. In those cases, all the involved subunits take on a critical role in signaling in addition to coexpression. In comparison, no additional functions have been proposed for the extracellular domains of GPIbβ and GPIX, which can change conformation in response to environmental changes [166].

In this chapter, we aim to examine mechanical properties of the membrane-proximal mechanical sensitive domain (MSD) in GPIb-IX complex, rather than the membrane-distal Ibα ligand-binding domain as in earlier reports [114, 155]. Since individual juxtamembrane domains are not stable and are held together by the neighboring transmembrane domains [167–169], we set up the first single-molecule force measurement on the full-length GPIb-IX complex (Figure 2.4) [58, 170] using optical tweezers. Relatedly, a mammalian cell line stably expressing biotinylated GPIb-IX has been established [58]. In this system, a 13-residue BioTag sequence that is specifically recognized and biotinylated by *E. coli* biotin ligase [171] was inserted into

a desired cytoplasmic domain of GPIb-IX thereby achieving site-specific biotinylation of the complex. The biotinylated GPIb-IX was immobilized to the streptavidin bead and used for the experiment. Recombinant A1 was attached to another bead through its hexa-histidine tag and a DNA handle [53, 114, 172]. Pulling on the immobilized GPIb-IX with recombinant VWF-A1 induces unfolding of a domain in the juxtamembrane stalk region of GPIbα. This domain, hitherto unidentified and designated as the mechanosensitive domain (MSD), is structured but relatively unstable. Identification of this MSD in GPIb-IX has potential implications for the mechanism of platelet mechanosensing, in which GPIbβ and GPIX extracellular domains play a critical role.

The key points in this chapter are: (i) Pulling of VWF A1 domain that is engaged to GPIb-IX induces unfolding of a hitherto unidentified mechanosensitive domain in GPIbα. (ii) The spatial proximity of the mechanosensitive domain to GPIbβ and GPIX suggests a novel mechanism of platelet mechanosensing.

2.2 Materials and Methods

2.2.1 Materials

HEK293 Tet-on 3G cell line was obtained from Clontech (Mountain View, CA). Recombinant hexahistidine-tagged VWF-A1 and thiol-activated 802-bp DNA handles were prepared using previously established protocols [53, 114]. Antibody WM23 was kindly shared by Dr. Michael Berndt. The monoclonal anti-GPIX antibody FMC25 was purchased from Millipore (Temacula, CA). Biotinylated antibody was prepared using sulfo-NHS-biotin (Thermo Scientific, Rockford, IL).

2.2.2 Cloning of Mutant GPIb-IX Constructs

To facilitate molecular cloning, a DNA fragment that encodes the same protein sequence of human GPIbβ but lacks the GC-rich nucleotide sequence was synthesized by Genscript (Piscataway, NJ). The encoded GPIbβ included an HA tag at its N-terminus as described in Section 0 [173]. Mammalian expression plasmid pBIG-5b (Genbank accession number KM042177) was generated by inserting the coding sequence of *E. coli* biotin ligase (BirA) into multiple cloning site (MCS) II of pBI (Clontech) and a DNA cassette comprising, from 5' to 3'-ends, a 13-residue biotin acceptor peptide (BioTag)-encoding sequence [174], an internal ribosome entry site, and an enhanced green fluorescent protein (EGFP)-encoding sequence into MCS I of pBI. The new GPIbβ gene was inserted into pBIG5b as a NheI/NsiI fragment to generate pBIG5b-BirA/Ibβ/EGFP.

To construct pBIG5b-Ibα/IX-biotag/mCherry, the gene fragment encoding GPIX was amplified, appended at the 5'-end with sequences encoding the myc tag and TEV protease cleavage sequence, and inserted into pBIG5b using the NheI/XhoI restriction sites. The resulting plasmid was digested by AgeI/BsrGI to replace the EGFP gene with mCherry. Subsequently, the pBIG5b-IX-biotag/mCherry plasmid was digested by EagI/SphI to replace the BirA gene with GPIbα. To enable ligation of the GPIbα fragment, the second SphI site in the MCSII was removed prior to ligation. Mutant GPIbα genes with altered MSD were subcloned into the pBIG5b-IX-biotag/mCherry plasmid in a similar fashion.

To construct pcDNA-Ibα-biotag, the gene fragment encoding the BioTag sequence was inserted into the GPIbα cDNA to replace the sequence encoding residues Q519-A532. The mutated GPIbα gene was ligated into the pcDNA-3.1(-) vector (Invitrogen, Carlsbad, CA) using the NheI/XhoI sites. The wild-type GPIX gene was ligated into

the pcDNA vector in a similar manner. All plasmids were confirmed by DNA sequencing.
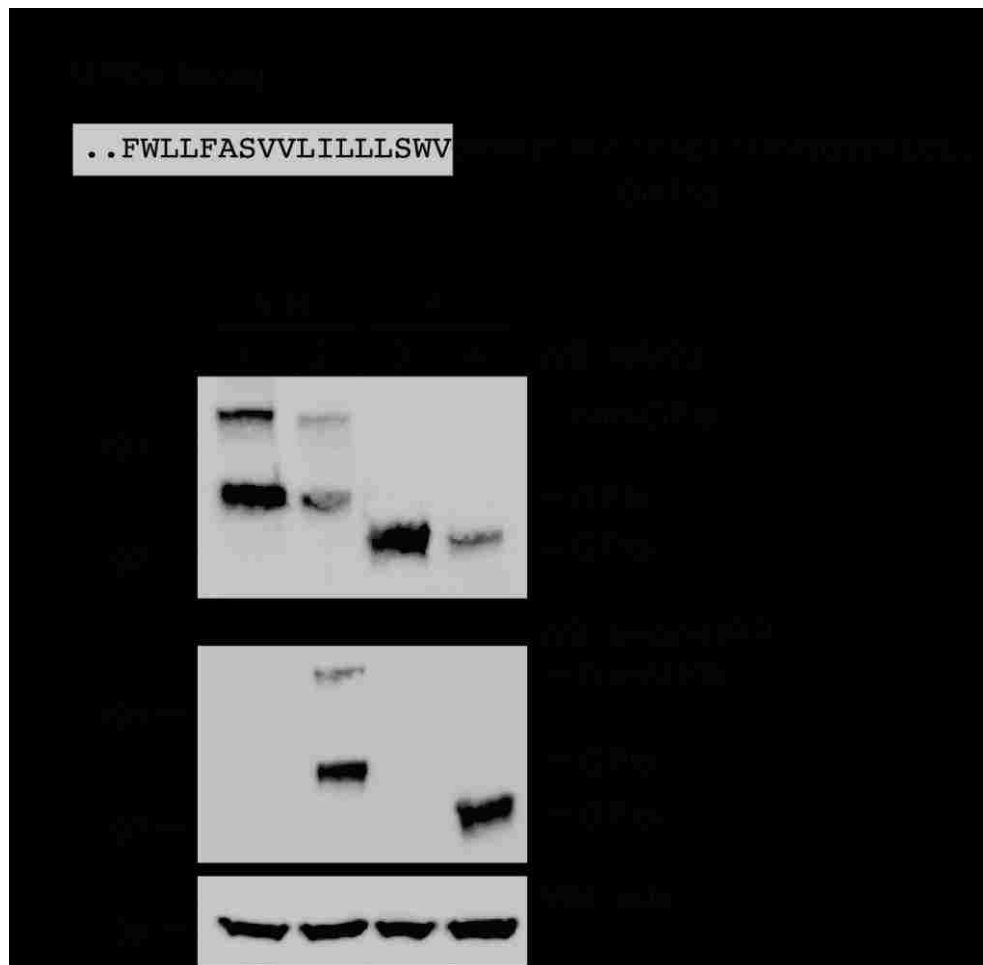
Figure 2.1 A mutant GPIb-IX in which a juxtamembrane residue in the GPIbα cytoplasmic domain was biotinylated. (A) Sequence of GPIbα-biotag, in which the cytoplasmic residues Gln519-Ala532 were replaced by the BioTag sequence (underlined). The transmembrane domain is shown in the grey box. (B) Formation of inter-subunit disulfide bonds and biotinylation of GPIbα in the GPIb-IX complex expressed in transiently transfected HEK 293 cells. Western blot experiments were performed as in Figure 2.2C–D. Lanes 1 and 3, cells expressing GPIbα/HA-GPIbβ/GPIX; lanes 2 and 4, cells expressing GPIbα-biotag/HA-GPIbβ/GPIX. Figure is kindly provided by the collaborator Dr. Renhao Li. Use with permission.

2.2.3   Expression of Biotinylated GPIb-IX and Mutants

To establish a cell line stably expressing HA-GPIbβ, HEK293 Tet-on cells were co-transfected by plasmids pBIG5b-BirA/Ibβ/EGFP and pUC19-puro using Lipofectamine 2000 (Invitrogen). The pUC19-puro plasmid was generated by ligating

the XhoI fragment of plasmid pTRE2pur (Clontech), which contains the puromycin *N*-acetyl-transferase expression cassette, into pUC19 vector that had been modified by insertion of an oligonucleotide cassette to contain a single XhoI restriction site in its MCS. Beginning 1 day post-transfection, cells were cultured in the DMEM medium supplemented with 10% fetal bovine serum (FBS), 1% penicillin/streptomycin, 5 µg/mL blasticidin and 2 µg/mL puromycin for 3 weeks. The surviving cells were treated with 3 µg/mL doxycycline for 1 day before being sorted for EGFP fluorescence and surface expression of HA-GPIbβ detected by anti-HA antibody (Sigma-Aldrich, St. Louis, MO). The cells stably expressing BirA/HA-GPIbβ/EGFP were further transfected with the pBIG5b-Ibα/IX-biotag/mCherry vector, cultured for 3 weeks and sorted for stable surface expression of GPIbα detected by WM23, and EGFP and mCherry fluorescence. Alternatively, cells stably expressing HA-GPIbβ/BirA/EGFP were transiently transfected with pcDNA-Ibα-biotag and pcDNA-IX using Lipofectamine 2000.

To induce expression of biotinylated GPIb-IX, the cells were cultured in the FBS-free medium containing 3 µg/mL doxycycline and 100 µM d-biotin for 1 day. The cells were harvested and lysed in the lysis buffer (1% triton X-100, 5 mM $CaCl_2$, 58 mM sodium borate, 10% protease inhibitor cocktail, 5 mM N-ethylmaleimide, pH 8.0; at approximately $1–2\times10^4$ cells/µL). The supernatant containing biotinylated GPIb-IX was further analyzed by Western blot and flow cytometry largely as described previously [166, 175, 176], or stored at −80 ˚C for the single-molecule force measurement.
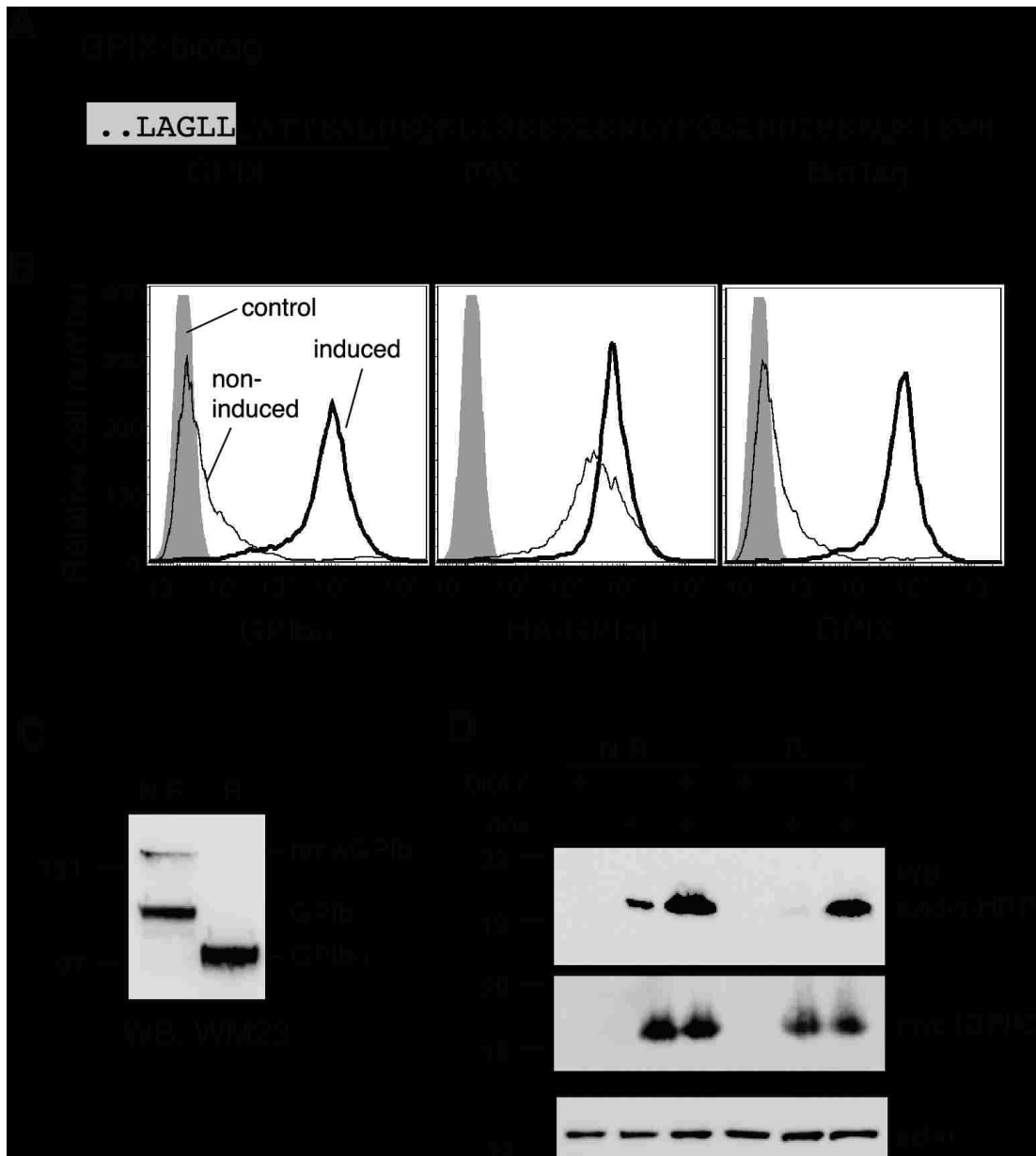
Figure 2.2 Expression and biotinylation of GPIb-IX. (A) The altered GPIX cytoplasmic sequence that contains the engineered biotinylation site. Residues in the GPIX transmembrane domain are shown in a grey box, and added residues are underlined and labeled. (B) Overlaid flow cytometry histograms showing the surface expression of GPIbα, HA-tagged GPIbβ and GPIX-biotag in stably transfected HEK293 Tet-on cells. Prior to (thin traces) and after (thick traces) the induction of protein expression by the addition of doxycycline and biotin, the cells were stained by mouse IgG (control), anti-GPIbα antibody WM23, anti-HA antibody, or anti-GPIX antibody FMC25 and detected by flow cytometry. (C) Formation of native inter-subunit disulfide bonds in the GPIbα/HA-GPIbβ/GPIX-biotag complex detected by Western blot. The cell lysate was resolved in an SDS gel under non-reducing (N.R.) or reducing (R.) conditions and transferred to the polyvinylidene difluoride (PVDF) membrane. The membrane was probed with WM23 followed by HRP-conjugated secondary antibody. The positions of molecular weight markers in the gel are marked on the left. (D) Expression of biotinylated GPIX-biotag in the cell detected by Western blot. Doxycycline (dox) and biotin were added, in combination as indicated, to the cells to induce protein expression

and biotinylation. The cell lysates were resolved in SDS gels and transferred to the PVDF membrane. The membranes were probed separately with (top) HRP-conjugated avidin, or (middle) anti-myc antibody and (bottom) anti-actin antibody followed by HRP-conjugated secondary antibody. Figure is kindly provided by the collaborator Dr. Renhao Li. Use with permission.

2.2.4 Expression and Purification of Recombinant GPIbα Stalk Region (Ibα-S)

The DNA fragment encoding GPIbα residues Ala417-Phe483 was amplified from the GPIbα cDNA and later ligated into the pHex vector [80] as a BamHI/XhoI fragment. The DNA sequence was confirmed by sequencing. Ibα-S was expressed as a decahistidine-tagged glutathione S-transferase (GST) fusion protein from *E. coli* BL21 cells and its purification by nickel affinity chromatography followed published protocols [80, 168]. After the fusion protein was cleaved by thrombin (5 units per mg of fusion protein), Ibα-S was separated from GST by preparative reverse-phase HPLC and stored at −80 ˚C as lyophilized powder [80]. Related proteins Ibα-cSc and Ibα-cS-biotag were prepared in a similar manner. The purity of each protein was confirmed by SDS-PAGE and analytical HPLC, and its concentration was estimated using the dry weight method.
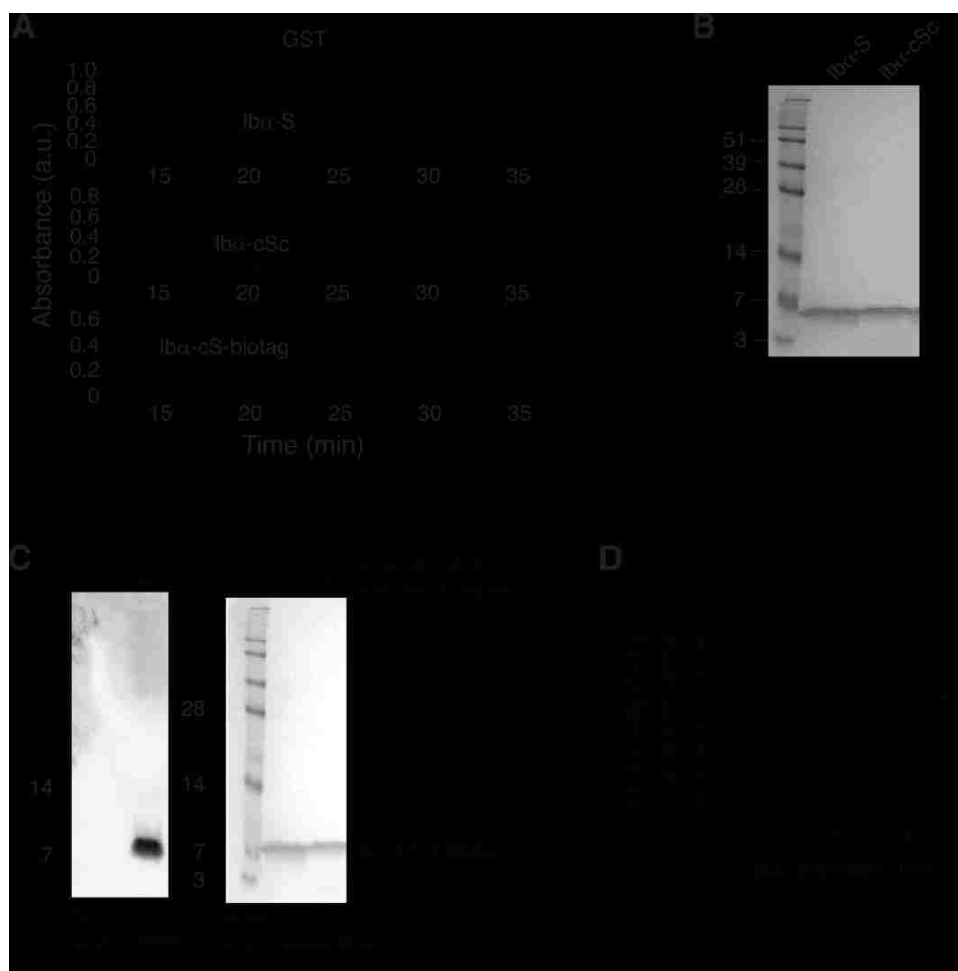
Figure 2.3 Expression and purification of the recombinant mechanosensory domains. (A) Preparative HPLC traces showing the separation of recombinant mechanosensory domains (Ibα-S and Ibα-cSc) from GST after thrombin digestion. The digestion mix was dissolved in 35% acetonitrile, 0.1% TFA. 10 mM DTT was added to the mixture containing Ibα-cSc or Ibα-cS-biotag. Both samples were filtered with 0.2-µm Nylon filter and injected to a Vydac reverse-phase C4 column followed by a gradient elution. Absorbance at both 220 nm (solid trace) and 280 nm (dashed) was recorded against time. The peaks of proteins of interest were marked. (B) Purified Ibα-S and Ibα-cSc were collected from HPLC, lyophilized and resolved in a 15% Bis-Tris SDS gel. The gel was stained by Coomassie blue. (C) Purified Ibα-cS-biotag (unbiotinylated or biotinylated, depending on its coexpression with biotin ligase) was resolved in 15% Bis-Tris SDS gel, and blotted by HRP-conjugated avidin (left) or stained directly with Coomassie blue (right). (D) Overlaid CD spectra of unbiotinylated Ibα-cS-biotag (dashed trace), biotinylated Ibα-cS-biotag (dotted trace) and Ibα-S (solid trace). Figure is kindly provided by the collaborator Dr. Renhao Li. Use with permission.

2.2.5   Laser Optical Tweezers Measurement

Biotin and digoxigenin (Dig) DNA handles were prepared as described previously

[53, 114]. Dithiobis-nitrilotriacetic acid (NTA) (Dojindo, Rockville, MA) was first

reduced by Immobilized TCEP Disulfide Reducing Gel (Thermo Scientific), and then coupled to the activated biotin DNA handle via a disulfide bond. Recombinant Ibα-cSc was coupled to two pieces of DNA handle through the disulfide bonds as described previously [53, 114]. Carboxyl-polystyrene beads of 2.0-μm diameter (Spherotech, Lake Forest, IL) were covalently coupled with streptavidin (Invitrogen), anti-digoxigenin Fab (Roche), or WM23 as described previously [53, 114]. To couple VWF-A1 to the bead, streptavidin-coated beads were first incubated for 10 min with 1 nM biotin-DNA handle-NTA in TBS buffer (150 mM NaCl, 10 mM Tris·HCl, 5 mM NiCl$_2$, pH 7.5) and then washed and incubated with 100 pM VWF-A1 for 15 min before experiment. In order to capture the biotinylated GPIb-IX, streptavidin-coated beads were incubated with 20 μL GPIb-IX-containing cell lysate for 10 min and washed with TBS buffer containing 1% triton X-100. Single-molecule pulling experiments were performed using an analytical mini-optical tweezers apparatus that has been used in several single-molecule unfolding/unbinding studies [17, 177, 178]. Force and bead-to-bead distance were recorded at 200 Hz. When appropriate, the force-extension data was fitted to the WLC model. The lifetime of the bond as a function of force was estimated by the Dudko–Hummer–Szabo equation (Eq. (1.37) or Eq. (1.38)) [34].

2.2.6   Circular Dichroism Spectroscopy

Purified Ibα-S or its variants were weighed and dissolved in 50 mM Tris·HCl, 50 mM NaCl, 1 mM DTT, pH 7.4 buffer, or the same buffer containing various concentrations of urea, to a final concentration of 2.5 mg/mL. Far-UV circular dichroism (CD) spectra (190–260 nm) were collected on a JASCO J810 spectrometer using a 0.1-cm quartz cuvette at 20 ˚C. The step-wise wavelength was set to 0.5 nm/step. Each spectrum was scanned 5 times and corrected for background signal.

2.3   Results

2.3.1   Force-Induced Unfolding of a Domain in the Full-Length GPIb-IX

To enable single-molecule force measurement of full-length GPIb-IX, a new expression system was engineered to achieve site-specific biotinylation of GPIb-IX (Figure 2.2). Since the cytoplasmic domain of GPIX is not critical to the proper assembly of GPIb-IX [176], a 13-residue BioTag sequence in which a lysine residue is specifically recognized and biotinylated by *E. coli* biotin ligase [174] was appended to the C-terminus of GPIX (Figure 2.2, Figure 2.4, and Figure 2.7). Coexpression of the engineered GPIX (GPIX-biotag) with GPIbα, HA-tagged GPIbβ [173], and biotin ligase in human embryonic kidney (HEK)293 cells produced a well-assembled GPIb-IX complex that was uniformly biotinylated at the cytoplasmic end of GPIX (Figure 2.2). In our optical tweezers assembly (Figure 2.4), recombinant hexahistidine-tagged VWF-A1 was attached to an NTA-conjugated DNA handle. The other end of the DNA handle was immobilized to a 2-μm polystyrene bead via biotin-streptavidin linkage, which was controlled by the optical trap [53]. The biotinylated GPIb-IX was captured by another streptavidin bead. This bead was held by a fixed micropipette. It should be noted that a small portion of GPIbα and GPIbβ in transfected cells form hmwGPIb complexes [166, 176], in addition to the wild-type GPIb-IX (Figure 2.2C). Since hmwGPIb is formed in the absence of GPIX [176], specific biotinylation of the GPIX cytoplasmic domain ensured that only the native full-length GPIb-IX was immobilized to the fixed bead and analyzed here.
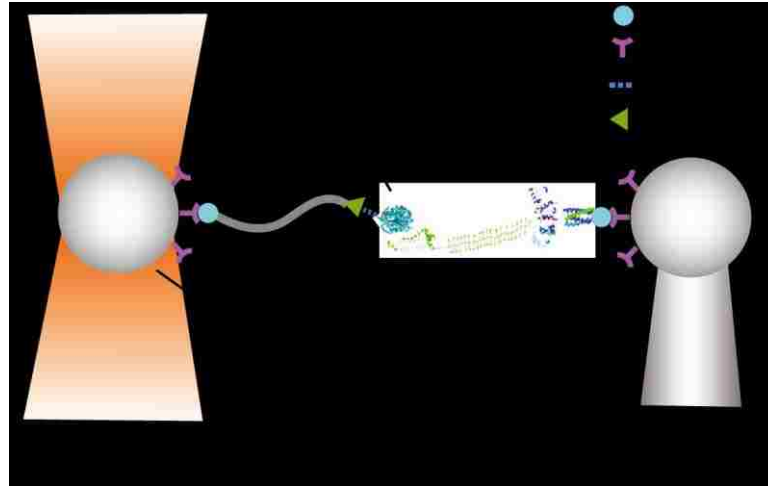
Figure 2.4 Experimental setup for the optical tweezers single-molecule force measurement of the full-length GPIb-IX. The BioTag sequence, that is specifically recognized and biotinylated by *E. coli* biotin ligase, was either appended to the C-terminus of GPIX cytoplasmic domain (as shown) or placed into the juxtamembrane region of the GPIbα cytoplasmic domain. The biotinylated GPIb-IX was expressed in transfected cells, solubilized in the Triton X-100-containing lysis buffer, and eventually immobilized on the streptavidin-coated bead. Recombinant VWF-A1 was linked through a DNA handle to a polystyrene bead that was placed in an optical trap as described before [53]. The right bead was held by a fixed micropipette, while the left bead was controlled to move by the optical trap.

In each recorded approach-retract cycle, the trapped VWF-A1 bead was brought into contact with the fixed GPIb-IX bead for approximately 1 second at a low contact force (~5 pN), and then pulled away. While no or very little (<1 pN) adhesion force was observed in ~80% of the approach-retract cycles, a tether that extended to over 200 nm and ruptured at around 10–30 pN was consistently observed in the other 20% of cycles (Figure 2.5A). The force-extension relationship of the tether fitted well with the WLC Model [32] in the low force (0–10 pN) regime (Figure 2.5A). It is noteworthy that the rupture force of 10–30 pN observed during the retraction step of pulling VWF-A1 from GPIb-IX was significantly smaller than those observed in the control experiment stretching DNA handle-NTA from VWF-A1 (Figure 2.8A), but comparable to those reported for the unbinding of VWF-A1 and the GPIbα N-terminal domain (Figure 2.6) [114, 156]. Thus, in our optical tweezers experiment we have observed the

binding and unbinding of VWF-A1 and full-length GPIb-IX at the single-molecule level.
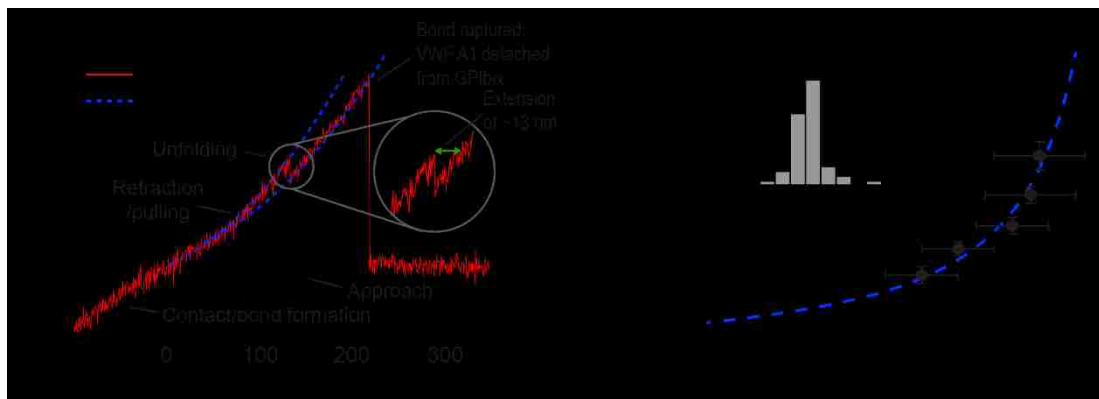
Figure 2.5 Unfolding of a domain by pulling VWF-A1 from biotinylated GPIb-IX. (A) A single-molecule force-distance trace illustrating the unfolding of MSD before the detachment of VWF-A1 from GPIb-IX. The inset highlights the observed unfolding event. (B) Fit of unfolding force vs. extension data to the WLC model (blue dashed line), which yielded a contour length of 25.1 ± 0.3 nm. Extension distances were sorted by unfolding force into 4-pN bins. A histogram of extension (inset) was used to find peak extension. Unfolding forces were averaged for each bin (*n* per bin is 23–51). Error bars are one *SD* for force and the half bin width for extension.

In the pulling curves of VWF-A1/GPIb-IX, an extension or unfolding event prior to the rupture, with forces ranging from 5 to 20 pN, was observed (Figure 2.5A). The WLC fit of the unfolding force and extension yielded a contour length of 25.1 ± 0.3 nm (Figure 2.5B), and a persistence length of 0.74 ± 0.04 nm. Assuming a contour length of 4 Å per residue, it indicated that a structural domain of approximately 63 residues was stretched or unfolded by the pulling force while VWF-A1 was still bound to the GPIbα N-terminal domain. Intact domain structures are required for the interaction of VWF-A1 with the GPIbα N-terminal domain, both of which contain hundreds of residues [154]. Furthermore, similar unfolding events were not observed in either the control experiment in which the NTA-DNA handle was pulled from VWF-A1 (Figure 2.8A) or previous force measurements employing VWF fragments and the GPIbα N-terminal domain [114, 155, 156]. Therefore, the observed unfolding events in the pulling of VWF-A1 from GPIb-IX are not due to unfolding of either of the interacting

domains, but rather of a different domain in the GPIb-IX complex, which we designate here as the mechanosensitive domain (MSD).

2.3.2   Lifetime of GPIb-IX/VWF-A1 Bonds under Force

To quantify the pulling of VWF-A1 from biotinylated GPIb-IX, we obtained the bonds lifetime of VWF-A1/GPIb-IX by transforming the force histogram according to Dudko–Hummer–Szabo equation (Eq. (1.38)) [34]. The bin width is 5 pN, and the force is the mean force in each bin ($n > 3$), and the errors are the *SEM*s. The plot of lifetimes of GPIb-IX/VWF-A1 bond versus force is shown in Figure 2.6. As the external pulling force increases, the bond lifetimes become smaller. This plot can be further used as a control to demonstrate that we are indeed quantifying the GPIb-IX/VWF-A1 bond(s), when compared with results of pulling VWF-A1 from GPIb-IX complex captured by a WM23 coated bead.
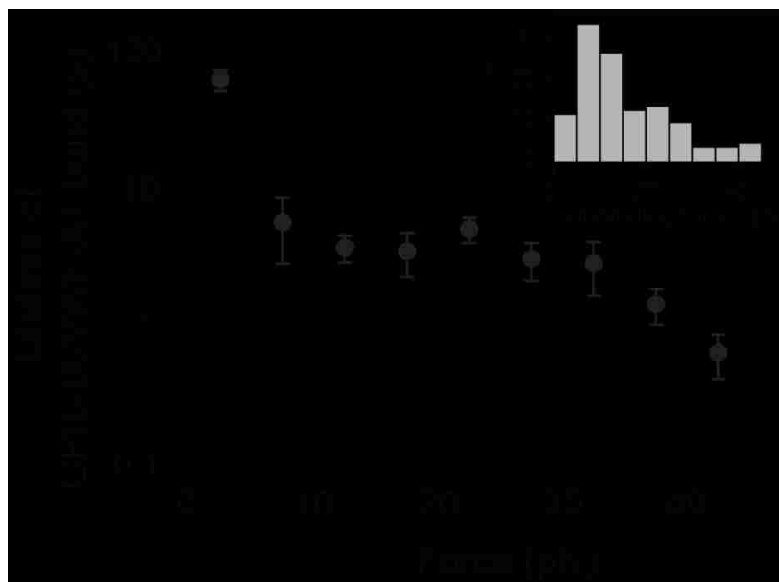
Figure 2.6 Lifetimes of the GPIb-IX/VWF-A1 bond versus force. The bonds lifetime of VWF-A1/GPIb-IX was obtained by transforming the force histogram according to Dudko–Hummer–Szabo equation (Eq. (1.38)). The bin width is 5 pN, and the force is the mean force in each bin ($n > 3$), and the errors are the *SEM*s. The inset is a representative histogram of unbinding force (collected under a pulling speed of 100 nm/s) used to obtain bond lifetimes [34].

2.3.3 Localization of MSD to the Stalk Region of GPIbα
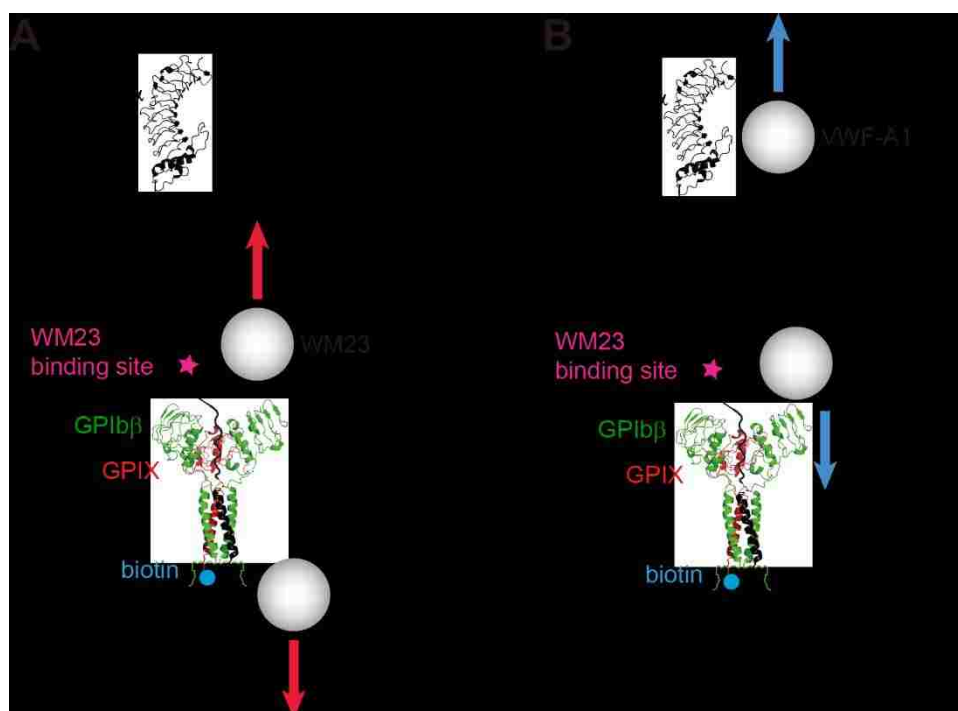
Figure 2.7 Pulling GPIb-IX complex in two other directions. (A) Pulling of DNA handle-conjugated WM23 on the GPIbα-biotinylated GPIb-IX complex. (B) Pulling of VWF-A1 from GPIb-IX captured on the WM23 bead.

In order to localize the MSD, we biotinylated and attached the monoclonal antibody WM23, which recognizes an epitope in the C-terminal portion of the macroglycopeptide region (Figure 1.5) [179], to a fixed bead. We did not observe any unfolding events when pulling VWF-A1 from GPIb-IX captured on the WM23 bead, while the lifetimes of the GPIb-IX/VWF-A1 bond remained unchanged (Figure 2.8). Moreover, a mutant GPIb-IX, in which a juxtamembrane residue in the GPIbα cytoplasmic domain was biotinylated, was expressed in HEK293 cells (Figure 2.1A–B). Pulling of DNA handle-conjugated WM23 on this GPIbα-biotinylated GPIb-IX produced similar unfolding events prior to the rupture (Figure 2.8A). Therefore, MSD should be located between the WM23 epitope in the macroglycopeptide region and the cytoplasmic domain of GPIbα. In other words, it should be in the stalk region or transmembrane helix of GPIbα. The force required to unfold a transmembrane helix is

much stronger (>100 pN) [180, 181] than what was observed here (~10 pN). Additionally, unfolding of the 25-residue transmembrane helix of GPIbα would have produced an unfolding contour length of ~10 nm, much shorter than >20 nm observed in the force curves (Figure 2.5). Our results, therefore, suggest that the juxtamembrane stalk region of GPIbα contains MSD.
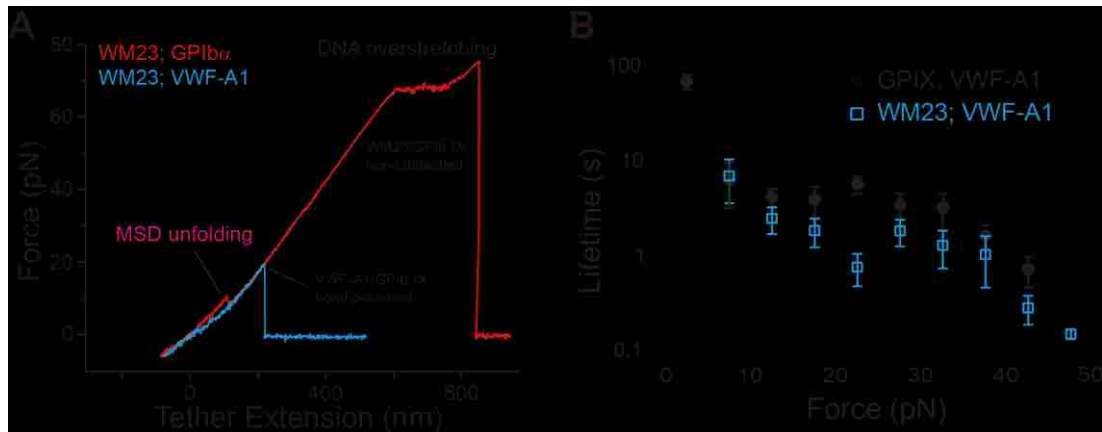
Figure 2.8 Localization of MSD in the juxtamembrane stalk region of GPIbα. (A) Overlaid force-distance traces of pulling VWF-A1 on GPIb-IX captured by biotinylated WM23 (red trace) and on GPIb-IX captured by biotin at the GPIX cytoplasmic domain (grey). (B) Plots of lifetimes of the GPIb-IX/VWF-A1 bond versus force (mean ± *SEM*, *n* > 3).

2.3.4 Force-Induced Unfolding/Refolding of the Recombinant Stalk Region of GPIbα (Ibα-cSc)

The stalk region of GPIbα has not been studied before, although it has been noted for its higher hydrophobic content than the neighboring macroglycopeptide region [182]. A recombinant protein Ibα-S that contains the GPIbα stalk region (residues Ala417-Phe483) was produced (Figure 2.3). De-convolution of its CD spectrum [183] indicated that Ibα-S is a structured domain, with 24% of its residues taking α-helical conformation, 19% in β-strand, and the rest in coils. Ibα-S is relatively unstable, as it was denatured in less than 1 M urea. Consistently, appending a biotinylated BioTag sequence to its C-terminus significantly altered its structure or stability (Figure 2.3). In

comparison, a related protein called Ibα-cSc, in which the GPIbα stalk region was flanked by a cysteine on each side, displayed a similar CD spectrum as Ibα-S but was more stable as judged by urea denaturation.

Optical tweezers measurement was performed on Ibα-cSc. Each of the flanking cysteine residues in Ibα-cSc was linked to a piece of DNA handle and a bead (Figure 2.9).
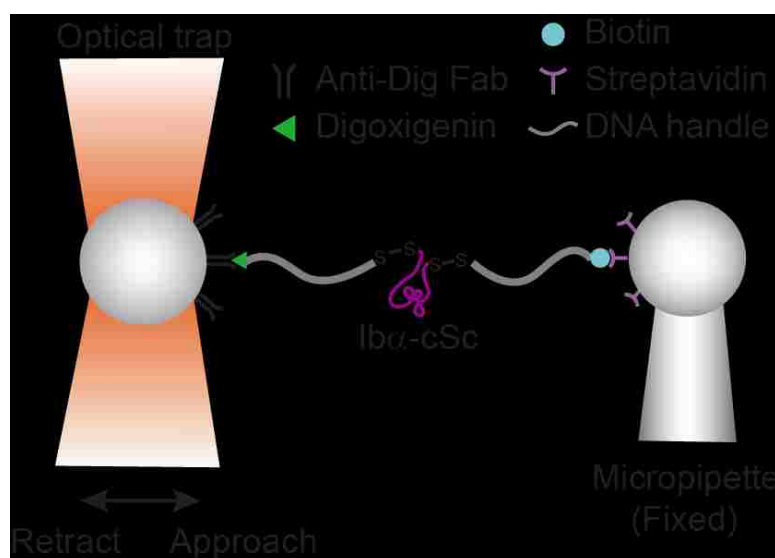
Figure 2.9 The optical tweezers setup to measure force-induced unfolding of Ibα-cSc. The recombinant Ibα-cSc was coupled with two DNA handles to each of its two terminus. One SA bead captured the biotinylated Ibα-cSc handle, and immobilized it there. The other bead coated with anti- digoxigenin Fab (abbreviated as "anti-dig bead") was captured and controlled by the optical trap. At each approach-retract cycle, the anti-dig bead was brought into contact with the fixed SA bead, and was held for a dwell time to allow the reaction.

Upon pulling, Ibα-cSc unfolded at 5–20 pN and was stretched to 10–15 nm (Figure 2.10A–B), which is comparable to the unfolding force and extension observed in the full-length GPIb-IX. WLC fit of the unfolding force as a function of extension yielded a contour length of 22.3 ± 1.2 nm and a persistence length of 0.64 ± 0.10 nm. The shortening/contraction events during refolding also fell on the same curve (Figure 2.10B).
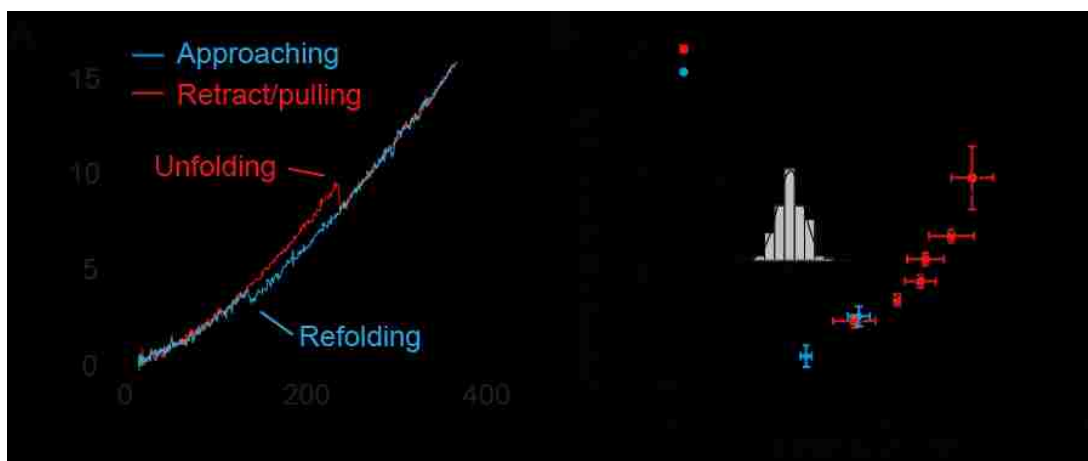
Figure 2.10 Force-induced unfolding and refolding of Ibα-cSc from pulling experiments. (A) Force-distance traces showing the force-induced unfolding and refolding of Ibα-cSc from pulling at 100 nm/s. (B) Unfolding force-extension data of pulling Ibα-cSc (red squares) fitted to WLC model, yielding a contour length of 22.3 ± 1.2 nm. Extension distances were sorted by unfolding force into 2-pN bins. A histogram of extension of each bin (inset) was fitted to a Gaussian curve (inset, solid line) to find peak extension. Unfolding forces were averaged for each bin (*n* per bin is 43–149 for unfolding, and 40–64 for refolding). Error bars are one *SD* for force and the half width of the Gaussian fit for extension. Blue circles represent refolding force-shortening data, which was treated in the same way as the unfolding forces-extension.

To characterize the free-energy landscape, we fit the most probable unfolding force as a function of loading rate to the single-barrier Bell–Evans model (shown in Figure 2.11), which yielded an unfolding rate in the absence of force of 0.008 s^{-1}, and a barrier width of 2.6 nm [33].

Since Ibα-cSc contains 67 residues between the two cysteine residues, when fully stretched it should extend to 26.8 nm, assuming a contour length of 4 Å per residue. Thus, our measurement indicated that the end-to-end distance of folded Ibα-cSc is about 4.5 nm. Overall, these results demonstrated that the GPIbα stalk residues form a structured MSD that has a similar unfolding force and extension to that observed in GPIb-IX.
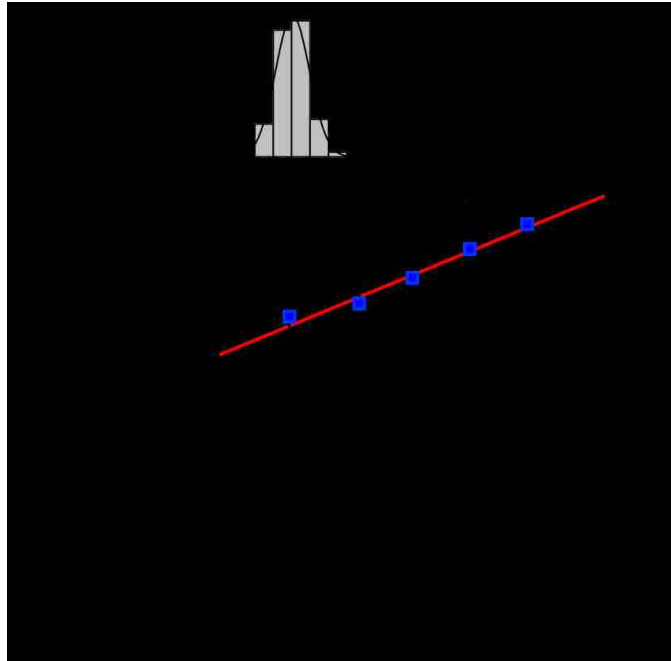
Figure 2.11 Most probable unfolding force of Ibα-cSc as a function of loading rate. Unfolding forces at five different loading rates were plotted as histograms (inset). Each histogram was fitted to a Gaussian curve (inset, solid line) to obtain the most probable force. Uncertainty in force (the black error bar) is shown as half of the bin width. The solid red line is a linear fit of the data to the Bell–Evans model [33].

2.3.5   Lack of Unfolding in GPIb-IX that Lacks MSD of GPIbα

To confirm the location of MSD in GPIb-IX, GPIbα mutants that lack the entire MSD (GPIbαΔS), the N-terminal (GPIbαΔS$_N$), and C-terminal half (GPIbαΔS$_C$) of the domain were constructed (Figure 2.12). Considering the relative instability of MSD, we reasoned that deletion of either half of the domain should effectively leave the remaining sequence unfolded. Each GPIbα mutant was coexpressed with HA-GPIbβ and GPIX-biotag to produce the corresponding mutant GPIb-IX complex in the transfected HEK293 cells. Western blot analysis revealed the defective complex assembly by GPIbαΔS, as it was present mostly in the hmwGPIb complex [166, 176] instead of the native GPIb complex (Figure 2.12B).
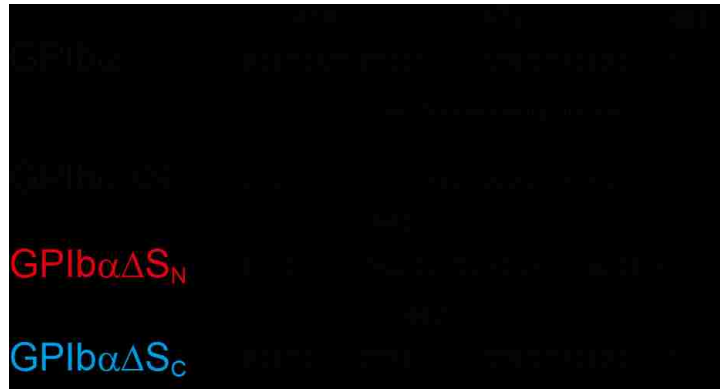
Figure 2.12 Expression and assembly of the GPIbα mutant complexes. Sequences illustrating various deletion mutations in MSD.

In comparison, both GPIbαΔS$_N$ and GPIbαΔS$_C$ formed native GPIb, and therefore were analyzed further by optical tweezers. VWF-A1 was used in the pulling experiments on mutant GPIb-IX complexes containing either GPIbαΔS$_N$ or GPIbαΔS$_C$, yielding similar bond lifetimes as those observed for the wild-type GPIb-IX (Figure 2.13A). In contrast to the wild-type, no unfolding events were observed in the pulling of either mutant complex (Figure 2.13B). Overall, these results demonstrated that disrupting the structure in the GPIbα stalk region eliminates the force-induced unfolding event in GPIb-IX, thus confirming the presence of MSD in this region.
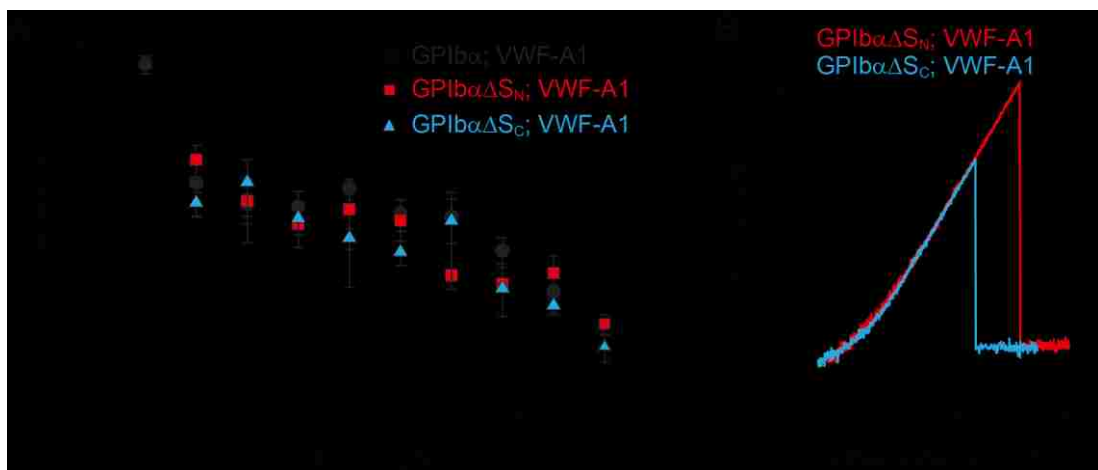
Figure 2.13 Lack of force-induced unfolding in GPIb-IX complexes with altered MSD. (A) Lifetimes (mean ± *SEM* of >3 experiments) of the bonds between VWF-A1 and the three constructs as a function of force. Each plot is identified by the identity of GPIbα subunit in the complex and the pulling ligand. (B) Representative force-distance traces of pulling VWF-A1 on GPIbαΔS$_N$/GPIbβ/GPIX (red trace) or GPIbαΔS$_C$/GPIbβ/GPIX (blue trace) complex that was captured by biotin at the GPIX cytoplasmic, showing the lack of force-induced unfolding.

2.4 Discussion and Conclusion

In this chapter, we present the first evidence for a juxtamembrane MSD in the GPIb-IX complex. VWF-A1-mediated mechanical pulling on the N-terminal domain of GPIbα induced unfolding of a MSD in GPIb-IX (Figure 2.4, Figure 2.5 and Figure 2.6). Follow-up studies utilizing different pulling ligands and immobilization sites localized MSD to the stalk region of GPIbα (Figure 2.7 and Figure 2.8). Direct characterization of the recombinant stalk region revealed that it contains a structured but relatively unstable domain and that its sensitivity to tensile force is similar to that of the full-length complex (Figure 2.9 and Figure 2.10). Finally, disrupting the domain structure by deleting a significant portion of the domain eliminated the VWF-A1-induced unfolding event in GPIb-IX (Figure 2.13), confirming the location of MSD in the juxtamembrane stalk region of GPIbα. Prior to this study, there have been no reports about the existence of a structured domain in the stalk region of GPIbα. Little information is currently available about this MSD. The CD spectrum of Ibα-S indicates the presence of some secondary structure, but it is likely that the conformation of MSD in GPIb-IX may be somewhat different from that in recombinant Ibα-S, considering that MSD is relatively unstable and sensitive to its surroundings.

Numerous studies have been carried out to characterize the interaction of VWF or its A1 domain with the N-terminal domain of GPIbα, such as the complex structure, the binding kinetics, and the influence of force [74, 75, 114, 154–156, 184]. In comparison, only a few biophysical studies have focused on the purified GPIb-IX [157, 185], primarily due to the difficulty in obtaining this hetero-tetrameric membrane protein complex. A previous study has used the optical tweezers to measure the unbinding forces between VWF-coated beads and GPIb-IX-expressing Chinese hamster ovary cells [186], but it was not conducted under single-molecule experimental conditions

and did not report the unfolding event. Here, site-specific biotinylation of the cytoplasmic domain enabled a systematic dissection of GPIb-IX under a condition that simulated the effect of shear flow on the VWF/GPIb-IX pair. Only through the single-molecule force measurement on the full-length receptor complex was the MSD in GPIb-IX uncovered. This novel setup will be useful in future investigation of GPIb-IX structure-function and could be applied to other mechanosensing receptors. Moreover, we found that the MSD unfolds at forces ranging from 5 to 20 pN, which is similar to the level of forces reported to induce catch- or flex-bond formation in the complex of VWF-A1 with the N-terminal domain of GPIbα [114, 155, 156]. The unfolding and extension of the MSD could lower the force applied to the VWF/GPIb-IX complex and, therefore, may function together with the VWF-A1/GPIbα interaction to stabilize the tethering and adhesion of platelets to VWF under flow.

The identification of a juxtamembrane MSD in GPIb-IX has potential implications for the mechanism of platelet mechanosensing. We proposed a model of GPIb-IX mechanosensing (naming it "the trigger model"). In this model, the force-induced unfolding of MSD is the step in which GPIb-IX converts a mechanical signal into a change in protein conformation (Figure 2.14). This type of signal can be recognized and transduced further. Under the assumption that platelets behave as spherical beads with a radius of 1 μm, it can be estimated that at 20 dynes/cm^2, a typical shear stress found in the microvasculature, the drag force exerted on a single platelet is 64 pN [187, 188]. Since it takes only 5–20 pN to unfold MSD in GPIb-IX, it is plausible that VWF, under physiological or pathological shear stress, could exert sufficient force on the tethered GPIb-IX, and the platelet, to induce the unfolding of MSD therein. Moreover, the long and unstructured macroglycopeptide region of GPIbα contains 1–4 copies of tandem nucleotide repeat sequence (VNTR), and the VNTR polymorphism contributes

to the variation in the molecular weight and length of GPIbα (by as much as 15 nm) [189]. The number of VNTR repeat is not correlated with the occurrence of coronary heart disease, in which arterial thrombosis and the interaction of VWF/GPIb-IX is thought to play an important role [190]. This lack of correlation has not been explained in the previously proposed receptor clustering model of GPIb-IX [191], as one would expect that the VNTR polymorphism, with its significant impact on GPIbα length, should affect the extent of GPIbα clustering on the platelet surface and downstream signaling. By comparison, in our model of mechano-transduction the macro-glycopeptide region is proposed to transduce only the tensile force, which should be minimally affected by its length and is therefore consistent with the lack of correlation between VNTR polymorphism and occurrence of coronary heart disease. Finally, MSD is located in direct contact with the extracellular domains of GPIbβ and GPIX (Figure 1.5), which can change conformation in response to an alteration in inter-subunit contacts [153, 166]. Therefore, we propose that unfolding of MSD induces a conformational change in the neighboring GPIbβ and GPIX, which transmits a signal into the cell (Figure 2.14). This mechano-transducing model, instead of the receptor clustering model, can explain that anti-GPIbβ monoclonal antibody RAM.1 blocks VWF-initiated GPIb-IX-mediated signaling into the platelet without affecting VWF binding to GPIb-IX [185, 192]. It may also help to explain the critical role of GPIbβ in mediating the procoagulant activity of platelets [193].

The identification of MSD in GPIb-IX also provides new insights on the pathogenesis of BSS. GPIbα is quickly degraded in transfected cells when it is not expressed with GPIbβ and GPIX [194]. However, the underlying molecular basis for this degradation has remained unclear. It is found that Ibα-S in isolation is not stable (Figure 2.3). It is therefore conceivable that the instability of MSD in GPIbα could

contribute to the rapid degradation of GPIbα when it is expressed in the absence of GPIbβ and GPIX [194]. GPIbβ and GPIX, being close to MSD in the complex, may either stabilize the domain or prevent its induction of degradation. Furthermore, the potential involvement of GPIbβ and GPIX in detecting unfolding of MSD and further propagating the signal offers a plausible functional justification for their elaborative complexation with GPIbα.
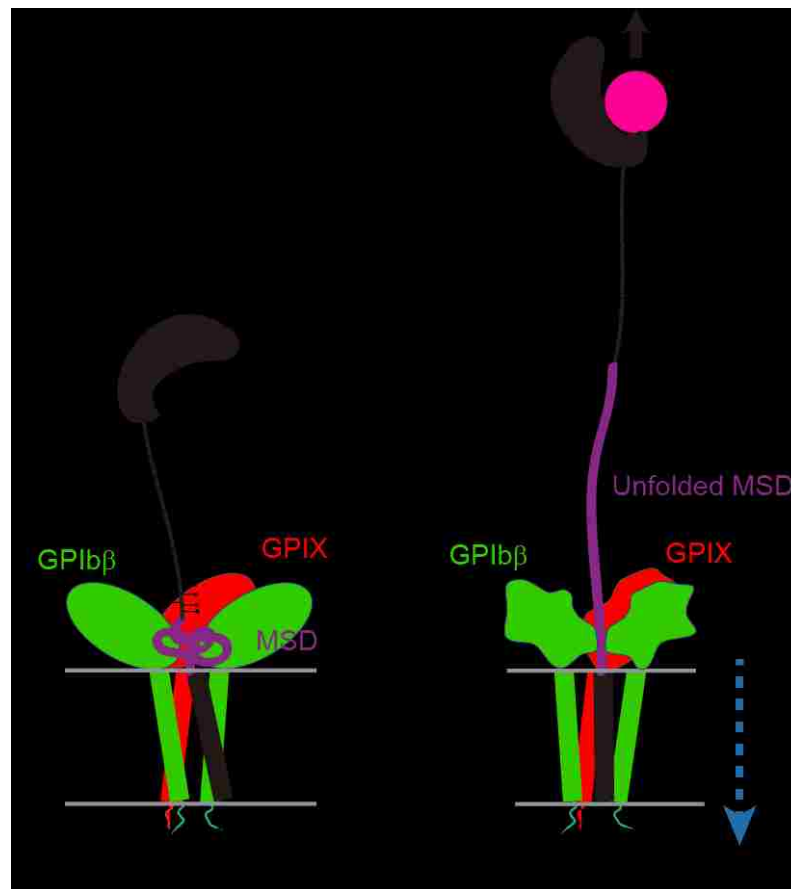
Figure 2.14 The trigger model of the proposed mechanosensing mechanism of GPIb-IX. We found in this study that the juxtamembrane MSD in GPIbα is folded, and it unfolds upon VWF-mediated pulling. Our results suggest that on the cell surface the juxtamembrane MSD in GPIbα is folded in the absence of shear flow (left panel). VWF binding under shear to the N-terminal domain of GPIbα induces unfolding of MSD, and subsequently a conformational change in the adjacent extracellular domains of GPIbβ and GPIX, which sends a signal across the platelet membrane (right).

2.5   Authorship and Conflict-of-Interest Statements

This project has been published as: Zhang, W., Deng, W., Zhou, L., Xu, Y., Yang, W., Liang, X., *et al.* (2015). Identification of a juxtamembrane mechanosensitive domain in the platelet mechanosensor glycoprotein Ib-IX complex. *Blood, 125*(3), 562-569.

Chapter 3: Development of a Novel Protein Coupling Method for Single Molecular Experiments Using Optical Tweezers

3.1 Introduction

The most single-molecule techniques, including atomic force microscopy (AFM), optical tweezers, magnetic tweezers, allow for the direct measurement of individual molecular properties. These instruments have a high sensitivity and precision in order to manipulate or visualize individual molecules, and measure microscopic forces.

Depending on the purpose of single-molecule experiments, different systems are set up. To measure the mechanical and biological properties of proteins, or protein–protein interactions, researchers usually need to create a linkage system with the protein on the chain of linkage, and then apply an external force to stretch it using AFM or optical tweezers. In these linkage systems, the protein needs to be immobilized at one end, and captured on the other end, through some kinds of bindings to beads or substrates. A DNA handle is often used in these systems to make the chain softer and longer for better measurements. Therefore, there are several connecting points on the single chain, which endure the same stretching force as the protein does. These connecting points should not break before the conformational change or protein–protein dissociation happens. The most widely used techniques involved here are protein tags and disulfide bonds. Their features are summarized in Table 3.1.

The methods of tagging the desired protein with peptides (such as His_6, myc, HA, and FLAG) or biotin have been widely used by researchers for protein detection, purification, and immobilization in single-molecule experiments [102–105]. It is known that the affinity between polyhistidine-tag (usually 6×His-tag) and Ni-NTA is

relatively weak and non-covalent, meaning that the binding has low mechanical strength and thermodynamic stability, and the reaction is reversible. Furthermore, due to the non-specificity of the bonds, the single-molecule experiments usually cannot eliminate non-specific interaction between the protein and the polystyrene bead in a single-molecule system. The disulfide bonds are strong, but this method needs protein reduction step, which also has an effect on proteins' internal disulfide bonds, and further changes their native structures and properties. However, in single-molecule force experiments, statistical analysis of events, e.g. unfolding/refolding and rupture, are necessary for drawing convincible conclusions. It requires the linkage system to be stable, and it would best that one can repeatedly pull the same tether for many times. It has been difficult to achieve a mechanically stable system for single-molecule pulling experiments using these traditional methods.

Table 3.1 Comparison of different linking methods in single-molecule systems

Linkages	Mechanical Stability
Disulfide Bonds	Strong, needs reduction before coupling
Polyhistidine-tag–Ni-NTA	Weak
Biotin–Avidin/Streptavidin	Strong, needs biotinylation
Antibody–Antigen	Intermediate

Recently, Mark Howarth *et al.* [36] proposed a new tagging method through the formation of a rapid covalent bond without using chemical modification, artificial amino acids, or cysteines. They obtained a peptide tag of 13 amino acids (termed SpyTag) by splitting the *Streptococcus pyogenes* (*S. pyogenes*) CnaB2 domain. SpyTag is capable of forming a covalent bond with its partner SpyCatcher, a rational modification of the rest protein fragments from the splitting of CnaB2, as shown in Figure 1.8. This reaction proceeds spontaneously, rapidly, efficiently throughout diverse conditions of buffer, pH, and temperature. Moreover, the SpyTag/SpyCatcher

bonds have a high mechanical stability with a lifetime of more than one day, and a high mechanical strength of 131 pN [36]. The specific binding between SpyTag and SpyCatcher allows potential simplification of single-molecule force spectroscopy experiments.

In this chapter, I will demonstrate the development of a novel method by forming an unbreakable site-specific linkage with the application of the SpyTag/SpyCatcher bonds. The new system is very effective for single molecular experiments using optical tweezers. I will demonstrate the advantages, such as high mechanical stability and strength, high efficiency, and simplification by eliminating sample purification step. In Chapter 4, I will also provide an approach for measuring the domain-domain interactions in complexed proteins with abundant inner disulfide bonds, such as VWF, using the SpyTag system.

3.2   Materials and Methods

3.2.1   Materials

Synthetic SpyTag with C-terminal Cysteine (AHIVMVDAYKPTKGGC) and N-terminal Cysteine (CGGAHIVMVDAYKPTK) were purchased from Genscript (Piscataway, NJ). SpyCatcher, SpyCatcher EQ, and MPB-SpyTag were kindly provided by Mark Howarth's group at the University of Oxford. SpyCatcher EQ is a mutation of the catalytic Glu^{77} that prohibits isopeptide bond formation, and MPB-SpyTag is a fusion protein of MPB and SpyTag.

The proteins were first cloned in pDEST14 vector and were expressed using *E. coli* BL21 DE3 pLysS cells (Stratagene), while constructs cloned in pET28a were expressed using *E. coli* BL21 DE3 RIPL cells (Stratagene). Cultures were grown overnight in LB containing 0.1 mg/mL ampicillin and 0.034 mg/mL chloramphenicol (pDEST14) or 0.5

mg/mL kanamycin (pET28a). Overnight cultures were diluted 100-fold and grown at 37 °C to A600 0.5, then induced with 0.4 mM IPTG and grown at 30 °C for 4 h.

Nickel affinity chromatography following standard techniques was used to purify all proteins, except for SpyTag-MBP, which was purified using amylose-agarose (New England Biolabs) with 10 mM maltose elution. For MBP-SpyTag-Zif-SpyTag, binding buffer for the amylose agarose contained 600 mM NaCl to improve purity. After elution from the columns, proteins were dialyzed three times into PBS. Protein concentrations were determined using the Micro Bicinchoninic Acid (BCA) Assay kit (Thermo Scientific), following manufacturer's instructions.

3.2.2   Expression and Purification of SpyTag-$\alpha_4\beta_7$ Integrin

Recombinant Spy-tagged integrin constructs were constructed in the pHLsec vector. All cDNAs were cloned into the Age I and Xho I sites of the plasmid, which encodes an N-terminal secretion signal sequence and a C-terminal His$_6$ tag. Plasmids of α_4, β_7, and a biotinlygase A (provided by Mark Horwarth in Oxford) were co-transfected to HEK293T cells using MegaTran reagent (Origine). Culture supernatants were harvested after 5 days of transfection and proteins were purified using Ni-NTA affinity chromatography followed by size-exclusion chromatography [195].

3.2.3   Laser Optical Tweezers Measurement

Carboxyl-polystyrene beads of 2.0-µm diameter (Spherotech, Lake Forest, IL) were covalently coupled with streptavidin (Invitrogen) as described previously [53, 114]. SpyCatcher or SpyCatcher EQ was coupled with biotin-DNA handle (at 4 : 1 ratio) at room temperature (25 °C) for overnight first. To measure the mechanical stability and

strength of the SpyTag/SpyCatcher bonds, streptavidin-coated (SA) beads were incubated with C-terminal/N-terminal SpyTag for 10 min in Tris-buffered saline (150 mM NaCl, 10 mM Tris·HCl, pH 7.5) at 25 °C to couple the SpyTag. SpyCatcher and SpyCatcher EQ, with biotin-DNA handle, were then coupled to SA beads in a similar way, respectively. To further test the efficiency of SpyTag system, SpyTag was fused to maltose-binding protein (SpyTag-MBP). To apply the novel tagging method, we selected the complexed protein, integrin $\alpha_4\beta_7$. SpyTag-$\alpha_4\beta_7$ was prepared by fusing SpyTag to integrin $\alpha_4\beta_7$ on its N-terminal end (Section 3.2.2). Before the optical tweezers experiments, SpyTag-MBP, purified SpyTag-$\alpha_4\beta_7$, or non-purified SpyTag-$\alpha_4\beta_7$ supernatant was incubated with SA beads to immobilize the construct on the bead's surface. SpyCatcher with DNA handle was mixed with SA beads. Single-molecule pulling experiments were performed using an analytical mini-optical tweezers apparatus. One bead with one type of construct was fixed by the micropipette, while the other bead with the other type of construct was controlled by the optical trap. The single-molecule measurement was performed in the force-ramp mode, where the applied force increases linearly with the pulling distance. The pulling speeds were typically set to 50 nm/s, 100 nm/s, 150 nm/s, 200 nm/s, and 300 nm/s. The survival frequency, indicating the bonds stability, is calculated as the fraction of the binding events with a lifetime longer than a certain value t (seconds). To characterize the bio-mechanical properties of the protein, WLC model [32] is used to fit the force-extension data.

3.3   Results

3.3.1   Lifetime of the SpyTag/SpyCatcher Covalent Bonds

To quantify the mechanical stability and mechanical strength of the SpyTag/SpyCatcher covalent bonds, we decided to measure and plot the survival frequency versus the bond lifetime using mini-optical tweezers. Bond lifetimes were measured from the start of holding at a high force (~65 pN) to until the bond ruptured. Survival frequency is calculated as the fraction of the binding events with a lifetime longer than a certain value t, which is

$$f_i = \frac{n_{t \geq t_i}}{N} = 1 - \frac{n_{t < t_i}}{N} \tag{3.1}$$

where f_i is the survival frequency at the corresponding bond lifetime t_i, $n_{t \geq ti}$ is the count of events with bond lifetimes that are greater than t_i, and N is the total number of events.

Assuming the bond dissociation occurs from a single bond state, the bond survival probability can be described by a single exponential function

$$f_i = \exp(-k_{off} t_i) \tag{3.2}$$

where k_{off} is the intrinsic off rate of the bond. Eq. (3.2) also predicts that the logarithm of the bond survival probability is linearly correlated with the bond lifetime. Least squares fitting of the bond survival frequency to the bond lifetime gives an estimate of the intrinsic off rate, which is an indication of the bonds stability.

During an approach-retract cycle of the single-molecule pulling experiment, one trapped SA bead coupled with either C-SpyTag or N-SpyTag was brought into contact with another fixed SA bead, coupled with SpyCatcher (EQ) biotin-DNA handle, for a constant dwell time (~10 s) at low contact force (~5 pN), and then pulled away. Once a tether was successfully picked up, we tried to hold the trapped bead at a constant force

around DNA overstretching (~65 pN), and recorded the lifetime of the binding (Figure 3.1).
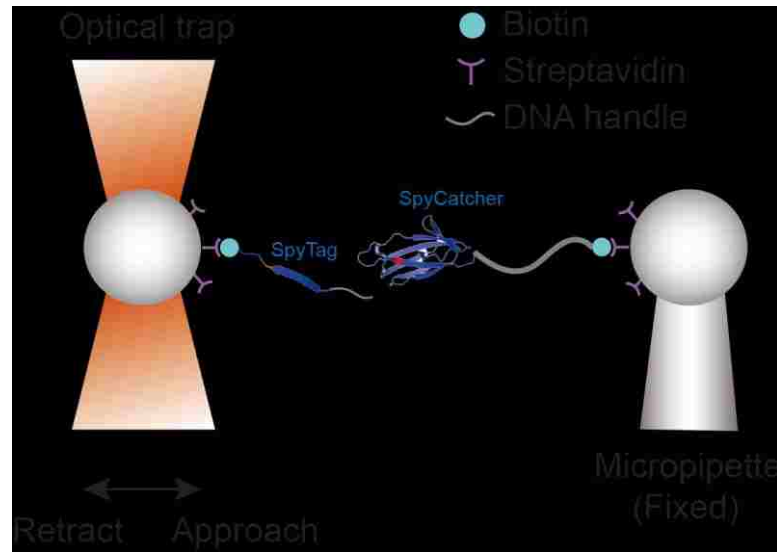
Figure 3.1 The optical tweezers setup to measure the mechanical properties of the SpyTag/SpyCatcher bonds. C-terminal/N-terminal SpyTag, SpyCatcher, and SpyCatcher EQ were used in the optical tweezers pulling experiments. During an approach-retract cycle of the single-molecule pulling experiment, one trapped SA bead coupled with either C-SpyTag or N-SpyTag was brought into contact with another fixed SA bead, which was coupled with SpyCatcher or SpyCatcher (EQ) biotin-DNA handle for a constant dwell time (~10 s) at a low contact force (~5 pN), and then pulled away. Once a tether was successfully picked up, we held the trapped bead at a constant force around DNA overstretching (~65 pN), and recorded the lifetime of the binding.

The plots of semi-log survival frequency versus lifetime for C-/N-SpyTag/SpyCatcher (or SpyCatcher EQ) are shown in Figure 3.2. Least squares fitting to the data from C-SpyTag/SpyCatcher EQ (red triangle) and N-SpyTag/SpyCatcher EQ (purple triangle) yielded

$$
\begin{aligned}
k_{off\text{C-SpyTag/SpyCatcher EQ}} &= 0.047 \pm 0.005 \text{ s}^{-1} \\
k_{off\text{N-SpyTag/SpyCatcher EQ}} &= 0.124 \pm 0.008 \text{ s}^{-1}
\end{aligned}
\tag{3.3}
$$

Neither C-SpyTag nor N-SpyTag formed any covalent bond with the mutant, SpyCatcher EQ, which was in good agreement with ref. [36]. For the interaction between C-SpyTag or N-SpyTag and SpyCatcher, the semi-log lifetime distributions appear as two line segments connected at ~100 s. It can be explained that the covalent bonds were formed for the segment where the lifetimes are more than ~100 s, while

they were not formed in the other segment. Least squares fitting to the data of long-lifetime segments yielded

(i)　　　When the non-covalent bonds formed (with fitting results shown as blue and green dashed lines in Figure 3.2):

$$k^1_{off_{\text{C-SpyTag/SpyCatcher}}} = 0.033 \pm 0.006 \text{ s}^{-1}$$
$$k^1_{off_{\text{N-SpyTag/SpyCatcher}}} = 0.029 \pm 0.003 \text{ s}^{-1}$$

(3.4)

These dissociation rates are similar to these in Eq. (3.3) indicating that the SpyTag/SpyCatcher covalent bonds were not formed for these data points.

(ii)　　　When the covalent bonds formed (with fitting results shown as blue and green lines in Figure 3.2):

$$k_{off_{\text{C-SpyTag/SpyCatcher}}} = (8.52 \pm 1.32) \times 10^{-4} \text{ s}^{-1}$$
$$k_{off_{\text{N-SpyTag/SpyCatcher}}} = (1.19 \pm 0.24) \times 10^{-3} \text{ s}^{-1}$$

(3.5)

We compared the bond lifetimes calculated by using the reciprocal of dissociation rates in Eq. (3.5) and Eq. (3.3), found that when the lifetimes of the covalent SpyTag/SpyCatcher bonds are approximately 100 to 150 times longer than that of the non-covalent bonds between SpyTag and SpyCatcher EQ. Furthermore, there is minimal difference in the covalent bonds lifetimes of C-SpyTag/SpyCatcher and N-SpyTag/SpyCatcher. It means that when fusing a desired protein with SpyTag, we can add SpyTag to either of its termini without sacrificing the covalent bond stability. This makes the single-molecule experiments simpler.
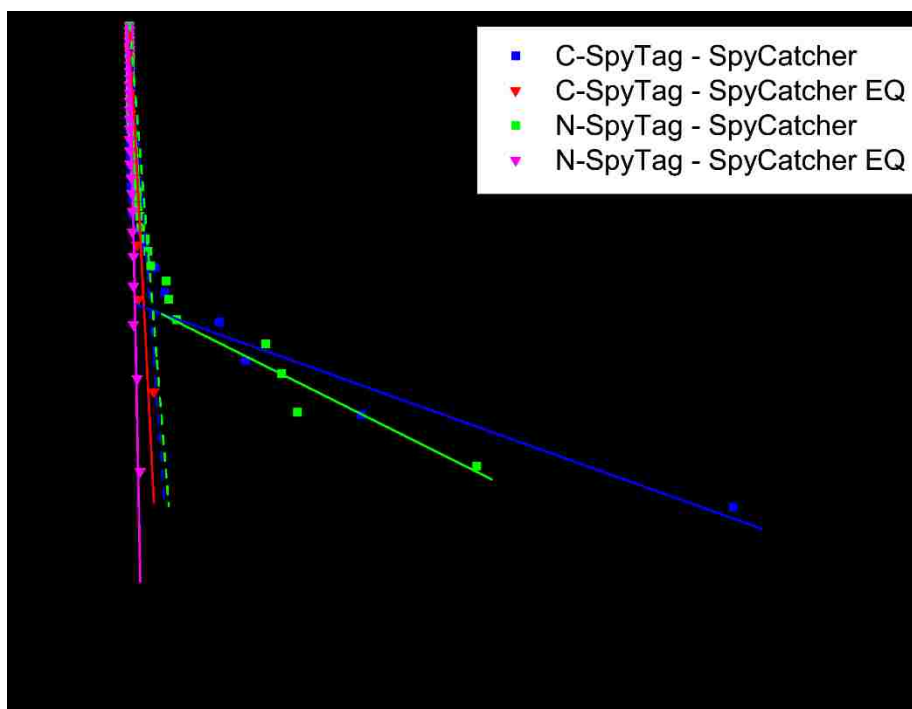
Figure 3.2 Semi-log survival frequency versus lifetime of SpyTag/SpyCatcher and SpyTag/SpyCatcher EQ bonds. Survival frequency is calculated as the fraction of the binding events with a lifetime longer than a certain value t. Assuming that the bond dissociation occurs from a single bond state, the logarithm of the bond survival probability is linearly correlated with the bond lifetime. Least squares fitting to the data of C-SpyTag/SpyCatcher EQ (red triangle) and N-SpyTag/SpyCatcher EQ (purple triangle) gives the intrinsic dissociation rate of 0.047 ± 0.005 s^{-1} and 0.124 ± 0.008 s^{-1}, respectively. For the interaction between C- or N-SpyTag and SpyCatcher, the distributions appears as two line segments connected at ~100 s. Fitting the two segments of longer lifetimes when the covalent bonds form, gives dissociation rates of $(8.52 \pm 1.32) \times 10^{-4}$ s^{-1} and 0.033 ± 0.006 s^{-1} for C-SpyTag/SpyCatcher, and $(1.19 \pm 0.24) \times 10^{-3}$ s^{-1} and 0.029 ± 0.003 s^{-1} for N-SpyTag/SpyCatcher, respectively. The lifetimes of the covalent SpyTag/SpyCatcher bonds are approximately 100 to 150 times longer than that of the non-covalent bonds between SpyTag and SpyCatcher EQ. Furthermore, there is minimal difference in the covalent bonds lifetimes of C-SpyTag/SpyCatcher and N-SpyTag/SpyCatcher.

We also plotted the force versus time from pulling SpyTag/SpyCatcher experiments (Figure 3.3). During each approach-retract cycle, one bead controlled by the optical trap approached the other fixed bead (shown as the blue trace), and was held to contact with each other for ~10 seconds of dwell time to allow the formation of SpyTag/SpyCatcher covalent bond. Once the covalent bond formed, the bead was pulled away and the force applied on this system increased gradually over time (red trace). When we saw the DNA overstretching ~65 pN, we held the bead to sustain at that force utilizing optical

tweezers' feedback system. During each pulling, we held the bonds at the same external preset force until they broke, then we could measure the lifetime from the plot directly. We found that the covalent bonds of SpyTag/SpyCatcher were stable to hold for as long as 1.4 h (Figure 3.3).

Therefore, our single-molecule experiment of pulling SpyTag/SpyCatcher and SpyTag/SpyCatcher EQ demonstrated that this novel system has remarkable advantages on mechanical stability and mechanical strength once the covalent bonds form.
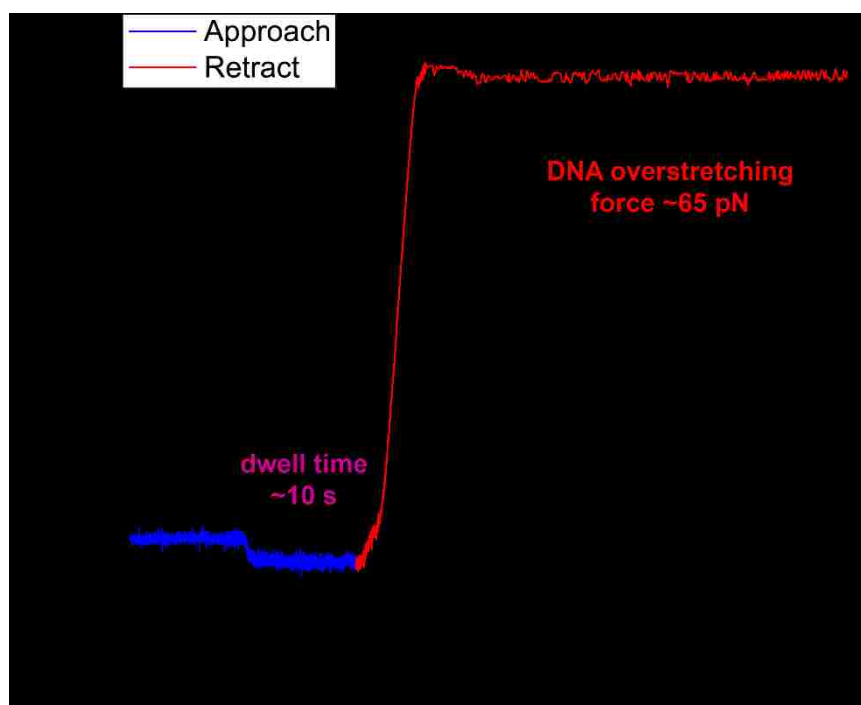
Figure 3.3 Mechanical strength of the SpyTag/SpyCatcher bonds. During each approach-retract cycle, one bead controlled by the optical trap approached the other fixed bead (blue trace), and was held to contact with each other for ~10 seconds of dwell time to form SpyTag/SpyCatcher covalent bonds. The bead was pulled away and the force applied on this system increased gradually over time (red trace). At the DNA overstretching ~65 pN, the bead was held to sustain at that force utilizing optical tweezers' feedback system. The covalent bonds of SpyTag/SpyCatcher were stable enough that the lifetime could be as long as 1.4 h.

3.3.2   Repeated Maltose-Binding Protein (MPB) Unfoldings with SpyTag

The first application of the novel SpyTag system is optical tweezers single-molecule force spectroscopy of the maltose-binding protein (MPB), which has already been well studied using different methods [36, 196–204]. In this application, we intended to demonstrate the prominent stability and efficiency of the new SpyTag system. SpyTag-MBP and SpyCatcher were expressed in *E. coli* and purified using Ni-NTA resin. SpyTag-MBP was incubated with SA beads—prepared as described previously—in Tris-buffered saline (150 mM NaCl, 10 mM Tris·HCl, pH 7.5) at 25 °C for 10 min. SpyCatcher was coupled with biotinylated DNA handle first, and then incubated with SA beads at the same condition. Before a good tether was picked up, one SpyTag-MPB-coupled bead was brought into contact with another fixed SpyCatcher-coupled bead for a constant dwell time (~2 s) at a low contact force (~5 pN) and then pulled away in each approach-retract cycle. After picking up a good tether, we did not allow the two beads to contact each other to eliminate further undesired bindings between other proteins. To realize that, we set a minimum force (above zero) to trigger the bead to retract before touching the other one. The tether is good when some unfolding events happen at ~30 pN, and can be further stretched to reach DNA overstretching, indicating that the covalent SpyTag/SpyCatcher bond is likely to be formed.
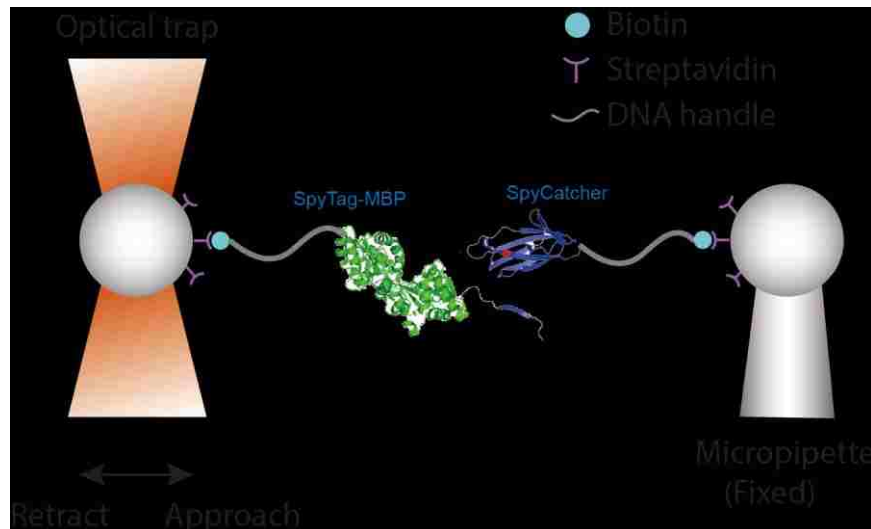
Figure 3.4 The optical tweezers setup to measure force-induced unfolding of MBP using the SpyTag system. MBP was fused with SpyTag to form SpyTag-MBP, incubated with SA beads for 10 min in Tris-buffered saline (150 mM NaCl, 10 mM Tris·HCl, pH 7.5) at 25 °C. SpyCatcher was coupled with biotinylated DNA handle first, and then incubated with SA beads for 10 min at the same condition. Before a good tether was picked up, one SpyTag-MPB-coupled bead was brought into contact with another fixed SpyCatcher-coupled bead, for a constant dwell time (~2 s) at a low contact force (~5 pN), and then pulled away in each approach-retract cycle.

Figure 3.5 shows 65 overlaid retract force-extension curves (approach force-extension curves are not shown here) from the pulling of a single tether at a pulling speed of 500 nm/s. The efficiency of the stable SpyTag system allows for acquiring a good histogram of the unfolding force or extension by performing the single-molecule experiments on one tether in one time. The unfolding force varied from ~10 pN to 50 pN, while the unfolding extension varied from ~40 nm to ~80 nm.
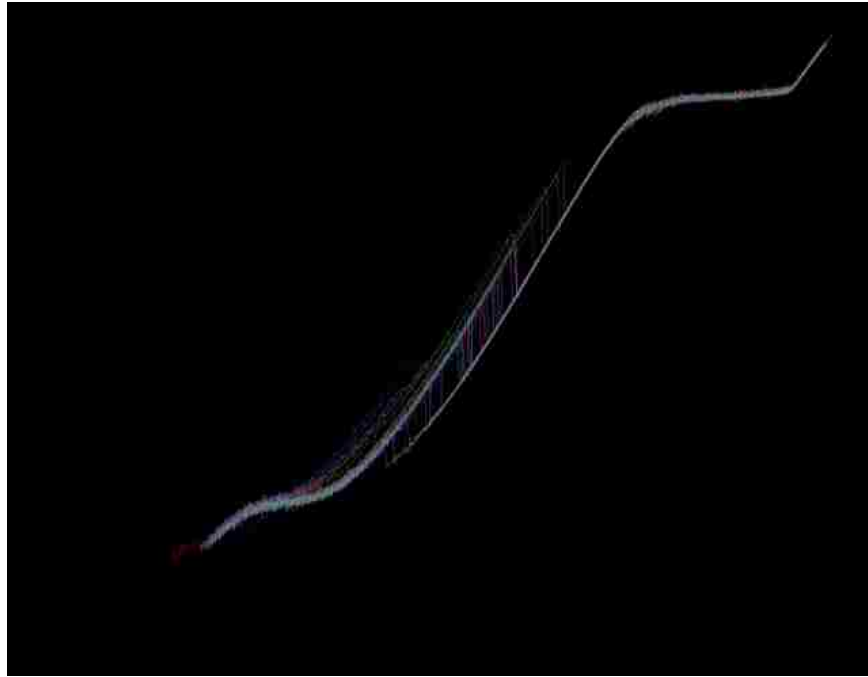
Figure 3.5 Overlaid force-extension curves of pulling MPB. 65 retract force-extension curves (approach force-extension curves are not shown here) from the pulling of one single SpyTag-MBP tether were overlapped together. The pulling speed is 500 nm/s. The efficiency of the stable SpyTag system allows for acquiring a good histogram of unfolding forces/extension by performing single-molecule experiments on one tether in one time. The unfolding force varied from ~10 pN to 50 pN, while the unfolding extension varied from ~40 nm to ~80 nm. The curves showed an intermediate state of MBP unfolding, as well as the normal native folded state and unfolded state.

To extract mechanical properties from these unfolding forces and extensions, a widely used statistical approach [53, 114, 205, 206] was employed. MBP force-extension data is shown in Figure 3.6. Unfolding extension was sorted by unfolding force into 5-pN bins. A histogram of extensions for each bin (inset) was fitted to Gaussian distribution (inset, solid line) to find the most probable extension, and the corresponding force was the mean value for forces within that bin (n per bin is 10 to 47). Error bars are the *SEM* for force and one *SD* for extension. The processed force-extension points were then fitted to the worm-like chain (WLC) model by error-weighted least squares [31, 207]. The WLC fit yielded a contour length of $L_c = 93.8 \pm 1.2$ nm and a persistence length of $L_p = 0.85 \pm 0.10$ nm. These results are in good agreement with previous work [200]. Moreover, when reconsidering the force-extension data shown in Figure 3.5, we found that there is an intermediate state of MBP,

other than the native folded state and the activated unfolded state. The intermediate state occurrs at a lower force (~25 pN) than the initial unfolding force. It is suggested that a further and more careful analysis of the contour length and the persistence length needs to be performed based on multiple peaks of the extension distribution, instead of considering it with merely one peak. In fact, the intermediate state of MBP unfolding has been reported in recent work [197, 199], and our fitted parameters are comparable with the published parameters.
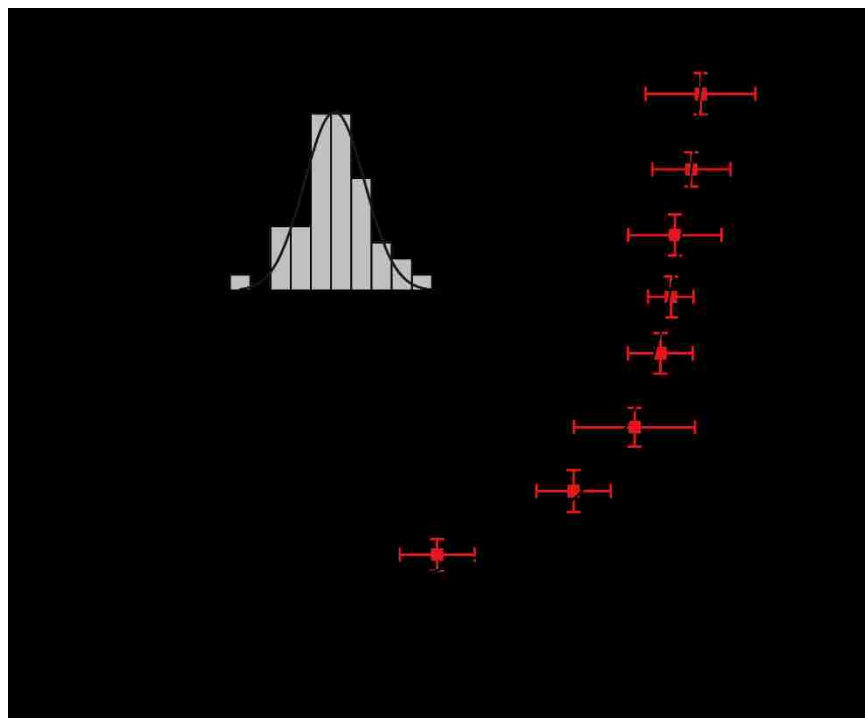
Figure 3.6 MBP force-extension data with an error weighted least squares fit to the WLC model. Unfolding extension was sorted by unfolding force into 5-pN bins. A histogram of extensions for each bin (inset) was fitted to Gaussian distribution (inset, solid line) to find the most probable extension, and the corresponding force was the mean value for forces within that bin (*n* per bin is 10 to 47). Error bars are the *SEM* for force and one *SD* for extension. The processed force-extension points were then fitted to the WLC model (black line) by error-weighted least squares [31, 207], and yielded a contour length of 93.8 ± 1.2 nm and a persistence length of 0.85 ± 0.10 nm.

Therefore, the first application of the newly developed SpyTag system on single maltose-binding protein (MBP) optical tweezers experiments has demonstrated its unprecedented advantage of experimental efficiency, i.e., with only one good tether

picked up, the system is capable of sustaining at a stable condition and observing a number of protein conformational events, such as unfolding or refolding.

3.3.3 Purification-Free Single-Molecule Pulling of a Complexed Protein: Integrin $\alpha_4\beta_7$

As described earlier at the beginning (in Section 1.3 and 3.1), the peptide SpyTag forms an amide covalent bond spontaneously with its protein partner, SpyCatcher. The reaction happens simply after they are mixed together, despite of diverse conditions of pH, temperature, and buffer [36]. Since SpyTag binds to SpyCatcher bonds specifically, we aimed to use this property to simply single-molecule force spectroscopy experiments. If we fuse the SpyTag gene sequence to the desired protein, e.g., von Willebrand factor (VWF) or integrin, and make it to be appropriately expressed, then we should be able to grab the protein fusion using SpyCatcher, thereby eliminating the protein purification step before single molecular experiments. Inspired by this idea, we performed the single molecular optical tweezers experiments on integrin $\alpha_4\beta_7$, a kind of complexed protein (Figure 1.7).

We performed the single-molecule pulling experiments of integrin $\alpha_4\beta_7$ with the new SpyTag system. In the first part, purified SpyTag-$\alpha_4\beta_7$ fusion was incubated with 10 times diluted SA beads, prepared as described previously, for 10 min in Tris-buffered saline (150 mM NaCl, 10 mM Tris·HCl, pH 7.5) at 25 °C. SpyCatcher was coupled with biotinylated DNA handle and then incubated with SA beads at the same condition. We used two different kinds of reaction buffer. One was the Tris-buffered saline with 1 mM Ca^{2+} and 1 mM Mg^{2+}, the other one was the Tris-buffered saline with no Ca^{2+} and 2 mM Mg^{2+} for the control experiment. 0.05% Tween 20 was used in both situations. During an approach-retract cycle, one SA bead coupled with SpyTag-$\alpha_4\beta_7$

was brought into contact with another fixed SpyCatcher-coupled bead for a constant dwell time (~2 s) at a low contact force (~5 pN), and then pulled away at a constant velocity (~200 nm/s). After a good tether was picked up, we set up a movement boundary for the optical trap to prevent the two beads from contacting each other again. Before contacting each other, the trapped bead retracted away. This action aimed to eliminating unnecessary bindings/interactions between molecules, since we hoped it to be at a single molecular level. We had no information about what would happen when some external force was applied on $\alpha_4\beta_7$, but we expected to see conformational changes or unfolding events when stretching it. We tried to repeat for more cycles when observing a DNA overstretching pattern from the pulling of a tether. If we did not observed any conformational change for many cycles, then we flushed away the two beads, and captured another two to repeat the experiments.

It is reported that there are about 1 mM Ca^{2+} and 1 mM Mg^{2+} and in blood and the existence of Ca^{2+} plays an important role in keeping integrins in an inactive state [208]. Therefore, in the single-molecule pulling experiments using Tris buffer with 1 mM Ca^{2+} and 1 mM Mg^{2+}, we expected to see the conformational changes of integrin $\alpha_4\beta_7$ from its inactive state to the active state under the stretched force, while in the control group using Tris buffer with only 2 mM Ca^{2+}, we expected to see no conformational change since it is in an extended activated state.

As expected, we observed a conformational change when pulling purified integrin $\alpha_4\beta_7$ (shown in Figure 3.7A). The red curves demonstrated that the conformational change occurring at a force of ~6 pN, and the protein's structure changed gradually to stretching force, instead of a sharp decrease of force seen in unfolding events. This phenomena could result from breaking the interactions between two legs of native $\alpha_4\beta_7$. The novel SpyTag system still showed its mechanical stability and strength.
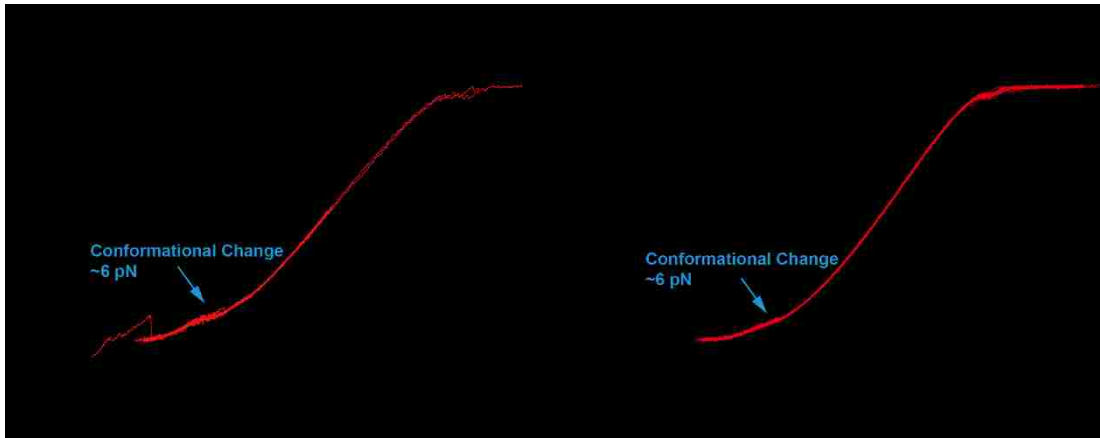
Figure 3.7 Single-molecule pulling of integrin $\alpha_4\beta_7$ with Ca^{2+}. (A) Overlaid retraction curves of pulling purified integrin $\alpha_4\beta_7$ in the single-molecule experiments. The buffer was Tris-buffered saline (150 mM NaCl, 10 mM Tris·HCl, pH 7.5) with 1 mM Ca^{2+} and 1 mM Mg^{2+}. A conformational change occurring at ~6 pN was observed. (B) Overlaid retraction curves of pulling integrin $\alpha_4\beta_7$ using its supernatant in the single-molecule experiments. The buffer was same as used in (A). A similar conformational change occurring at ~6 pN was observed.

In the second part, SpyTag-$\alpha_4\beta_7$ fusion was successfully expressed, but not purified. Similar to the sample preparations procedure described above, we incubated the SpyCatcher bio-handle with SA beads (diluted 10 fold). However, we incubated SA beads (diluted 10 fold) with SpyTag-$\alpha_4\beta_7$ fusion supernatant. It is not feasible to employ traditional tagging methods since the single-molecule measurement is not guaranteed. This time, we observed that a similar conformational change happened as that overserved when pulling purified integrin $\alpha_4\beta_7$ (shown in Figure 3.7B). The conformational change started at a similar force of ~6 pN, and no sharp unfolding events were observed. This phenomena again could arise from the breaking of the interactions between two legs of native $\alpha_4\beta_7$ integrin.
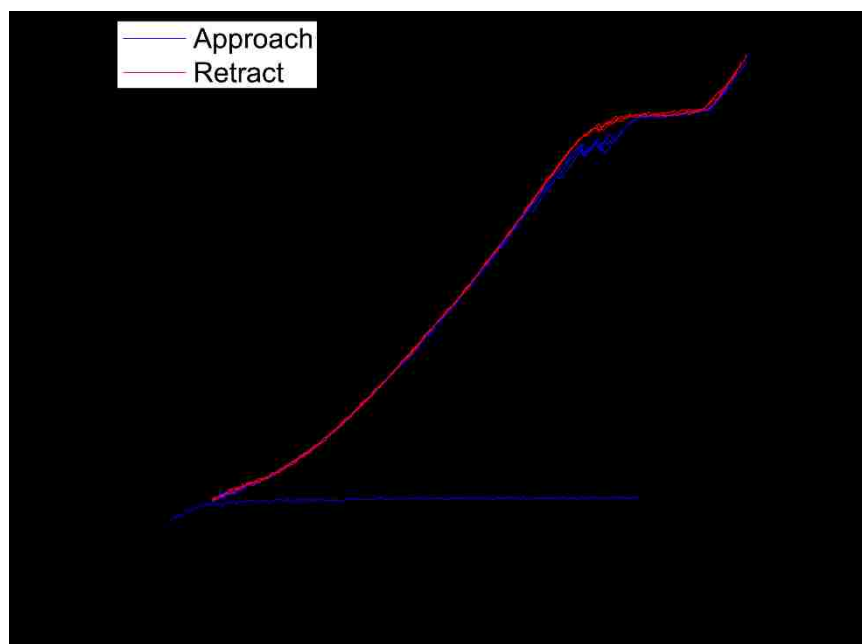
Figure 3.8 Single-molecule pulling of integrin $\alpha_4\beta_7$ without Ca^{2+}. Typical force-extension curves of pulling purified integrin $\alpha_4\beta_7$ in Tris buffer with 2 mM Mg^{2+} and no Ca^{2+}. The red line and blue line represent the retract process and approach process, respectively. DNA overstretching at ~65 pN was observed, and no conformational change of $\alpha_4\beta_7$ was seen.

Figure 3.8 shows typical force-extension curves from the pulling of purified integrin $\alpha_4\beta_7$ in Tris buffer with 2 mM Mg^{2+} and no Ca^{2+}. In the control experiment, DNA overstretching at ~65 pN was observed, and no conformational change of $\alpha_4\beta_7$ was seen, which agrees well with the fact that Ca^{2+} is required to keep integrins in an inactive state.

In order to precisely characterize the conformational change of integrin $\alpha_4\beta_7$ under force load, more single-molecule experiments need to be carried out to help make a more convincible conclusion. However, the application of the new SpyTag system did show its advantage over traditional systems by eliminating the sample purification step, as well as providing a new approach to investigate complexed proteins, such as integrin $\alpha_4\beta_7$.

3.4   Discussion and Conclusion

In this chapter, we intended to apply the SpyTag/SpyCatcher covalent bonds to develop an unbreakable site-specific linkage for single-molecule force measurements, especially for use with optical tweezers.

The new SpyTag system ensures high mechanical stability and mechanical strength. We found that the lifetimes of formed covalent SpyTag/SpyCatcher bonds are approximately 100 to 150 times longer than that of the non-covalent bonds between SpyTag and SpyCatcher EQ, and the covalent bonds of SpyTag/SpyCatcher are so stable that they can be held at a high force (~65 pN) for as long as 1.4 h. Furthermore, there is minimal difference in the lifetimes of C-SpyTag/SpyCatcher and N-SpyTag/SpyCatcher. This makes the single molecular experiments simpler, since we can fuse SpyTag to desired samples on either of its termini without sacrificing the covalent bonds stability.

We demonstrated the unprecedented advantages of experimental efficiency by applying the novel SpyTag system in single-molecule force experiments of pulling MBP. A good histogram of unfolding forces/extensions with 65 events, necessary for further data analysis, was directly obtained from the pulling of one tether at a pulling speed of 500 nm/s in one time. The fitted parameters, including the contour length and persistence length of MBP, agree well with published results [200]. We also observed an intermediate state of MBP. When necessary, we can further fit the force-loading rate data to the Bell–Evans model [33] and Dudko model [34], to extract the two-state free-energy landscape, including the spontaneous unfolding rate, the barrier width, and the barrier height.

The new SpyTag system showed that it can simplify the single-molecule experiments by eliminating the sample purification step, as well as providing a new

approach to investigate complexed proteins, such as integrin $\alpha_4\beta_7$. We observed, for the first time, the conformational change from the pulling of both purified integrin $\alpha_4\beta_7$ and non-purified integrin $\alpha_4\beta_7$, in the existence of Ca^{2+} (Figure 3.7). The conformational change both started at a small force of ~6 pN, and no sharp unfolding events were observed. This phenomena could come from the breaking of the interactions between two legs of native integrin $\alpha_4\beta_7$. Also, the control experiment showed no conformational change of pulling integrin $\alpha_4\beta_7$ in the absence of Ca^{2+}. However, in order to precisely characterize the conformational change of integrin $\alpha_4\beta_7$ under the external force, more single-molecule experiments need to be performed to help to make a more reliable conclusion.

The novel SpyTag system does not involve any protein reduction procedure, which makes it promising for measuring protein's domain-domain interactions, such as von Willebrand factor (VWF). This type of protein have disulfide bonds inside its internal structure, so the reduction reaction, required by some traditional single-molecule force spectroscopy methods, will also destroy the disulfide bonds and thus alter the structure and properties of the protein. In next chapter, I will show the study of VWF conformational change with/without the existence of factor VIII (FVIII), as well as new application of this novel SpyTag system.

3.5   Authorship Statement

In this project, Xiaohui (Frank) Zhang designed the research. The Synthetic SpyTag with C-terminal Cysteine (AHIVMVDAYKPTKGGC) or N-terminal Cysteine (CGGAHIVMVDAYKPTK) used in the single-molecule experiments was purchased from Genscript (Piscataway, NJ). The collaborator Dr. Mark Howarth at the University of Oxford provided the SpyCatcher and SpyTag-MBP fusion protein. Chenyu Wu

helped with the preparation of the integrin $\alpha_4\beta_7$. I performed all single-molecule experiments and analyzed the data.

Chapter 4: Exploring the Influence of FVIII in VWF Unfolding/Folding Process

4.1 Introduction

In physiologic hemostasis and pathologic thrombosis, the enhanced mechanical shear force generated by blood flow at the bleeding site triggers the activation of von Willebrand factor (VWF) multimers. The VWF multimers mediate the platelet adhesion to collagen by acting as an intermediary between collagen fibrils on damaged blood vessel walls and platelets in blood. Platelet aggregation, which is induced by the enhanced shear stress, requires the existence of VWF and its platelet surface receptor glycoprotein (GP) Ib-IX and integrin $\alpha_{IIb}\beta_3$ (GPIIb/IIIa) [50, 51]. The Springer group [53] discovered the mechanism of mechanoenzymatic cleavage of the ultralarge vascular protein VWF. The VWF multimers react to elongational forces and unfolds their A2 domains for cleavage by ADAMTS13. Recently Zhang *et al.* [58, 209] identified a juxtamembrane mechanosensitive domain in glycoprotein (GP) Ib-IX complex, the platelet receptor of VWF. It then proposed a trigger model where VWF-mediated pulling under fluid shear induces unfolding of the mechanosensory domain in GPIb-IX, and subsequently a conformational change in the adjacent extracellular domains of GPIbβ and GPIX occurs which sends in a signal across the platelet membrane to stimulate platelets [209].

One important VWF function is to serve as a carrier protein of human clotting factor VIII (FVIII) or antihemophilic factor [210]. FVIII has long been reported to have two distinct biological functions—coagulant activity and a role in primary hemostasis [49]. The native conformation of the D' domain of VWF (Figure 1.3) is required for both FVIII binding and normal multimerization and optimal secretion [211]. It is required to

form a noncovalent complex with VWF for the normal survival of FVIII in the blood circulation [212, 213]. The light chain of FVIII contains two distinct domains that associate with VWF. One domain is an acidic cluster in the amino terminus of A3 domain [214–217], and the other is the C2 domain [218, 219]. The C2 domain is comprised of the carboxy-terminal 159 amino acids and contains essential binding sites for VWF and is responsible for binding to platelet membrane surfaces [82, 87]. However, how FVIII binds to VWF and affects its function has remained elusive.

In this Chapter, I will show the single-molecule experiments on VWF fragments using optical tweezers and atomic force microscopy (AFM). The VWF fragments we investigated include D'-D3, D'-D3-A1, D'-D3-A1-A2, and A2 alone. In this way, we expected to see the domain-domain interactions within VWF. Meanwhile, we added FVIII to incubate with the fragments, so that we can explore the influence of FVIII in VWF unfolding/folding process. And also, since the traditional linking methods will break these inner disulfide bonds between VWF domains in the sample reduction step, we applied the newly developed SpyTag system (described in Chapter 3) to overcome this problem.

4.2   Materials and Methods

4.2.1   Materials

Synthetic SpyTag with C-terminal Cysteine (AHIVMVDAYKPTKGGC) or N-terminal Cysteine (CGGAHIVMVDAYKPTK) was purchased from Genscript (Piscataway, NJ). D'D3-SpyTag, D'D3A1-SpyTag, D'D3A1A2-SpyTag, and factor VIII (FVIII) were produced and kindly provided by Dr. X. Long Zheng at the University of Alabama at Birmingham. SpyCatcher was produced and kindly provided by Mark Howarth's group at the University of Oxford.

4.2.2   Expression of VWF A2

The cDNA of human VWF A2 domain (Pro^{1480} to Pro^{1678} with prepro-VWF numbering) was PCR-amplified with or without additional cysteines flanking the N and C termini added using PCR primers. All cDNAs were cloned into the Age I and Xho I sites of plasmid pHLsec [220], which encodes an N-terminal secretion signal sequence and a C-terminal His$_6$ tag. Plasmids were transfected to HEK293T cells using lipofectamine reagent (Invitrogen). Culture supernatants were harvested after 5 days of transfection and proteins were purified using Ni-NTA affinity chromatography followed by size-exclusion chromatography in 155 mM NaCl, 3 mM Na_2HPO_4, 1 mM KH_2PO_4 (PBS).

4.2.3   Coating of the Probes and Substrate

Factor VIII was coated to the cantilever, and D'D3A1A2 was coated to the dish surface. The detailed protocol of using gas-phase amino-silanization to coat the AFM cantilever and the dish is from http://www.jku.at/biophysics/content/e257042. The AFM probes used are soft Silicon Nitride cantilevers with Silicon Nitride tips (Bruker Nano Inc., model MLCT-UT). The dish used to coat VWF fragment is the common microscopy glass slide (75 × 25 × 1 mm).

4.2.4   Laser Optical Tweezers Measurement

Carboxyl-polystyrene beads of 2.0-μm diameter (Spherotech, Lake Forest, IL) were covalently coupled with streptavidin (Invitrogen) as described previously [53, 114]. SpyCatcher was coupled with biotin-DNA handle before the experiments.

For measuring the domain-domain interactions of VWF fragments, we performed the single-molecule experiments using optical tweezers. In preparation, streptavidin-coated (SA) beads were incubated with C-terminal/N-terminal SpyTag for 10 min in Tris-buffered saline (150 mM NaCl, 10 mM Tris·HCl, pH 7.5) at 25 °C to couple one kind of Spy-tagged VWF fragment. SpyCatcher was first coupled biotin-DNA handle, and then incubated with SA beads in a similar way. During the pulling experiments of each kind of VWF fragment, one SA bead with SpyCatcher-DNA handle on its surface was fixed by the micropipette, while another bead coupled with that kind of VWF fragment was trapped and controlled by the optical tweezers. The force measurement was performed in the force-ramp mode, where the stretching force increases linearly with the pulling distance. The pulling speeds were usually set to be 50 nm/s, 100 nm/s, 150 nm/s, 200 nm/s, and 300 nm/s. After observing interactions between the VWF domains, we added 5 nM FVIII to the reaction chamber and repeated the pulling experiments.

For the VWF A2 domain, we performed the single-molecule experiment using purified Spy-tagged A2 and Spy-tagged A2 supernatant. Meanwhile, we used A2-DNA handle, immobilized to two beads coated with streptavidin and anti-digoxigenin antibody, respectively.

When appropriate, the force-extension data (if there is some unfolding or conformational change) would be fitted to WLC model [32] to characterize its mechanical properties, and force-loading rate data would be fitted to the Bell–Evans model [33] or Dudko model [34] to depict the two-state free-energy landscape.

4.2.5 Atomic Force Microscopy (AFM) Force Measurement

To measure the interaction between FVIII and VWF D'-D3-A1-A2 fragment, I used a home-built atomic force microscopy (AFM) instrument (Figure 1.14), since the applied force from optical tweezers is too high for it to reach (~70 to 160 pN). The cantilever was coated with FVIII, while the dish substrate surface was coated with the VWF fragment, D'D3A1A2. The holder where the cantilever is fixed was controlled by the piezoelectric actuator. In one approach-retract cycle, the piezoelectric actuator brought the holder down to approach and pressed the coverslip's surface. By setting a trigger signal, the piezo state would stop to avoid damaging the cantilever. We also set a dwell time to allow longer interaction between the constructs (usually 1 s to 5 s). It is noticed that the part of the fragment that was picked up by the tip is random. Then the cantilever moved upward to retract within a distance of Z range. Five different pulling speeds with a reasonable range were performed to get five different force loading rates. The unbinding force-loading rate data was fitted to the Bell–Evans model [33] or Dudko model [34] to quantify the interactions.

4.3 Results

4.3.1 Pulling of D'D3 without FVIII

To measure the most simple domain-domain interactions in VWF, we pulled the shortest fragment D'D3 from VWF monomer using optical tweezers. The pulling velocity was 200 nm/s. Similar to other experiments, we brought the SpyTag-D'D3 coupled bead in contact with another fixed, SpyCatcher-DNA handle coupled bead, for a constant dwell time (~2 s) at a low contact force (~5 pN), and then pulled away. Once a good tether was picked up, we set a minimum force (above zero) to prevent the

moving bead from contacting with the fixed one. Repeated approach-retract recycles were performed until the bonds dissociated.

Figure 4.1 shows typical approach-retract force-distance curves of pulling D'D3 fragment, with a specific flat stage of DNA overstretching at ~65 pN. We observed some unfolding events during the retraction process (in Figure 4.2). The unfolding forces varied from ~10 pN to ~40 pN. The histogram of the unfolding extensions showed that the most probable unfolding distance is ~25 nm. However, there are few data points to make a solid conclusion.
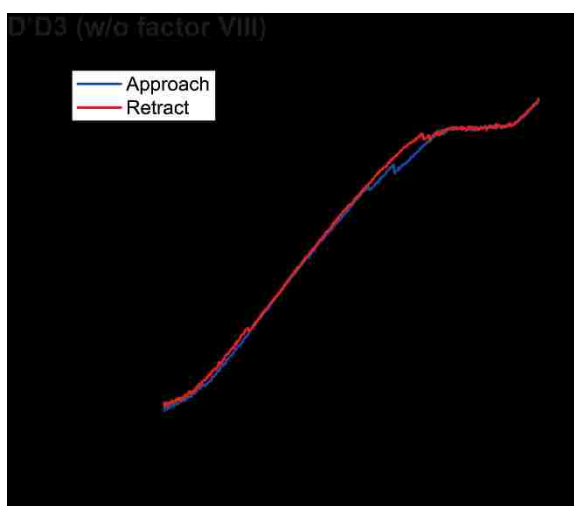
Figure 4.1 Single-molecule pulling results of D'D3 fragment. **T**ypical approach-retract force-distance curves with DNA overstretching at ~65 pN. Few unfolding events were observed in the experiments.

4.3.2   Pulling of D'D3A1 without FVIII

Similar to Section 4.3.1, we performed single-molecule experiments using optical tweezers. The pulling velocity was 200 nm/s. The VWF fragment used was D'D3A1, with an extra A1 domain than before. Initially, we did not add any FVIII to the reaction buffer. Figure 4.2A shows typical approach-retract force-distance curves from the pulling of D'D3A1 fragments including a pattern of DNA overstretching. More unfolding events were observed, compared with that from the pulling of D'D3. Some

93

refolding events were also observed. By fitting the histogram of the unfolding extension to the Gaussian distribution, we obtained the most probable extension of 22.8 ± 1.9 nm (Figure 4.2B). After adding 5 nM FVIII to the Tris buffer, we observed much less unfolding events.
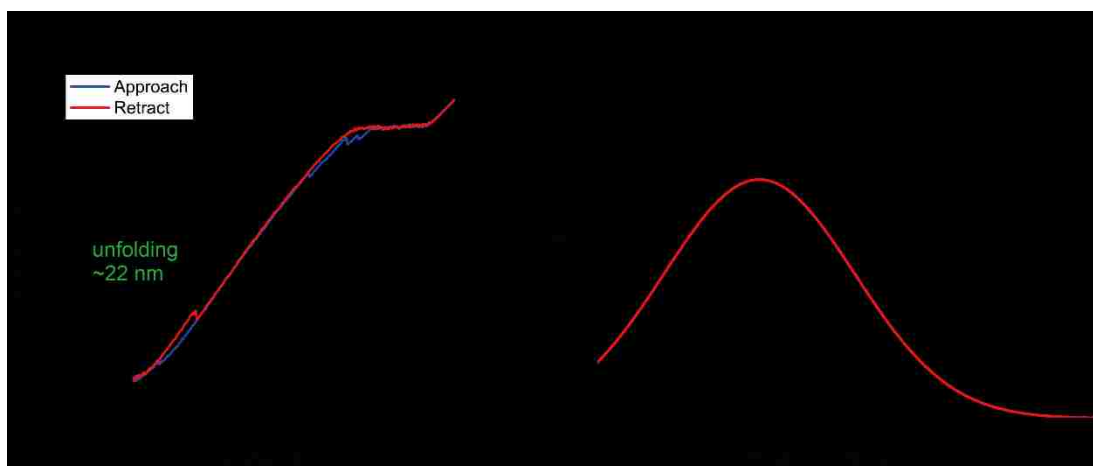
Figure 4.2 Single-molecule pulling results of D'D3A1 fragment. (A) Typical approach-retract force-distance curves from the pulling of D'D3A1 including a pattern of DNA overstretching. More unfolding events were observed, compared with that from the pulling of D'D3. Some refolding events were also observed. (B) The histogram of the unfolding extension. By fitting the histogram of the unfolding extension to the Gaussian distribution, we obtained the most probable extension of 22.8 ± 1.9 nm. After adding 5 nM FVIII to the Tris buffer, we observed much less unfolding events.

4.3.3   Pulling of D'D3A1A2 without FVIII

In a further study, we performed single-molecule experiments on VWF D'D3A1A2 fragment, in the absence of FVIII. Similar to Section 4.3.1, the optical tweezers were used to measure the force-induced conformational changes of D'D3A1A2. Three different pulling speeds, including 50 nm/s, 150 nm/s, and 200 nm/s, were used. We observed two unfolding events that occurred together in one retraction process (Figure 4.3A), which was different from pulling D'D3 or D'D3A1. The two unfolding events contain one short unfolding (~15 nm) and one long unfolding (~40 nm). The histogram of the unfolding extension was shown in Figure 4.3B. By fitting the histogram data to a 2-peak Gaussian distribution, we obtained a short extension of 17.9 ± 0.6 nm, and a

94

longer extension of 39.4 ± 2.5 nm. The longer one could be the unfolding of the VWF

A2 domain, while the shorter one might come from other parts of the fragment.

Figure 4.3 Single-molecule pulling results of D'D3A1A2 fragment, without FVIII. (A) Typical approach-retract force-distance curves from the pulling of D'D3A1A2 without FVIII. We observed two unfolding events that occurred together in one retraction process. (B) The histogram of the unfolding extension. By fitting the histogram data to a 2-peak Gaussian distribution, we obtained a short extension of 17.9 ± 0.6 nm, and a longer extension of 39.4 ± 2.5 nm. The longer one could be the unfolding of the VWF A2 domain, while the shorter one might come from other parts of the fragment.

4.3.4   Pulling of D'D3A1A2 with FVIII

After pulling D'D3A1A2 without FVIII, we added 5 nM FVIII to the buffer, and

saw the changes of force-extension curves (Figure 4.4A). It seemed that both the short

and long unfolding events disappeared. Instead, an intermediate unfolding of ~20 nm

appeared. By fitting the unfolding force histogram data to the Gaussian distribution

(Figure 4.4B), we found the most likely unfolding force is 24.5 ± 0.4 nm. This change

should be caused by the interaction between FVIII and D'D3A1A2, such that FVIII

changed the structure of D'D3A1A2 after binding to it.
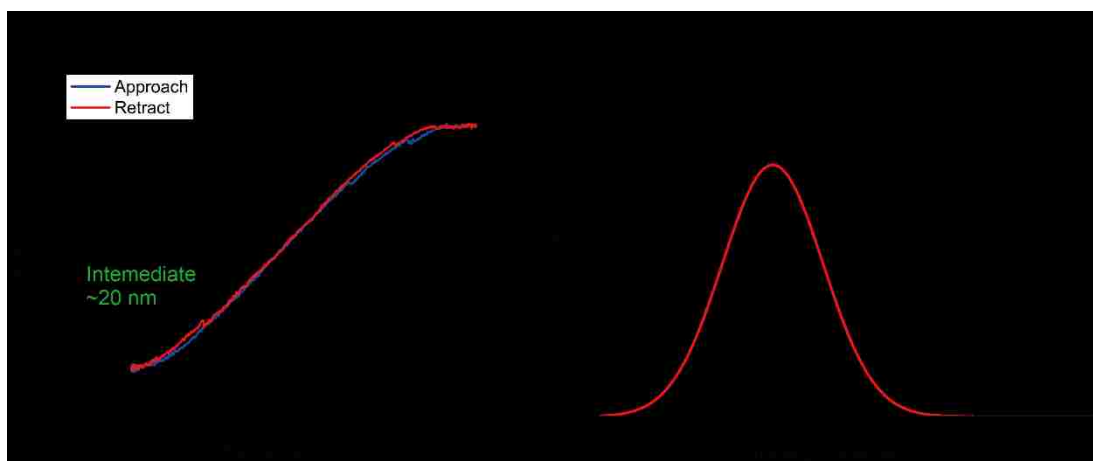
Figure 4.4 Single-molecule pulling results of D'D3A1A2 fragment, with FVIII. (A) Typical force-extension curves of pulling D'D3A1A2 with 5nM FVIII. It seemed that both the short and long unfolding events, seen when pulling D'D3A1A2 without FVIII disappeared. Instead, an intermediate unfolding of ~20 nm appeared. By fitting the unfolding force histogram data to the Gaussian distribution, we found the most likely unfolding force is 24.5 ± 0.4 nm. This change should be caused by the interaction between FVIII and D'D3A1A2, such that FVIII changed the structure of D'D3A1A2 after binding to it.

4.3.5   Interaction between FVIII and D'D3A1A2 Using AFM

In this subsection, we used the home-built AFM to measure the dynamic force spectrum of the FVIII–D'D3A1A2 interaction, since the unbinding forces are too high for optical tweezers. FVIII-coated cantilever was brought to interact with D'D3A1A2, immobilized on the dish surface. The cantilever was controlled by the piezoelectric actuator to move back and forward at a constant speed. A dwell time of ~1 s to 5 s was set to control the interaction time for bond formation. Five different pulling speeds were performed to get five different force loading rates. Rupture forces at 5 different loading rates/pulling speeds were plotted as histograms. Each histogram was fitted to a Gaussian curve to obtain the most probable force. Error bar on force is the *SEM* of the force. The red solid line (Figure 4.5) is the least squares fit of the data to the Bell–Evans model [33]. The fitting results showed that, the intrinsic off-rate of the binding is $k_0 =$

2.80 ± 1.03 s^{-1}, and the barrier width between the naive state and the transition state is $\Delta x^{\ddagger} = 1.70 \pm 0.18$ Å.
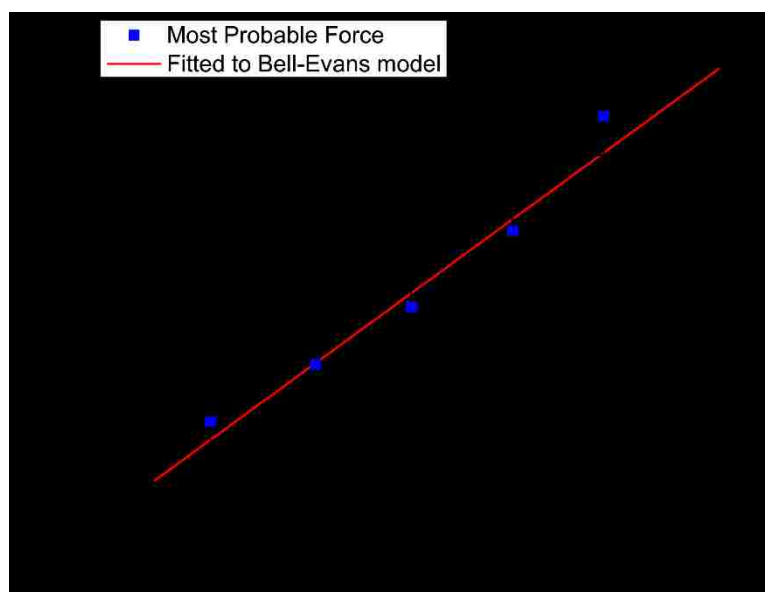
Figure 4.5 Dynamic force spectrum of D'D3A1A2–FVIII interaction. Five different pulling speeds were performed to get five different force loading rates. Rupture forces were plotted as histograms. Each histogram was fitted to a Gaussian curve to obtain the most probable force. Error bar on force is the *SEM* of the force. The red solid line is the least squares fit of the data to the Bell–Evans model [33]. The fitting results gave the intrinsic off-rate of the binding is $k_0 = 2.80 \pm 1.03$ s^{-1}, and the barrier width between the naive state and the transition state is $\Delta x^{\ddagger} = 1.70 \pm 0.18$ Å.

4.3.6   Pulling of VWF A2 Protein

In previous sections, we inferred that, after FVIII bound to FVIII, it might interact with A1A2 domains and altered A2 unfolding, so that we observed an intermediate state when pulling FVIII from the D'D3A1A2 fragment. However, whether FVIII interacts with A2 directly remains questionable. To answer this, we designed the single-molecule pulling experiments in two approaches. In the first approach, we used the newly developed SpyTag system (Chapter 3), where A2 was fused with SpyTag and not purified. Laser optical tweezers measurement was very similar to that described in Section 3.2.3 on the non-purified integrin $\alpha_4\beta_7$ supernatant. In the second approach, we coupled A2 domains with DNA handles through N- and C-terminal Cys tags. Two kinds

of carboxyl-polystyrene 2.0-µm beads (10 mg, Spherotech, Lake Forest, IL) were prepared. One kind of beads were the SA beads, described previously. The other kind of beads were coated with sheep anti-digoxigenin IgG (Roche) using a similar protocol, termed as anti-dig beads. Laser optical tweezers experiment was performed by pulling one anti-dig bead from the A2-handle, which was captured by one SA bead. In both approaches, we wanted to add FVIII after observing the typical unfolding of A2 domains, and see whether it directly changed the unfolding pathway of A2 domains.
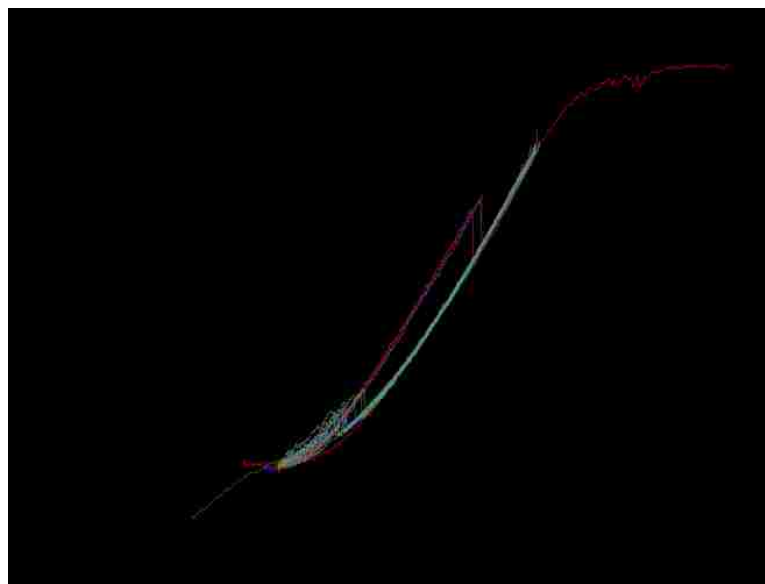
Figure 4.6 Overlaid retract force-extension curves of pulling A2 using the SpyTag system. The supernatant of SpyTag-A2, fused with SpyTag and A2 protein, was used. Colored traces are the pulling curves of A2. A typical DNA overstretching was observed (~65 pN). An unfolding event occurred at ~10 pN, which is comparable with [53]. Besides, another unfolding event occurred at a higher force ~45 pN, which might indicate that there existed an intermediate state. The newly developed SpyTag system still performed well in this experiment.

Figure 4.6 shows the overlaid force-extension curves (colored lines) of pulling A2 using the developed SpyTag system (Chapter 3). In this system, the VWF A2 protein was fused to SpyTag, and was not purified. Without the existence of FVIII, a typical pattern of DNA overstretching was observed (~65 pN). An unfolding event occurred at ~10 pN, which corresponded to the normal unfolding of the A2 domain reported in [53]. Besides, another unfolding event occurred at a higher force ~45 pN, which might

indicate that there existed an intermediate state from the pulling of SpyTag-A2 fusion protein. We can see that, the newly developed SpyTag system still performed well in this experiment.

In the second pulling system, we also observed the regular unfolding of the A2 domain with FVIII. Some preliminary results of its unfolding force and extension data are shown in Figure 4.7. The A2 protein, coupled with DNA handle, was immobilized by one SA bead, and one optical trap-controlled anti-dig bead was brought into contact with the SA bead and pulled away. The reaction buffer did not include FVIII. The unfolding extensions (~25 nm) and unfolding force (~10 pN) were comparable with published results [53]. When appropriate, the force-extension data would be fitted to the WLC model (Eq. (1.1)) to extract the contour length and the persistence of A2, and compared with published results.

Figure 4.7 Single-molecule pulling results of A2 protein, without FVIII. The results were obtained by pulling A2 protein captured by one SA bead from one anti-dig bead, without the existence of FVIII. The unfolding extensions (~25 nm) and unfolding force (~10 pN) were comparable with published results [53]. When appropriate, the force-extension data would be fitted to the WLC model to extract the contour length and the persistence of A2, and compared with published results.

After observing the regular unfolding of the A2 protein, we added 5 nM of FVIII into the Tris buffer (150 mM NaCl, 10 mM Tris·HCl, pH 7.5), and repeated the pulling experiments. We did observe the unfolding of the A2 protein. However, at this moment, we did not have enough unfolding events to compare the biomechanical properties of

A2 with these measured in absence of FVIII. Figure 4.8 shows a typical pulling curve of A2 with FVIII.
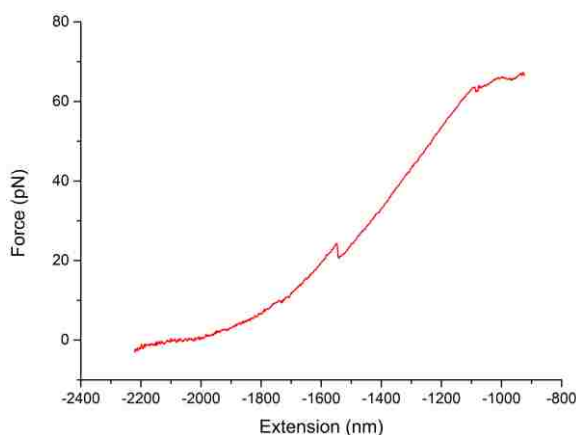
Figure 4.8 A typical retract curve of pulling A2, with FVIII. From the pulling of A2 protein with the existence of 5 nM FVIII, we observed an unfolding event, but could not know whether it was altered due to the lack of more events.

4.4   Discussion and Conclusion

These results have shown that there are some differences in the force spectrum of pulling D'D3A1 or D'D3A1A2, in the absence or presence of 5 nM factor VIII. However, in order to clearly clarify the function of FVIII and the interaction between FVIII and D'D3A1 or D'D3A1A2, we need to obtain more unfolding events. We need to extract the characteristics of unfoldings in both pulling D'D3A1 and D'D3A1A2, and compare the later one with VWF A2 unfolding pathways. Furthermore, we may need to use D'D3 generated by mammal cells, instead of bacteria cells to repeat the single-molecule experiments.

We expect to see that FVIII interacts with some sites either on VWF A1, A2, or somewhere between A1 and A2, to form a more stable complex. The new complex unfolds in a different way from A2, but with a longer lifetime. This will help to clarify the function of FVIII in platelet binding to membrane surfaces at the single molecular level.

4.5   Authorship Statement

In this project, Xiaohui (Frank) Zhang designed the research. The Synthetic SpyTag with C-terminal Cysteine (AHIVMVDAYKPTKGGC) or N-terminal Cysteine (CGGAHIVMVDAYKPTK) used in the single-molecule experiments was purchased from Genscript (Piscataway, NJ). The collaborator Dr. Mark Howarth at the University of Oxford provided the SpyCatcher. The collaborator Dr. X. Long Zheng at the University of Alabama at Birmingham provided the VWF fragments with SpyTag. We expressed the VWF A2 protein. I performed the optical tweezers experiments and analyzed the data.

Conclusion

Single-molecule experiments have been performed to study the biological and mechanical properties of proteins and molecular interactions [1, 2, 133]. There are a variety of different single-molecule techniques, including atomic force microscopy (AFM) [4–8], optical tweezers [9–19], magnetic tweezers [20–27], and biomembrane force probes (BFP) [28–30]. High spatial resolution (nanometers), temporal resolution (microseconds), and force sensitivity (piconewtons) can be achieved by using the developed instruments, based on these single-molecule techniques. The single-molecule experiments are carried out in the force-clamp mode, where a constant force is applied, or force-ramp mode, where the applied force increases linearly with the time, usually pulling at a constant speed. To quantify the biological properties of molecules, the molecule is treated as an elastic chain and the worm-like chain model [31, 32] is then applied. Furthermore, , the Bell–Evans model [33] and the Dudko model [34], both of which are derived from Kramers theory [35], can be applied to characterize the mechanical properties of proteins or bonds and to plot the free energy landscape.

In my first dissertation project [58, 206], we used the mini-optical tweezers to perform single-molecule force experiments on the platelet mechanosensor glycoprotein (GP) Ib-IX complex. The mechanical shear force generated by blood flow in the vasculature is an important factor that mediates physiologic hemostasis and pathologic thrombosis. Elevated shear stress induces binding of the von Willebrand factor (VWF) to the GPIb-IX complex on the platelet surface and induces platelet activation. Both GPIb-IX and VWF are capable of sensing and reacting to tensile forces. Earlier studies by the Springer group [53] have identified the mechanosensor within VWF, the A2 domain, which unfolds at a tensile force of 10–20 pN, and is cleaved by plasma enzyme ADAMTS13. Although GPIb-IX complex has long been recognized as the platelet

mechanosensor, how it senses the blood flow through its binding to VWF and converts this mechanical information into a protein-mediated signal that can be recognized and propagated has remained elusive. We successfully identified a juxtamembrane mechanosensory domain (MSD) in GPIb-IX, and further proposed a model of GPIb-IX mechanosensing (and further named it "the trigger model"). In this model, the force-induced unfolding of MSD is the step by which GPIb-IX converts a mechanical signal into a change in protein conformation, a type of signal that could be recognized and transduced further. This has significant implications for the pathogenesis and treatment of related blood diseases.

Though these single-molecule techniques and instruments have allowed for the direct pulling of single molecules, a well-designed system for holding the two ends of a molecule is necessary. Most of the traditional linkage systems offer low mechanical stability and strength. The disulfide coupling method is mechanically strong, but requires the reduction reaction to the protein sample, which is not practical for complexed proteins with an abundance of inner disulfide bonds, such as the VWF. Therefore, we aimed to develop a specific and strong covalent coupling method for single-molecule experiments.

In my second project, the novel SpyTag linkage has been developed and demonstrated to have high mechanical stability and strength. The covalent bonds of the SpyTag/SpyCatcher are very stable to the point where they can be held at high forces for as long as 1.4 h. Since there is not much difference between the lifetimes of the C-SpyTag/SpyCatcher and the N-SpyTag/SpyCatcher, we can add SpyTag to either of its termini without sacrificing the stability of the covalent bonds. This also makes the single molecular experiments simpler. The first application of this SpyTag system was on the single maltose-binding protein (MBP) pulling experiments, which showed its

unprecedented advantage of experimental efficiency. From the pulling of a single tether at a pulling speed of 500 nm/s, we obtained 65 good force-extension curves. The stable SpyTag system allowed us to perform single-molecule experiments in such an efficient way that a good histogram of unfolding forces/extension can be obtained using one single tether at a time. Fitting the unfolding force-extension data to the worm-like chain (WLC) model [31] yielded a comparable contour length and a persistence length with previous reports [200]. Moreover, the force extension curves indicated an intermediate state of MBP unfolding, at a lower force ~25 pN.

The new SpyTag system simplifies the single-molecule experiments by eliminating the sample purification step, as well as providing a new approach to investigate complexed proteins, such as the $\alpha_4\beta_7$ integrin. Moreover, the novel system eliminates the protein reduction procedure, which makes it promising for measuring protein's domain-domain interactions, such as the von Willebrand factor (VWF). This kind of protein has disulfide bonds inside its internal structure, so the reduction reaction, required by some traditional single-molecule force spectroscopy methods, destroys the disulfide bonds and thus alter the structure and properties of the protein.

Finally, in my third project, we aimed to investigate the domain-domain interactions within VWF, as well as the function of clotting factor VIII (FVIII) in VWF folding/unfolding, using the novel SpyTag system. There exists some difference in the force spectrum of pulling D'D3A1 or D'D3A1A2, in the absence or presence of the 5 nM factor VIII. However, more unfolding events are required to reveal the function of FVIII and the interaction between FVIII and D'D3A1 or D'D3A1A2. The function of FVIII on VWF A2 unfolding pathways should also be studied separately to further confirm FVIII's function.

In summary, my dissertation studies have provided a deeper understanding of the structure and function of GPIb-IX and VWF, and have significant implications for the pathogenesis and treatment of related blood diseases. In addition, the technical platforms developed, including the usage of SpyTag in optical tweezers experiments, is not limited to the chosen model system, and can potentially be applied to a broad range of protein structural and functional studies.

Publications

Zhang, W., Deng, W., Wang, Y., Zhou, L., Yang, W., Liang, X., *et al.* (2014). Identification of the mechanosensory domain in the platelet mechanosensor GPIb-IX complex. *Journal of Thrombosis and Haemostasis*, 12: 74–75.

Zhang, W., Deng, W., Zhou, L., Xu, Y., Yang, W., Liang, X, *et al.* (2015). Identification of a juxtamembrane mechanosensitive domain in the platelet mechanosensor glycoprotein Ib-IX complex. *Blood, 125*(3), 562–569.

Zhang, X., **Zhang, W**., Dragovich, M., Deng, W., & Li, R. (2016). Biophysical Characterization of Mechanosensors within the Plasma Protein von Willebrand Factor and its Receptor Platelet Glycoprotein Ib-IX. *Biophysical Journal, 3*(110), 637a.

Zhang W., Zhang, X. (2016). A Novel Method for Single Molecular Experiment using Optical Tweezers. (In preparation)

Zhang W. Deng, W., Zhang, X., Li R. (2016). Biophysical characterization of the mechanosensory domain within glycoprotein Ib-IX. (In preparation)

Zhang, W., Wang Y., Zhang X. (2016). Probing Internal Friction in the Mechanical Unfolding of Single Protein Molecule. (In preparation)

Appendix

Protocol of Coating the Polystyrene Beads

1. Take 100 μL 2.04-μm Carboxyl-polystyrene beads (Bangs Laboratories, Inc., Catalog# PC05N), and add to 1.5 mL Eppendorf tube.

2. Centrifuge at $720 \times$ G for 5 min, and remove the supernatant.

3. Dissolve the pellet with 0.4 mL PolyLink Coupling Buffer (Polysciences. Inc, Catalog# 2435A).

4. Repeat the steps 2–3–2 twice.

5. Add 0.2 mL PolyLink Coupling Buffer, same as before, to dissolve the pellet.

6. Freshly prepare 200 mg/mL EDAC solution by mixing 7 mg PolyLink EDAC (Polysciences, Inc., Catlaog# 2435C) with 35 μL PolyLink Coupling Buffer, same as before.

7. Take 10 μL EDAC solution prepared in step 6, and mix it with the beads in step 5.

8. Vortex for 10 min at room temperature.

9. Add the protein (streptavidin, antibody, or anti-digoxigenin) at a concentration of about 1 mg/mL.

10. Seal the tube with Parafilm M® film, and shake for 1 hour at room temperature.

11. Centrifuge at $720 \times$ G for 5 min, and remove the supernatant.

12. Wash 5 times with 0.4 mL PBS (with 0.02% Tween 20) for each time.

13. Add 0.2 mL PBS (with 0.02% Tween 20) and 0.2 mL PBS (with 2 mM Sodium azide) to the tube.

14. Store at 4 °C for future use.

Bibliography

1. Ritort, F., Single-molecule experiments in biological physics: methods and applications. *J Phys Condens Matter*, 2006. **18**(32): R531–83.

2. Sotomayor, M. & Schulten, K., Single-molecule experiments in vitro and in silico. *Science*, 2007. **316**(5828): 1144–8.

3. Neher, E., Sakmann, B., & Steinbach, J.H., The extracellular patch clamp: a method for resolving currents through individual open channels in biological membranes. *Pflugers Arch*, 1978. **375**(2): 219–28.

4. Binnig, G., Quate, C.F., & Gerber, C., Atomic Force Microscope. *Physical Review Letters*, 1986. **56**(9): 930–933.

5. Bustamante, C., Rivetti, C., & Keller, D.J., Scanning force microscopy under aqueous solutions. *Curr Opin Struct Biol*, 1997. **7**(5): 709–16.

6. Smith, B.L., The importance of molecular structure and conformation: learning with scanning probe microscopy. *Prog Biophys Mol Biol*, 2000. **74**(1–2): 93–113.

7. Zhang, X.H., Wojcikiewicz, E., & Moy, V.T., Force spectroscopy of the leukocyte function-associated antigen-1/intercellular adhesion molecule-1 interaction. *Biophysical Journal*, 2002. **83**(4): 2270–2279.

8. Kellermayer, M.S., Visualizing and manipulating individual protein molecules. *Physiol Meas*, 2005. **26**(4): R119–53.

9. Ashkin, A., Dziedzic, J.M., & Yamane, T., Optical trapping and manipulation of single cells using infrared laser beams. *Nature*, 1987. **330**(6150): 769–71.

10. Ashkin, A. & Dziedzic, J.M., Optical trapping and manipulation of viruses and bacteria. *Science*, 1987. **235**(4795): 1517–20.

11. Wang, M.D., Yin, H., Landick, R., Gelles, J., & Block, S.M., Stretching DNA with optical tweezers. *Biophys J*, 1997. **72**(3): 1335–46.

12. Block, S.M., Goldstein, L.S.B., & Schnapp, B.J., Bead Movement by Single Kinesin Molecules Studied with Optical Tweezers. *Nature*, 1990. **348**(6299): 348–352.

13. Novotny, L., Bian, R.X., & Xie, X.S., Theory of nanometric optical tweezers. *Physical Review Letters*, 1997. **79**(4): 645–648.

14. Ashkin, A., Optical trapping and manipulation of neutral particles using lasers. *Proc Natl Acad Sci U S A*, 1997. **94**(10): 4853–60.

15. Curtis, J.E., Koss, B.A., & Grier, D.G., Dynamic holographic optical tweezers. *Optics Communications*, 2002. **207**(1–6): 169–175.

16. Smith, S.B., Cui, Y., & Bustamante, C., Optical-trap force transducer that operates by direct measurement of light momentum. *Methods Enzymol*, 2003. **361**: 134–62.

17. Wen, J.D., Lancaster, L., Hodges, C., Zeri, A.C., Yoshimura, S.H., Noller, H.F., Bustamante, C., et al., Following translation by single ribosomes one codon at a time. *Nature*, 2008. **452**(7187): 598–603.

18. Cecconi, C., Shank, E.A., Dahlquist, F.W., Marqusee, S., & Bustamante, C., Protein-DNA chimeras for single molecule mechanical folding studies with the optical tweezers. *European Biophysics Journal with Biophysics Letters*, 2008. **37**(6): 729–738.

19. Zhong, M.C., Wei, X.B., Zhou, J.H., Wang, Z.Q., & Li, Y.M., Trapping red blood cells in living animals using optical tweezers. *Nat Commun*, 2013. **4**: 1768.

20.   Gosse, C. & Croquette, V., Magnetic Tweezers: Micromanipulation and Force Measurement at the Molecular Level. *Biophysical Journal*, 2002. **82**(6): 3314–3329.

21.   Haber, C. & Wirtz, D., Magnetic tweezers for DNA micromanipulation. *Review of Scientific instruments*, 2000. **71**(12): 4561–4570.

22.   Neuman, K.C. & Nagy, A., Single-molecule force spectroscopy: optical tweezers, magnetic tweezers and atomic force microscopy. *Nat Methods*, 2008. **5**(6): 491–505.

23.   Ribeck, N. & Saleh, O.A., Multiplexed single-molecule measurements with magnetic tweezers. *Review of Scientific Instruments*, 2008. **79**(9).

24.   Lipfert, J., Kerssemakers, J.W., Jager, T., & Dekker, N.H., Magnetic torque tweezers: measuring torsional stiffness in DNA and RecA-DNA filaments. *Nat Methods*, 2010. **7**(12): 977–80.

25.   De Vlaminck, I., Henighan, T., van Loenhout, M.T.J., Pfeiffer, I., Huijts, J., Kerssemakers, J.W.J., Katan, A.J., et al., Highly Parallel Magnetic Tweezers by Targeted DNA Tethering. *Nano Letters*, 2011. **11**(12): 5489–5493.

26.   De Vlaminck, I., Henighan, T., van Loenhout, M.T.J., Burnham, D.R., & Dekker, C., Magnetic Forces and DNA Mechanics in Multiplexed Magnetic Tweezers. *Plos One*, 2012. **7**(8).

27.   Lansdorp, B.M., Tabrizi, S.J., Dittmore, A., & Saleh, O.A., A high-speed magnetic tweezer beyond 10,000 frames per second. *Review of Scientific Instruments*, 2013. **84**(4).

28.   Merkel, R., Nassoy, P., Leung, A., Ritchie, K., & Evans, E., Energy landscapes of receptor-ligand bonds explored with dynamic force spectroscopy. *Nature*, 1999. **397**(6714): 50–53.

29. Evans, E., Ritchie, K., & Merkel, R., Sensitive force technique to probe molecular adhesion and structural linkages at biological interfaces. *Biophys J*, 1995. **68**(6): 2580–7.

30. Evans, E., Energy landscapes of biomolecular adhesion and receptor anchoring at interfaces explored with dynamic force spectroscopy. *Faraday Discuss*, 1998(111): 1–16.

31. Bustamante, C., Marko, J.F., Siggia, E.D., & Smith, S., Entropic elasticity of lambda-phage DNA. *Science*, 1994. **265**(5178): 1599–600.

32. Bustamante, C., Smith, S.B., Liphardt, J., & Smith, D., Single-molecule studies of DNA mechanics. *Curr Opin Struct Biol*, 2000. **10**(3): 279–85.

33. Evans, E. & Ritchie, K., Dynamic strength of molecular adhesion bonds. *Biophys J*, 1997. **72**(4): 1541–55.

34. Dudko, O.K., Hummer, G., & Szabo, A., Theory, analysis, and interpretation of single-molecule force spectroscopy experiments. *Proc Natl Acad Sci U S A*, 2008. **105**(41): 15755–60.

35. Kramers, H.A., Brownian motion in a field of force and the diffusion model of chemical reactions. *Physica*, 1940. **7**(4): 284–304.

36. Zakeri, B., Fierer, J.O., Celik, E., Chittock, E.C., Schwarz-Linek, U., Moy, V.T., & Howarth, M., Peptide tag forming a rapid covalent bond to a protein, through engineering a bacterial adhesin. *Proc Natl Acad Sci U S A*, 2012. **109**(12): E690–7.

37. Zdanowicz, M.M., *Essentials of pathophysiology for pharmacy*. 2002: CRC Press.

38. Porrett, P.M. & Drebin, J., *The Surgical Review: An Integrated Basic and Clinical Science Study Guide*. 2015: Lippincott Williams & Wilkins.

39.   Versteeg, H.H., Heemskerk, J.W., Levi, M., & Reitsma, P.H., New fundamentals in hemostasis. *Physiol Rev*, 2013. **93**(1): 327–58.

40.   Kauskot, A. & Hoylaerts, M.F., Platelet Receptors, in *Antiplatelet Agents*, P. Gresele, et al., Editors. 2012, Springer Berlin Heidelberg: Berlin, Heidelberg. 23–57.

41.   Pallister, C. & Watson, M., *Haematology*. 2nd ed. 2010: Scion Publishing.

42.   Dilley, A., Drews, C., Miller, C., Lally, C., Austin, H., Ramaswamy, D., Lurye, D., et al., von Willebrand disease and other inherited bleeding disorders in women with diagnosed menorrhagia. *Obstet Gynecol*, 2001. **97**(4): 630–6.

43.   Acharya, S.S., Coughlin, A., Dimichele, D.M., & North American Rare Bleeding Disorder Study, G., Rare Bleeding Disorder Registry: deficiencies of factors II, V, VII, X, XIII, fibrinogen and dysfibrinogenemias. *J Thromb Haemost*, 2004. **2**(2): 248–56.

44.   Sadler, J.E., Budde, U., Eikenboom, J.C., Favaloro, E.J., Hill, F.G., Holmberg, L., Ingerslev, J., et al., Update on the pathophysiology and classification of von Willebrand disease: a report of the Subcommittee on von Willebrand Factor. *J Thromb Haemost*, 2006. **4**(10): 2103–14.

45.   Gale, A.J., Continuing education course #2: current understanding of hemostasis. *Toxicol Pathol*, 2011. **39**(1): 273–80.

46.   Bolton-Maggs, P.H., Young Wan-Yin, B., McCraw, A.H., Slack, J., & Kernoff, P.B., Inheritance and bleeding in factor XI deficiency. *Br J Haematol*, 1988. **69**(4): 521–8.

47.   Tuddenham, E.G.D. & Cooper, D.N., *The molecular genetics of haemostasis and its inherited disorders*. 1994: Oxford University Press.

48.   World Federation of Hemophilia, *Report on the Annual Global Survey 2014*. 2015.

49.   Hoyer, L.W., The factor VIII complex: structure and function. *Blood*, 1981. **58**(1): 1–13.

50.   Moake, J.L., Turner, N.A., Stathopoulos, N.A., Nolasco, L.H., & Hellums, J.D., Involvement of large plasma von Willebrand factor (vWF) multimers and unusually large vWF forms derived from endothelial cells in shear stress-induced platelet aggregation. *J Clin Invest*, 1986. **78**(6): 1456–61.

51.   Peterson, D.M., Stathopoulos, N.A., Giorgio, T.D., Hellums, J.D., & Moake, J.L., Shear-induced platelet aggregation requires von Willebrand factor and platelet membrane glycoproteins Ib and IIb-IIIa. *Blood*, 1987. **69**(2): 625–8.

52.   Kroll, M.H., Hellums, J.D., McIntire, L.V., Schafer, A.I., & Moake, J.L., Platelets and shear stress. *Blood*, 1996. **88**(5): 1525–41.

53.   Zhang, X., Halvorsen, K., Zhang, C.Z., Wong, W.P., & Springer, T.A., Mechanoenzymatic cleavage of the ultralarge vascular protein von Willebrand factor. *Science*, 2009. **324**(5932): 1330–4.

54.   Springer, T.A., Biology and physics of von Willebrand factor concatamers. *J Thromb Haemost*, 2011. **9 Suppl 1**: 130–43.

55.   Springer, T.A., von Willebrand factor, Jedi knight of the bloodstream. *Blood*, 2014. **124**(9): 1412–25.

56.   Marti, T., Rosselet, S.J., Titani, K., & Walsh, K.A., Identification of disulfide-bridged substructures within human von Willebrand factor. *Biochemistry*, 1987. **26**(25): 8099–8109.

57. Katsumi, A., Tuley, E.A., Bodo, I., & Sadler, J.E., Localization of disulfide bonds in the cystine knot domain of human von Willebrand factor. *J Biol Chem*, 2000. **275**(33): 25585–94.

58. Zhang, W., Deng, W., Zhou, L., Xu, Y., Yang, W., Liang, X., Wang, Y., et al., Identification of a juxtamembrane mechanosensitive domain in the platelet mechanosensor glycoprotein Ib-IX complex. *Blood*, 2015. **125**(3): 562–9.

59. Dong, J.F., Moake, J.L., Nolasco, L., Bernardo, A., Arceneaux, W., Shrimpton, C.N., Schade, A.J., et al., ADAMTS-13 rapidly cleaves newly secreted ultralarge von Willebrand factor multimers on the endothelial surface under flowing conditions. *Blood*, 2002. **100**(12): 4033–9.

60. Savage, B., Sixma, J.J., & Ruggeri, Z.M., Functional self-association of von Willebrand factor during platelet adhesion under flow. *Proc Natl Acad Sci U S A*, 2002. **99**(1): 425–30.

61. Ulrichts, H., Vanhoorelbeke, K., Girma, J.P., Lenting, P.J., Vauterin, S., & Deckmyn, H., The von Willebrand factor self-association is modulated by a multiple domain interaction. *J Thromb Haemost*, 2005. **3**(3): 552–61.

62. Siedlecki, C.A., Lestini, B.J., Kottke-Marchant, K.K., Eppell, S.J., Wilson, D.L., & Marchant, R.E., Shear-dependent changes in the three-dimensional structure of human von Willebrand factor. *Blood*, 1996. **88**(8): 2939–50.

63. Savage, B., Saldivar, E., & Ruggeri, Z.M., Initiation of platelet adhesion by arrest onto fibrinogen or translocation on von Willebrand factor. *Cell*, 1996. **84**(2): 289–97.

64. Savage, B., Almus-Jacobs, F., & Ruggeri, Z.M., Specific synergy of multiple substrate-receptor interactions in platelet thrombus formation under flow. *Cell*, 1998. **94**(5): 657–66.

65. Schneider, S.W., Nuschele, S., Wixforth, A., Gorzelanny, C., Alexander-Katz, A., Netz, R.R., & Schneider, M.F., Shear-induced unfolding triggers adhesion of von Willebrand factor fibers. *Proc Natl Acad Sci U S A*, 2007. **104**(19): 7899–903.

66. Ruggeri, Z.M., Orje, J.N., Habermann, R., Federici, A.B., & Reininger, A.J., Activation-independent platelet adhesion and aggregation under elevated shear stress. *Blood*, 2006. **108**(6): 1903–10.

67. Hoylaerts, M.F., Yamamoto, H., Nuyts, K., Vreys, I., Deckmyn, H., & Vermylen, J., von Willebrand factor binds to native collagen VI primarily via its A1 domain. *Biochem J*, 1997. **324 (Pt 1)**: 185–91.

68. Nishida, N., Sumikawa, H., Sakakura, M., Shimba, N., Takahashi, H., Terasawa, H., Suzuki, E., et al., Collagen-binding mode of vWF-A3 domain determined by a transferred cross-saturation experiment. *Nat Struct Biol*, 2003. **10**(1): 53–8.

69. Bonnefoy, A., Romijn, R.A., Vandervoort, P.A., I, V.A.N.R., Vermylen, J., & Hoylaerts, M.F., von Willebrand factor A1 domain can adequately substitute for A3 domain in recruitment of flowing platelets to collagen. *J Thromb Haemost*, 2006. **4**(10): 2151–61.

70. Brondijk, T.H., Bihan, D., Farndale, R.W., & Huizinga, E.G., Implications for collagen I chain registry from the structure of the collagen von Willebrand factor A3 domain complex. *Proc Natl Acad Sci U S A*, 2012. **109**(14): 5253–8.

71. Emsley, J., Cruz, M., Handin, R., & Liddington, R., Crystal structure of the von Willebrand Factor A1 domain and implications for the binding of platelet glycoprotein Ib. *J Biol Chem*, 1998. **273**(17): 10396–401.

72. Zhang, Q., Zhou, Y.F., Zhang, C.Z., Zhang, X., Lu, C., & Springer, T.A., Structural specializations of A2, a force-sensing domain in the ultralarge vascular protein von Willebrand factor. *Proc Natl Acad Sci U S A*, 2009. **106**(23): 9226–31.

73. Huizinga, E.G., Tsuji, S., Romijn, R.A., Schiphorst, M.E., de Groot, P.G., Sixma, J.J., & Gros, P., Structures of glycoprotein Ibalpha and its complex with von Willebrand factor A1 domain. *Science*, 2002. **297**(5584): 1176–9.

74. Blenner, M.A., Dong, X., & Springer, T.A., Structural basis of regulation of von Willebrand factor binding to glycoprotein Ib. *J Biol Chem*, 2014. **289**(9): 5565–79.

75. Dumas, J.J., Kumar, R., McDonagh, T., Sullivan, F., Stahl, M.L., Somers, W.S., & Mosyak, L., Crystal structure of the wild-type von Willebrand factor A1-glycoprotein Ibalpha complex reveals conformation differences with a complex bearing von Willebrand disease mutations. *J Biol Chem*, 2004. **279**(22): 23327–34.

76. McEwan, P.A., Yang, W., Carr, K.H., Mo, X., Zheng, X., Li, R., & Emsley, J., Quaternary organization of GPIb-IX complex and insights into Bernard-Soulier syndrome revealed by the structures of GPIbbeta and a GPIbbeta/GPIX chimera. *Blood*, 2011. **118**(19): 5292–301.

77. Li, R. & Emsley, J., The organizing principle of the platelet glycoprotein Ib-IX-V complex. *J Thromb Haemost*, 2013. **11**(4): 605–14.

78. Modderman, P.W., Admiraal, L.G., Sonnenberg, A., & von dem Borne, A.E., Glycoproteins V and Ib-IX form a noncovalent complex in the platelet membrane. *J Biol Chem*, 1992. **267**(1): 364–9.

79.   Du, X., Beutler, L., Ruan, C., Castaldi, P.A., & Berndt, M.C., Glycoprotein Ib and glycoprotein IX are fully complexed in the intact platelet membrane. *Blood*, 1987. **69**(5): 1524–7.

80.   Luo, S.Z., Mo, X., Afshar-Kharghan, V., Srinivasan, S., Lopez, J.A., & Li, R., Glycoprotein Ibalpha forms disulfide bonds with 2 glycoprotein Ibbeta subunits in the resting platelet. *Blood*, 2007. **109**(2): 603–9.

81.   Nakamura, F., Pudas, R., Heikkinen, O., Permi, P., Kilpelainen, I., Munday, A.D., Hartwig, J.H., et al., The structure of the GPIb-filamin A complex. *Blood*, 2006. **107**(5): 1925–32.

82.   Shen, B.W., Spiegel, P.C., Chang, C.H., Huh, J.W., Lee, J.S., Kim, J., Kim, Y.H., et al., The tertiary structure and domain organization of coagulation factor VIII. *Blood*, 2008. **111**(3): 1240–7.

83.   Lenting, P.J., van Mourik, J.A., & Mertens, K., The life cycle of coagulation factor VIII in view of its structure and function. *Blood*, 1998. **92**(11): 3983–96.

84.   Ngo, J.C., Huang, M., Roth, D.A., Furie, B.C., & Furie, B., Crystal structure of human factor VIII: implications for the formation of the factor IXa-factor VIIIa complex. *Structure*, 2008. **16**(4): 597–606.

85.   Vehar, G.A., Keyt, B., Eaton, D., Rodriguez, H., O'Brien, D.P., Rotblat, F., Oppermann, H., et al., Structure of human factor VIII. *Nature*, 1984. **312**(5992): 337–42.

86.   Stoilova-McPhie, S., Villoutreix, B.O., Mertens, K., Kemball-Cook, G., & Holzenburg, A., 3-Dimensional structure of membrane-bound coagulation factor VIII: modeling of the factor VIII heterodimer within a 3-dimensional density map derived by electron crystallography. *Blood*, 2002. **99**(4): 1215–1223.

87. Pratt, K.P., Shen, B.W., Takeshima, K., Davie, E.W., Fujikawa, K., & Stoddard, B.L., Structure of the C2 domain of human factor VIII at 1.5 angstrom resolution. *Nature*, 1999. **402**(6760): 439–442.

88. Fay, P.J., Anderson, M.T., Chavin, S.I., & Marder, V.J., The size of human factor VIII heterodimers and the effects produced by thrombin. *Biochim Biophys Acta*, 1986. **871**(3): 268–78.

89. Vandieijen, G., Tans, G., Rosing, J., & Hemker, H.C., The Role of Phospholipid and Factor-Viiia in the Activation of Bovine Factor-X. *Journal of Biological Chemistry*, 1981. **256**(7): 3433–3442.

90. Hynes, R.O., Integrins: bi-directional, allosteric, signalling machines. *Cell*, 2002. **110**: 673–687.

91. Bouma, G. & Strober, W., The immunological and genetic basis of inflammatory bowel disease. *Nat Rev Immunol*, 2003. **3**(7): 521–33.

92. Rose, D.M., Han, J., & Ginsberg, M.H., Alpha4 integrins and the immune response. *Immunol Rev*, 2002. **186**: 118–24.

93. Luo, B.H., Carman, C.V., & Springer, T.A., Structural basis of integrin regulation and signaling. *Annu Rev Immunol*, 2007. **25**: 619–47.

94. Briskin, M.J., Mcevoy, L.M., & Butcher, E.C., Madcam-1 Has Homology to Immunoglobulin and Mucin-Like Adhesion Receptors and to Iga1. *Nature*, 1993. **363**(6428): 461–464.

95. Wang, J. & Springer, T.A., Structural specializations of immunoglobulin superfamily members for adhesion to integrins and viruses. *Immunol Rev*, 1998. **163**: 197–215.

96.   Johnston, J.A., Taub, D.D., Lloyd, A.R., Conlon, K., Oppenheim, J.J., & Kevlin, D.J., Human T lymphocyte chemotaxis and adhesion induced by vasoactive intestinal peptide. *J Immunol*, 1994. **153**(4): 1762–8.

97.   Bargatze, R.F., Jutila, M.A., & Butcher, E.C., Distinct roles of L-selectin and integrins α4β7 and LFA-1 in lymphocyte homing to Peyer's patch-HEV in situ: The multistep model confirmed and refined. *Immunity*, 1995. **3**: 99–108.

98.   Carman, C.V. & Springer, T.A., Integrin avidity regulation: are changes in affinity and conformation underemphasized? *Curr Opin Cell Biol*, 2003. **15**(5): 547–56.

99.   Xiao, T., Takagi, J., Coller, B.S., Wang, J.H., & Springer, T.A., Structural basis for allostery in integrins and binding to fibrinogen-mimetic therapeutics. *Nature*, 2004. **432**(7013): 59–67.

100.   de Chateau, M., Chen, S., Salas, A., & Springer, T.A., Kinetic and mechanical basis of rolling through an integrin and novel Ca^{2+}-dependent rolling and Mg^{2+}-dependent firm adhesion modalities for the α4β7-MAdCAM-1 interaction. *Biochemistry*, 2001. **40**(46): 13972–13979.

101.   Chen, J., Salas, A., & Springer, T.A., Bistable regulation of integrin adhesiveness by a bipolar metal ion cluster. *Nat Struct Biol*, 2003. **10**(12): 995–1001.

102.   Holm, L., Moody, P., & Howarth, M., Electrophilic affibodies forming covalent bonds to protein targets. *J Biol Chem*, 2009. **284**(47): 32906–13.

103.   Oke, M., Carter, L.G., Johnson, K.A., Liu, H., McMahon, S.A., Yan, X., Kerou, M., et al., The Scottish Structural Proteomics Facility: targets, methods and outputs. *J Struct Funct Genomics*, 2010. **11**(2): 167–80.

104. Hagan, R.M., Bjornsson, R., McMahon, S.A., Schomburg, B., Braithwaite, V., Buhl, M., Naismith, J.H., et al., NMR spectroscopic and theoretical analysis of a spontaneously formed Lys-Asp isopeptide bond. *Angew Chem Int Ed Engl*, 2010. **49**(45): 8421–5.

105. Zakeri, B. & Howarth, M., Spontaneous intermolecular amide bond formation between side chains for irreversible peptide targeting. *J Am Chem Soc*, 2010. **132**(13): 4526–7.

106. Li, L., Fierer, J.O., Rapoport, T.A., & Howarth, M., Structural analysis and optimization of the covalent association between SpyCatcher and a peptide Tag. *J Mol Biol*, 2014. **426**(2): 309–17.

107. Kang, H.J. & Baker, E.N., Intramolecular isopeptide bonds: protein crosslinks built for stress? *Trends Biochem Sci*, 2011. **36**(4): 229–37.

108. Smith, S.B., Cui, Y., & Bustamante, C., Overstretching B-DNA: the elastic response of individual double-stranded and single-stranded DNA molecules. *Science*, 1996. **271**(5250): 795–9.

109. Rubinstein, M.C.R.H., *Polymer physics*. 2006, Oxford; New York: Oxford University.

110. Odijk, T., Stiff Chains and Filaments under Tension. *Macromolecules*, 1995. **28**(20): 7016–7018.

111. Marko, J.F. & Siggia, E.D., Stretching DNA. *Macromolecules*, 1995. **28**(26): 8759–8770.

112. Bouchiat, C., Wang, M.D., Allemand, J., Strick, T., Block, S.M., & Croquette, V., Estimating the persistence length of a worm-like chain molecule from force-extension measurements. *Biophys J*, 1999. **76**(1 Pt 1): 409–13.

113. Cao, Y. & Li, H., Polyprotein of GB1 is an ideal artificial elastomeric protein. *Nat Mater*, 2007. **6**(2): 109–14.

114. Kim, J., Zhang, C.Z., Zhang, X., & Springer, T.A., A mechanically stabilized receptor-ligand flex-bond important in the vasculature. *Nature*, 2010. **466**(7309): 992–5.

115. Gross, P., Laurens, N., Oddershede, L.B., Bockelmann, U., Peterman, E.J.G., & Wuite, G.J.L., Quantifying how DNA stretches, melts and changes twist under tension. *Nature Physics*, 2011. **7**(9): 731–736.

116. Gore, J., Bryant, Z., Nollmann, M., Le, M.U., Cozzarelli, N.R., & Bustamante, C., DNA overwinds when stretched. *Nature*, 2006. **442**(7104): 836–9.

117. Lionnet, T., Joubaud, S., Lavery, R., Bensimon, D., & Croquette, V., Wringing out DNA. *Phys Rev Lett*, 2006. **96**(17): 178102.

118. Sheinin, M.Y. & Wang, M.D., Twist-stretch coupling and phase transition during DNA supercoiling. *Phys Chem Chem Phys*, 2009. **11**(24): 4800–3.

119. Hänggi, P., Talkner, P., & Borkovec, M., Reaction-rate theory: fifty years after Kramers. *Reviews of Modern Physics*, 1990. **62**(2): 251–341.

120. Uhlenbeck, G.E. & Ornstein, L.S., On the Theory of the Brownian Motion. *Physical Review*, 1930. **36**(5): 823–841.

121. Arrhenius, S., *Über die Reaktionsgeschwindigkeit bei der Inversion von Rohrzucker durch Säuren*. 1889: Wilhelm Engelmann.

122. Bell, G.I., Models for the specific adhesion of cells to cells. *Science*, 1978. **200**(4342): 618–27.

123. Zhurkov, S.N., Kinetic Concept of the Strength of Solids. *International Journal of Fracture*, 1984. **26**(4): 295–307.

124. Simson, D.A., Strigl, M., Hohenadl, M., & Merkel, R., Statistical breakage of single protein A-IgG bonds reveals crossover from spontaneous to force-induced bond dissociation. *Physical Review Letters*, 1999. **83**(3): 652–655.

125. Gergely, C., Voegel, J., Schaaf, P., Senger, B., Maaloum, M., Horber, J.K., & Hemmerle, J., Unbinding process of adsorbed proteins under external stress studied by atomic force microscopy spectroscopy. *Proc Natl Acad Sci U S A*, 2000. **97**(20): 10802–7.

126. Sekatskii, S.K., Benedetti, F., & Dietler, G., Dependence of the most probable and average bond rupture force on the force loading rate: First order correction to the Bell–Evans model. *Journal of Applied Physics*, 2013. **114**(3): 034701.

127. Carrion-Vazquez, M., Oberhauser, A.F., Fowler, S.B., Marszalek, P.E., Broedel, S.E., Clarke, J., & Fernandez, J.M., Mechanical and chemical unfolding of a single protein: a comparison. *Proc Natl Acad Sci U S A*, 1999. **96**(7): 3694–9.

128. Schwesinger, F., Ros, R., Strunz, T., Anselmetti, D., Guntherodt, H.J., Honegger, A., Jermutus, L., et al., Unbinding forces of single antibody-antigen complexes correlate with their thermal dissociation rates. *Proceedings of the National Academy of Sciences*, 2000. **97**(18): 9972–9977.

129. Schlierf, M. & Rief, M., Single-molecule unfolding force distributions reveal a funnel-shaped energy landscape. *Biophys J*, 2006. **90**(4): L33–5.

130. Cao, Y. & Li, H., How do chemical denaturants affect the mechanical folding and unfolding of proteins? *J Mol Biol*, 2008. **375**(1): 316–24.

131. Bullerjahn, J.T., Sturm, S., & Kroy, K., Theory of rapid force spectroscopy. *Nat Commun*, 2014. **5**: 4463.

132. Garg, A., Escape-field distribution for escape from a metastable potential well subject to a steadily increasing bias field. *Phys Rev B Condens Matter*, 1995. **51**(21): 15592–15595.

133. Dudko, O.K., Hummer, G., & Szabo, A., Intrinsic rates and activation free energies from single-molecule pulling experiments. *Phys Rev Lett*, 2006. **96**(10): 108101.

134. Hummer, G. & Szabo, A., Kinetics from nonequilibrium single-molecule pulling experiments. *Biophys J*, 2003. **85**(1): 5–15.

135. Raible, M., Evstigneev, M., Reimann, P., Bartels, F.W., & Ros, R., Theoretical analysis of dynamic force spectroscopy experiments on ligand-receptor complexes. *J Biotechnol*, 2004. **112**(1–2): 13–23.

136. Abramowitz, M. & Stegun, I.A., *Handbook of mathematical functions: with formulas, graphs, and mathematical tables*. Vol. 55. 1964: Courier Corporation.

137. Zhang, W., Mechanical stability and internal friction of GB1 protein. 2013.

138. Ray, C., Brown, J.R., & Akhremitchev, B.B., Rupture force analysis and the associated systematic errors in force spectroscopy by AFM. *Langmuir*, 2007. **23**(11): 6076–83.

139. Deniz, A.A., Mukhopadhyay, S., & Lemke, E.A., Single-molecule biophysics: at the interface of biology, physics and chemistry. *J R Soc Interface*, 2008. **5**(18): 15–45.

140. Neuman, K.C., Lionnet, T., & Allemand, J.F., Single-Molecule Micromanipulation Techniques. *Annual Review of Materials Research*, 2007. **37**(1): 33–67.

141. Greenleaf, W.J., Woodside, M.T., & Block, S.M., High-resolution, single-molecule measurements of biomolecular motion. *Annu Rev Biophys Biomol Struct*, 2007. **36**: 171–90.

142. Truong, K. & Ikura, M., The use of FRET imaging microscopy to detect protein–protein interactions and protein conformational changes in vivo. *Current Opinion in Structural Biology*, 2001. **11**(5): 573–578.

143. Pollok, B.A. & Heim, R., Using GFP in FRET-based applications. *Trends in Cell Biology*. **9**(2): 57–60.

144. Ni, Q. & Zhang, J., Dynamic visualization of cellular signaling. *Adv Biochem Eng Biotechnol*, 2010. **119**: 79–97.

145. Sekar, R.B. & Periasamy, A., Fluorescence resonance energy transfer (FRET) microscopy imaging of live cell protein localizations. *J Cell Biol*, 2003. **160**(5): 629–33.

146. Holden, S.J., Uphoff, S., Hohlbein, J., Yadin, D., Le Reste, L., Britton, O.J., & Kapanidis, A.N., Defining the limits of single-molecule FRET resolution in TIRF microscopy. *Biophys J*, 2010. **99**(9): 3102–11.

147. Berezin, M.Y. & Achilefu, S., Fluorescence lifetime measurements and biological imaging. *Chem Rev*, 2010. **110**(5): 2641–84.

148. Auton, M., Sowa, K.E., Behymer, M., & Cruz, M.A., N-terminal flanking region of A1 domain in von Willebrand factor stabilizes structure of A1A2A3 complex and modulates platelet activation under shear stress. *J Biol Chem*, 2012. **287**(18): 14579–85.

149. Tischer, A., Madde, P., Blancas-Mejia, L.M., & Auton, M., A molten globule intermediate of the von Willebrand factor A1 domain firmly tethers platelets under shear flow. *Proteins*, 2014. **82**(5): 867–78.

150. De Marco, L., Girolami, A., Zimmerman, T.S., & Ruggeri, Z.M., Interaction of purified type IIB von Willebrand factor with the platelet membrane glycoprotein Ib induces fibrinogen binding to the glycoprotein IIb/IIIa complex and initiates aggregation. *Proc Natl Acad Sci U S A*, 1985. **82**(21): 7424–8.

151. Goto, S., Salomon, D.R., Ikeda, Y., & Ruggeri, Z.M., Characterization of the unique mechanism mediating the shear-dependent binding of soluble von Willebrand factor to platelets. *J Biol Chem*, 1995. **270**(40): 23352–61.

152. Du, X., Signaling and regulation of the platelet glycoprotein Ib-IX-V complex. *Curr Opin Hematol*, 2007. **14**(3): 262–9.

153. McEwan, P.A., Yang, W., Carr, K.H., Mo, X., Zheng, X., Li, R., & Emsley, J., Quaternary organization of GPIb-IX complex and insights into Bernard-Soulier syndrome revealed by the structures of GPIbβ and a GPIbβ/GPIX chimera. *Blood*, 2011. **118**(19): 5292–301.

154. Huizinga, E.G., Tsuji, S., Romijn, R.A., Schiphorst, M.E., de Groot, P.G., Sixma, J.J., & Gros, P., Structures of glycoprotein Iba and its complex with von Willebrand factor A1 domain. *Science*, 2002. **297**(5584): 1176–9.

155. Yago, T., Lou, J., Wu, T., Yang, J., Miner, J.J., Coburn, L., Lopez, J.A., et al., Platelet glycoprotein Ibalpha forms catch bonds with human WT vWF but not with type 2B von Willebrand disease vWF. *J Clin Invest*, 2008. **118**(9): 3195–207.

156. Ju, L., Dong, J.F., Cruz, M.A., & Zhu, C., The N-terminal flanking region of the A1 domain regulates the force-dependent binding of von Willebrand factor to platelet glycoprotein Ibalpha. *J Biol Chem*, 2013. **288**(45): 32289–301.

157. Fox, J.E., Aggerbeck, L.P., & Berndt, M.C., Structure of the glycoprotein Ib-IX complex from platelet membranes. *J Biol Chem*, 1988. **263**(10): 4882–90.

158. Lopez, J.A., Leung, B., Reynolds, C.C., Li, C.Q., & Fox, J.E., Efficient plasma membrane expression of a functional platelet glycoprotein Ib-IX complex requires the presence of its three subunits. *J Biol Chem*, 1992. **267**(18): 12851–9.

159. Lopez, J.A., Andrews, R.K., Afshar-Kharghan, V., & Berndt, M.C., Bernard-Soulier syndrome. *Blood*, 1998. **91**(12): 4397–418.

160. Lanza, F., Bernard-Soulier syndrome (hemorrhagiparous thrombocytic dystrophy). *Orphanet J Rare Dis*, 2006. **1**: 46.

161. Berndt, M.C. & Andrews, R.K., Bernard-Soulier syndrome. *Haematologica*, 2011. **96**(3): 355–9.

162. Call, M.E., Pyrdol, J., Wiedmann, M., & Wucherpfennig, K.W., The organizing principle in the formation of the T cell receptor-CD3 complex. *Cell*, 2002. **111**(7): 967–79.

163. Rutledge, T., Cosson, P., Manolios, N., Bonifacino, J.S., & Klausner, R.D., Transmembrane helical interactions: zeta chain dimerization and functional association with the T cell antigen receptor. *EMBO J*, 1992. **11**(9): 3245–54.

164. Huang, C., Lu, C., & Springer, T.A., Folding of the conserved domain but not of flanking regions in the integrin beta2 subunit requires association with the alpha subunit. *Proc Natl Acad Sci U S A*, 1997. **94**(7): 3156–61.

165. Huang, C. & Springer, T.A., Folding of the beta-propeller domain of the integrin alphaL subunit is independent of the I domain and dependent on the beta2 subunit. *Proc Natl Acad Sci U S A*, 1997. **94**(7): 3162–7.

166. Zhou, L., Yang, W., & Li, R., Analysis of inter-subunit contacts reveals the structural malleability of extracellular domains in platelet glycoprotein Ib-IX complex. *J Thromb Haemost*, 2014. **12**(1): 82–9.

167. Mo, X., Lu, N., Padilla, A., Lopez, J.A., & Li, R., The transmembrane domain of glycoprotein Ibbeta is critical to efficient expression of glycoprotein Ib-IX complex in the plasma membrane. *J Biol Chem*, 2006. **281**(32): 23050–9.

168. Luo, S.Z. & Li, R., Specific heteromeric association of four transmembrane peptides derived from platelet glycoprotein Ib-IX complex. *J Mol Biol*, 2008. **382**(2): 448–57.

169. Mo, X., Nguyen, N.X., McEwan, P.A., Zheng, X., Lopez, J.A., Emsley, J., & Li, R., Binding of platelet glycoprotein Ibbeta through the convex surface of leucine-rich repeats domain of glycoprotein IX. *J Thromb Haemost*, 2009. **7**(9): 1533–40.

170. Zhang, X., Chen, A., De Leon, D., Li, H., Noiri, E., Moy, V.T., & Goligorsky, M.S., Atomic force microscopy measurement of leukocyte-endothelial interaction. *Am J Physiol Heart Circ Physiol*, 2004. **286**(1): H359–67.

171. Beckett, D., Kovaleva, E., & Schatz, P.J., A minimal peptide substrate in biotin holoenzyme synthetase-catalyzed biotinylation. *Protein Sci*, 1999. **8**(4): 921–9.

172. del Rio, A., Perez-Jimenez, R., Liu, R., Roca-Cusachs, P., Fernandez, J.M., & Sheetz, M.P., Stretching single talin rod molecules activates vinculin binding. *Science*, 2009. **323**(5914): 638–41.

173. Mo, X., Luo, S.Z., Lopez, J.A., & Li, R., Juxtamembrane basic residues in glycoprotein Ibbeta cytoplasmic domain are required for assembly and surface expression of glycoprotein Ib-IX complex. *FEBS Lett*, 2008. **582**(23–24): 3270–4.

174. Schatz, P.J., Use of peptide libraries to map the substrate specificity of a peptide-modifying enzyme: a 13 residue consensus peptide specifies biotinylation in Escherichia coli. *Biotechnology (N Y)*, 1993. **11**(10): 1138–43.

175. Mo, X., Lu, N., Padilla, A., Lopez, J.A., & Li, R.H., The transmembrane domain of glycoprotein Ib beta is critical to efficient expression of glycoprotein Ib-IX complex in the plasma membrane. *Journal of Biological Chemistry*, 2006. **281**(32): 23050–23059.

176. Luo, S.Z., Mo, X., Lopez, J.A., & Li, R., Role of the transmembrane domain of glycoprotein IX in assembly of the glycoprotein Ib-IX complex. *J Thromb Haemost*, 2007. **5**(12): 2494–502.

177. Shank, E.A., Cecconi, C., Dill, J.W., Marqusee, S., & Bustamante, C., The folding cooperativity of a protein is controlled by its chain topology. *Nature*, 2010. **465**(7298): 637–40.

178. Stephenson, W., Asare-Okai, P.N., Chen, A.A., Keller, S., Santiago, R., Tenenbaum, S.A., Garcia, A.E., et al., The essential role of stacking adenines in a two-base-pair RNA kissing complex. *J Am Chem Soc*, 2013. **135**(15): 5602–11.

179. Berndt, M.C., Du, X.P., & Booth, W.J., Ristocetin-dependent reconstitution of binding of von Willebrand factor to purified human platelet membrane glycoprotein Ib-IX complex. *Biochemistry*, 1988. **27**(2): 633–40.

180. Oesterhelt, F., Oesterhelt, D., Pfeiffer, M., Engel, A., Gaub, H.E., & Muller, D.J., Unfolding pathways of individual bacteriorhodopsins. *Science*, 2000. **288**(5463): 143–6.

181. Preiner, J., Janovjak, H., Rankl, C., Knaus, H., Cisneros, D.A., Kedrov, A., Kienberger, F., et al., Free energy of membrane protein unfolding derived from single-molecule force measurements. *Biophys J*, 2007. **93**(3): 930–7.

182. Chen, J.M. & Lopez, J.A., The mysteries of a platelet adhesion receptor. *Blood*, 2005. **105**(11): 4154–4155.

183. Louis-Jeune, C., Andrade-Navarro, M.A., & Perez-Iratxeta, C., Prediction of protein secondary structure from circular dichroism using theoretically derived spectra. *Proteins*, 2012. **80**(2): 374–81.

184. Miura, S., Li, C.Q., Cao, Z., Wang, H., Wardell, M.R., & Sadler, J.E., Interaction of von Willebrand factor domain A1 with platelet glycoprotein Ibα-(1-289). Slow intrinsic binding kinetics mediate rapid platelet adhesion. *Journal of biological chemistry*, 2000. **275**(11): 7539–46.

185. Yan, R., Mo, X., Paredes, A.M., Dai, K., Lanza, F., Cruz, M.A., & Li, R., Reconstitution of the platelet glycoprotein Ib-IX complex in phospholipid bilayer Nanodiscs. *Biochemistry*, 2011. **50**(49): 10598–606.

186. Arya, M., Anvari, B., Romo, G.M., Cruz, M.A., Dong, J.F., McIntire, L.V., Moake, J.L., et al., Ultralarge multimers of von Willebrand factor form spontaneous high-strength bonds with the platelet glycoprotein Ib-IX complex: studies using optical tweezers. *Blood*, 2002. **99**(11): 3971–7.

187. Goldman, A.J., Cox, R.G., & Brenner, H., Slow viscous motion of a sphere parallel to a plane wall—II Couette flow. *Chemical Engineering Science*, 1967. **22**(4): 653–660.

188. Yakovenko, O., Sharma, S., Forero, M., Tchesnokova, V., Aprikian, P., Kidd, B., Mach, A., et al., FimH forms catch bonds that are enhanced by mechanical force due to allosteric regulation. *J Biol Chem*, 2008. **283**(17): 11596–605.

189. Lopez, J.A., Ludwig, E.H., & McCarthy, B.J., Polymorphism of human glycoprotein Ib alpha results from a variable number of tandem repeats of a 13-amino acid sequence in the mucin-like macroglycopeptide region. Structure/function implications. *J Biol Chem*, 1992. **267**(14): 10055–61.

190. Afshar-Kharghan, V., Matijevic-Aleksic, N., Ahn, C., Boerwinkle, E., Wu, K.K., & Lopez, J.A., The variable number of tandem repeat polymorphism of platelet glycoprotein Ibalpha and risk of coronary heart disease. *Blood*, 2004. **103**(3): 963–5.

191. Ozaki, Y., Suzuki-Inoue, K., & Inoue, O., Platelet receptors activated via mulitmerization: glycoprotein VI, GPIb-IX-V, and CLEC-2. *J Thromb Haemost*, 2013. **11 Suppl 1**: 330–9.

192. Maurer, E., Tang, C., Schaff, M., Bourdon, C., Receveur, N., Ravanat, C., Eckly, A., et al., Targeting platelet GPIbβ reduces platelet adhesion, GPIb signaling and thrombin generation and prevents arterial thrombosis. *Arteriosclerosis, thrombosis, and vascular biology*, 2013. **33**(6): 1221–9.

193. Ravanat, C., Strassel, C., Hechler, B., Schuhler, S., Chicanne, G., Payrastre, B., Gachet, C., et al., A central role of GPIb-IX in the procoagulant function of platelets that is independent of the 45-kDa GPIbα N-terminal extracellular domain. *Blood*, 2010. **116**(7): 1157–64.

194. Dong, J.F., Gao, S., & Lopez, J.A., Synthesis, assembly, and intracellular transport of the platelet glycoprotein Ib-IX-V complex. *J Biol Chem*, 1998. **273**(47): 31449–54.

195. Riddell, A.F., Gomez, K., Millar, C.M., Mellars, G., Gill, S., Brown, S.A., Sutherland, M., et al., Characterization of W1745C and S1783A: 2 novel mutations causing defective collagen binding in the A3 domain of von Willebrand factor. *Blood*, 2009. **114**(16): 3489–96.

196. Bertz, M. & Rief, M., Mechanical unfoldons as building blocks of maltose-binding protein. *J Mol Biol*, 2008. **378**(2): 447–58.

197. Bertz, M. & Rief, M., Ligand binding mechanics of maltose binding protein. *J Mol Biol*, 2009. **393**(5): 1097–105.

198. Ganesh, C., Shah, A.N., Swaminathan, C.P., Surolia, A., & Varadarajan, R., Thermodynamic characterization of the reversible, two-state unfolding of maltose binding protein, a large two-domain protein. *Biochemistry*, 1997. **36**(16): 5020–8.

199. Aggarwal, V., Kulothungan, S.R., Balamurali, M.M., Saranya, S.R., Varadarajan, R., & Ainavarapu, S.R., Ligand-modulated parallel mechanical unfolding pathways of maltose-binding proteins. *J Biol Chem*, 2011. **286**(32): 28056–65.

200. Bechtluft, P., van Leeuwen, R.G., Tyreman, M., Tomkiewicz, D., Nouwen, N., Tepper, H.L., Driessen, A.J., et al., Direct observation of chaperone-induced changes in a protein folding pathway. *Science*, 2007. **318**(5855): 1458–61.

201. Collier, D.N., Bankaitis, V.A., Weiss, J.B., & Bassford, P.J., The Antifolding Activity of Secb Promotes the Export of the Escherichia-Coli Maltose-Binding Protein. *Cell*, 1988. **53**(2): 273–283.

202. Bacci, M., Chinappi, M., Casciola, C.M., & Cecconi, F., Role of denaturation in maltose binding protein translocation dynamics. *J Phys Chem B*, 2012. **116**(14): 4255–62.

203. Guardiani, C., Marino, D.D., Tramontano, A., Chinappi, M., & Cecconi, F., Exploring the Unfolding Pathway of Maltose Binding Proteins: An Integrated Computational Approach. *J Chem Theory Comput*, 2014. **10**(9): 3589–97.

204. Millet, O., Hudson, R.P., & Kay, L.E., The energetic cost of domain reorientation in maltose-binding protein as studied by NMR and fluorescence spectroscopy. *Proc Natl Acad Sci U S A*, 2003. **100**(22): 12700–5.

205. Xu, A.J. & Springer, T.A., Mechanisms by which von Willebrand disease mutations destabilize the A2 domain. *J Biol Chem*, 2013. **288**(9): 6317–24.

206. Zhang, W., Deng, W., Wang, Y., Zhou, L., Yang, W., Liang, X., Cho, S., et al. Identification of the mechanosensory domain in the platelet mechanosensor GPIb-IX complex. in *Journal of Thrombosis and Haemostasis*. 2014. Wiley-Blackwell.

207. Aioanei, D., Brucale, M., Tessari, I., Bubacco, L., & Samori, B., Worm-like Ising model for protein mechanical unfolding under the effect of osmolytes. *Biophys J*, 2012. **102**(2): 342–50.

208. Zhang, K. & Chen, J., The regulation of integrin function by divalent cations. *Cell Adh Migr*, 2012. **6**(1): 20–9.

209. Zhang, X., Zhang, W., Dragovich, M., Deng, W., & Li, R., Biophysical Characterization of Mechanosensors within the Plasma Protein von Willebrand Factor and its Receptor Platelet Glycoprotein Ib-IX. *Biophysical Journal*, 2016. **3**(110): 637a.

210. Meyer, D., Pietu, G., Fressinaud, E., & Girma, J.P., von Willebrand factor: structure and function. *Mayo Clin Proc*, 1991. **66**(5): 516–23.

211. Jorieux, S., Fressinaud, E., Goudemand, J., Gaucher, C., Meyer, D., & Mazurier, C., Conformational changes in the D' domain of von Willebrand factor induced by CYS 25 and CYS 95 mutations lead to factor VIII binding defect and multimeric impairment. *Blood*, 2000. **95**(10): 3139–45.

212. Weiss, H.J., Sussman, II, & Hoyer, L.W., Stabilization of factor VIII in plasma by the von Willebrand factor. Studies on posttransfusion and dissociated factor VIII and in patients with von Willebrand's disease. *J Clin Invest*, 1977. **60**(2): 390–404.

213. Tuddenham, E.G., Lane, R.S., Rotblat, F., Johnson, A.J., Snape, T.J., Middleton, S., & Kernoff, P.B., Response to infusions of polyelectrolyte fractionated human factor VIII concentrate in human haemophilia A and von Willebrand's disease. *Br J Haematol*, 1982. **52**(2): 259–67.

214. Foster, P., Fulcher, C., Houghten, R., & Zimmerman, T., An immunogenic region within residues Val1670-Glu1684 of the factor VIII light chain induces antibodies which inhibit binding of factor VIII to von Willebrand factor. *Journal of Biological Chemistry*, 1988. **263**(11): 5230–5234.

215. Leyte, A., Verbeet, M.P., Brodniewicz-Proba, T., Van Mourik, J.A., & Mertens, K., The interaction between human blood-coagulation factor VIII and von Willebrand factor. Characterization of a high-affinity binding site on factor VIII. *Biochemical Journal*, 1989. **257**(3): 679–683.

216. Shima, M., Yoshioka, A., Nakai, H., Tanaka, I., Sawamoto, Y., Kamisue, S., Terada, S., et al., Epitope localization of monoclonal antibodies against factor VIII light chain which inhibit complex formation by factor VIII with von Willebrand factor. *International journal of hematology*, 1991. **54**(6): 515–522.

217. Leyte, A., Vanschijndel, H.B., Niehrs, C., Huttner, W.B., Verbeet, M.P., Mertens, K., & Vanmourik, J.A., Sulfation of Tyr1680 of Human Blood-Coagulation Factor-Viii Is Essential for the Interaction of Factor-Viii with Von-Willebrand Factor. *Journal of Biological Chemistry*, 1991. **266**(2): 740–746.

218. Shima, M., Scandella, D., Yoshioka, A., Nakai, H., Tanaka, I., Kamisue, S., Terada, S., et al., A factor VIII neutralizing monoclonal antibody and a human inhibitor alloantibody recognizing epitopes in the C2 domain inhibit factor VIII binding to von Willebrand factor and to phosphatidylserine. *Thromb Haemost*, 1993. **69**(3): 240–6.

219. Saenko, E.L., Shima, M., Rajalakshmi, K.J., & Scandella, D., A role for the C2 domain of factor VIII in binding to von Willebrand factor. *J Biol Chem*, 1994. **269**(15): 11601–5.

220. Aricescu, A.R., Lu, W., & Jones, E.Y., A time- and cost-efficient system for high-level protein production in mammalian cells. *Acta Crystallogr D Biol Crystallogr*, 2006. **62**(Pt 10): 1243–50.

Biography

Wei Zhang was born in March 12, 1989 in Hefei, China. In 2007, he was admitted to the University of Science and Technology of China (USTC), and got his Bachelor of Science degree in Physics in 2011. He has a strong interest in mathematics, physics, as well as biology. He joined Lab of Laser-Biology at USTC, where his undergraduate thesis was finished. Under the supervision of Dr. Yinmei Li, Wei completed the project, *Optical Tweezers to Study the Non-specific Binding between the Polystyrene Spheres and the Cells*. During these four years, Wei was awarded the Outstanding Freshman Scholarship (11/2007) and the Outstanding Student Scholarship (11/2009). In the summer of 2009, he taught mathematics for senior high school students.

From August 2011, Wei was supervised by Dr. Xiaohui (Frank) Zhang at Lehigh University for his thesis of *Probing Internal Friction in the Mechanical Unfolding of Single Protein Molecule*, and obtained Master of Science degree in Mechanical Engineering and Mechanics department in September 2013. This project focused on the mechanical kinetics in single molecular field, with the use of atomic force microscopy (AFM). During the first two years at Lehigh University, he was awarded Dean's Doctoral Student Assistantship (09/2011) and Fellowship of Lehigh University (09/2012).

Since September 2013, Wei continued to pursue the degree of Doctor of Philosophy in Mechanical Engineering and Mechanics at Lehigh University under Dr. Xiaohui (Frank) Zhang. His research focused on clarifying mechanism of thrombosis by investigating the biological and mechanical properties of mechanosensitive molecules using single-molecule techniques, such as AFM. He is looking forward to getting more experience in single molecular field and mechanical field.